Doctoral Thesis

Shibaura Institute of Technology
Regional Environmental Systems
Tokyo, Japan

University of Caen Normandy
Physics, Engineering Sciences, Materials, Energy
Caen, France

Densification of MgB_2 superconducting cryomagnets: Synthesis and physical properties studies

2022 / September

Yiteng XING

Acknowledgments

First of all, I would like to express my sincere thanks to my supervisors, Prof. Jacques Noudem, Prof. Miryala Muralidhar and Prof. Pierre Bernstein, for their encouragement, advice and patience. Their guidance and inspiration are indispensable factors for me to complete my thesis work and deeply benefit me in my future research. Prof. Jacques Noudem and Prof. Pierre Bernstein have given me a lot of help and support both in my life and research work, from the master to the doctor. I have obtained much more detailed advices on the experiment process and writing skills from them. The opportunities they gave me to visit and experience different research fields at institute Néel (Grenoble) and LIMSA laboratory (Bologna), led to a great promotion of my work. I also would thank to Prof. Miryala Muralidhar for accepting me as his PhD student. Although I did not realize my plan to study in Japan due to the Covid, he still gave me great help and advice in my doctoral course.

I would appreciate Prof. Xaiver Chuad, Prof. Sophie Rivoirard, Mr. Paul Chometon and other people in CRETA and Néel, for their technology & equipment support and kindly help.

I would also like to thank Prof. Antonio Morandi, Prof. Pier Luigi Ribani, their PhD student Giacomo Russo and other people in the LIMSA laboratory, for their warm welcome and lots of help both in my research and enjoying life in Italy.

I also greatly appreciate all the people in CNRS/CRISMAT/CNRT, for their knowledge sharing, kindness and friendship, especially, Mr. Jerôme Lecourt, Mrs. Christelle Bilot, Mr. Fabien Veillon, Mrs. Sylvie Hebert and Mrs. Stéphanie Gascoin, who gave me a lot of help and technical support during these three years.

I must thanks the "Conseil Régional-Normandie, France" for my thesis schorlarship. I would also like to thank Project RIN 2020 and Project TUSFM (Alstom) for their research financial support.

Finally, I would thank all my friends in France and China, for their continuous encouragement and concern. I would give my appreciation to all members of my family, for their understanding and encouragement. Especially, my mother, who gives me encouragement every morning and much more support during my 8 years of life in France. My love for you can not be expressed with words only.

Thank you again to all of the above, I could not have completed the thesis without your help.

Table of Contents

Chapter 1 Generalities

1.1 History of superconductivity

Superconductivity is a phenomenon, which appears in some materials with zero electrical resistance below a critical temperature, T_c. In the late 19th century and the early 20th century, with the discovery of absolute zero [1] and the low-temperature environment produced by liquefaction of gases such as oxygen, nitrogen and hydrogen [2–4], people began to have great interests in the study of material properties at cryogenic temperatures. In 1911, after the success of helium condensation in 1908 [5], the superconductivity was firstly demonstrated by the Dutch physicist Kammerlingh Onnes [6], who observed that the electrical resistance of mercury disappeared below 4.2 K.

Although this type of materials required an extremely low temperature to remain superconducting, lots of scientists were attracted by their special property of no-resistance, which means no energy dissipation for the transport of electrical current. Therefore, the focus of research at that moment turned to finding or manufacturing materials with a higher and higher critical temperature. Between the 1950s and 1960s, the discovery of niobium-based superconducting alloys such as NbTi and Nb_3Sn [7,8] and the discovery of Josephson effect [9] caused an upsurge in the research and development of the low-temperature superconducting technology. However, before 1986, the highest T_c of conventional superconductors was still under 30 K. In 1986, a truly breakthrough discovery was made by Bednorz and Muller [10], who reported the superconductivity at 30 K of a LaBaCuO ceramic compound, the highest transition temperature known at that time. This remarkable discovery of superconductivity in the copper-oxides named cuprates, has boosted the research of other high critical temperature superconductors (HTS). In 1987, Wu et al. announced a transition temperature of 93 K in the Y-Ba-Cu-O system [11]. This compound was the first superconductor that could be cooled down by the inexpensive liquid nitrogen, and also became one of the most popular candidates for HTS applications. Higher and higher critical temperatures were discovered in the cuprate family in the following years: $Bi_2Sr_2Ca_2Cu_3O_8$ (T_c=110 K) $Tl_2Ba_2Ca_2Cu_3O_x$ (T_c = 124 K) and Hg-Ba-Ca-Cu-O system at high pressure (T_c=133 K at normal pressure and 164 K under 31 GPa) [12–15]. In 2001, Nagamatsu et al. [16] reported the superconductivity at 39 K of the intermetallic compound MgB_2. Compared to the cuprates, although its critical temperature was not spectacular, MgB_2 presents the conditions needed for the applications requiring the mass production of superconductors, as a consequence of its simple synthesis process and cheap cost. Otherwise, the discovery of the first iron-based superconductor La-Fe-P-O system with T_c = 5 K in 2006 [17] was also surprising, because magnetic elements such as iron atoms were considered as harmful for superconductivity. Then, in the ensuing years, numerous new iron-based superconductors have been discovered, such as LaFeAs[OF] (T_c = 26 K) and SmFeAs[OF] (T_c = 54 K) [18,19]. A $SrTiO_3$ doped single layer FeSe film was also reported with a surprisingly high T_c = 109 K [20]. Moreover, the study of the hydride superconductors under ultra-high pressure has shown important progress since 2000s. According to the Bardeen–Cooper–Schrieffer (BCS) theory [21], hydrogen was considered as one of the best candidate for HTS research due to its

high Debye temperature. However, at ambient pressure, most of light element compound are insulating. The first high-T_c-high-pressure hydride H_3S was discovered in 2015 [22], with a T_c of 203 K under 155 GPa, and 4 years later, a higher T_c of 260 K was observed in LaH_{10} under 190 GPa [23]. In 2020, the first room temperature superconductor C-H-S compound, was discovered by Snider, E. et al at 287 K under 267 GPa [24] and in the same year, Grockowiak, A. D. et al reported the superconductivity of La-H samples at and above room temperature until 550 K [25]! This indicates that nearly 110 years after the discovery of superconductivity, we have finally entered the era of room temperature superconductivity. Although this kind of superconductors cannot be used for applications, they are a milestone in the research on superconductivity. Fig.1-1 shows the maximum superconducting transition temperature over the years since the discovery of superconductivity.

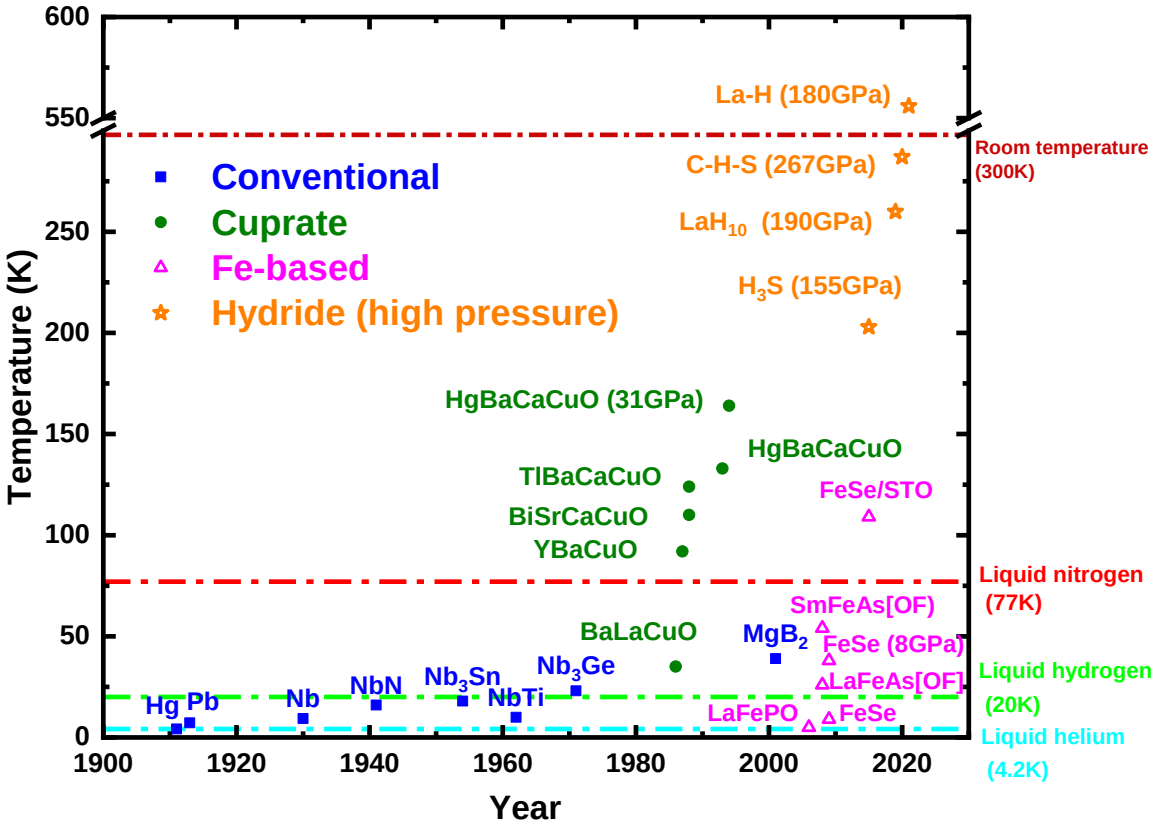

Fig.1-1 Evolution of the T_c since the discovery of the superconductivity phenomenon

1.2 Fundamentals of superconductivity

1.2.1 Characteristics of superconducting materials

In addition to the critical temperature T_c, superconductors have two other principal parameters: the critical current density J_c and the critical magnetic field H_c. The critical current density J_c is the maximum current density that a material can carry without any energy loss. If the density of the applied current is greater than J_c, superconductivity is destroyed, even below the transition temperature. The critical magnetic field H_c is the maximum magnetic field that can be applied to a superconducting material without transition to the resistive state. Fig.1-2 shows the superconducting region delimited by T_c, J_c and H_c in the T, J, B phase diagram.

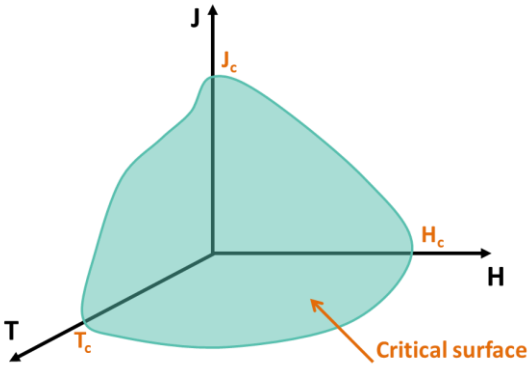

Fig.1-2 Relationship between T_c, J_c and H_c in superconducting materials

The Meissner effect [26] is another important property of superconductivity. In 1933, Meissner discovered that a superconductor could be suspended to a magnet. This discovery has shown that the superconducting state is not only a state with zero electrical resistivity, but also a state in which the magnetic field is expelled from the material (See Fig.1-3). When a magnetic field is applied to a material in the superconducting state, current loops appears on the surface. These induced currents produce a magnetic field that cancels exactly the applied field. This perfect diamagnetic property is mostly used in magnetic field shielding and maglev trains nowadays.

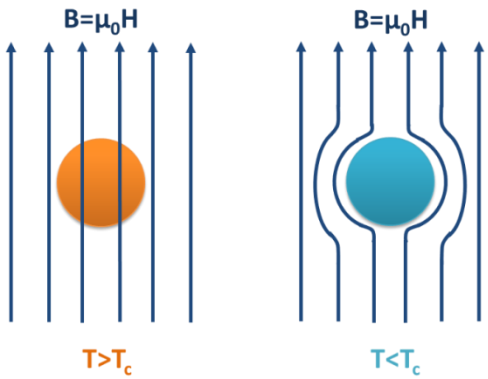

Fig.1-3 Diagram of the Meissner effect

1.2.2 The BCS theory

The first microscopic theory of superconductivity, the BCS theory was proposed by John Bardeen, Leon Neil Cooper and John Robert Shriver in 1957 [21]. It is based on the formation of electron pairs (known as Cooper pairs) under the effect of an attractive interaction between electrons and the vibrating crystal lattice.

As shown in Fig.1-4, when a negatively charged electron passes through a lattice of positively charged ions, the crystal lattice is slightly deformed by this electron and creates a prominent positively charged area which can attract another electron. These two electrons form then a Cooper pair. This process can also be regarded as a phonon exchange between two electrons.

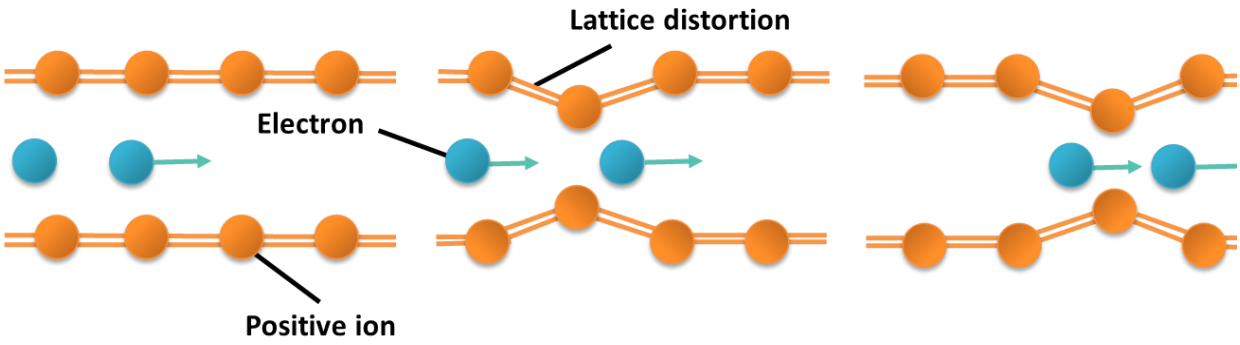

Fig.1-4 Formation of Cooper pairs

However, with the increase of the temperature, the ions in the material vibrate stronger and stronger, so that the phonon emission and absorption process can no longer occur, and the Cooper pairs disappear. This theory explains the condensation mechanism of electron pairs as electron-phonon coupling. It is valid for conventional superconductors but so far, there is no consensus for a model accounting for the formation of Cooper pairs in high T_c superconductors.

1.2.3 The Ginzburg–Landau theory

In 1950, the physicists Vitaly Ginzburg and Lev Landau presented a phenomenological theory of superconductivity based on their previously proposed model of phase transition [27]. This approach considers that the superconducting electron density in the material is not constant. It defines two characteristic lengths and makes possible to determine the nature of the superconducting material.

1.2.3.1 The Characteristic lengths

The superconducting state is characterized by two lengths: the penetration depth, λ and the coherence length, ξ. Length λ is the distance at which the magnetic field drops to zero from the surface of the material. Length ξ is the distance over which the density of superconducting electrons varies from its maximum value to zero. In reality, ξ and λ are

functions of the temperature and affect the values of J_c and H_c. The ratio of these two characteristic lengths [Eq.1.1], called the Ginzburg-Landau parameter

$$\kappa = \frac{\lambda}{\xi} \quad \text{[Eq.1.1]}$$

determines if the superconductor is type I or type II.

1.2.3.2 Type I and Type II superconductors

If $\kappa < \frac{1}{\sqrt{2}}$, the superconductor is type I. Materials in this family have only one critical magnetic field, H_c. Fig.1-5 (A) shows their phase diagram with a curve separating the normal state from the Meissner state. When the applied magnetic field, current or temperature exceed the critical value, a type I superconductor suddenly undergoes a phase transition to the normal state. Most of metal superconductors are type I, except niobium, technetium and vanadium.

The Ginzburg Landau parameter of the type II superconductors is greater than $\frac{1}{\sqrt{2}}$. Unlike type I superconductors, they show three different phases (See Fig.1-5 (B)). They don't undergo a direct transition from the Meissner to the normal state, because of the existence of the mixed state.

If a field lower than the first critical field H_{c1} is applied, the material is in the Meissner state. If the external field is increased without exceeding the second critical field H_{c2}, the material enters a phase called the mixed state. In the mixed state, the magnetic field cannot be completely expelled, but partially penetrates the superconductor under the form of cylindrical flux tubes in the normal state, called vortex or fluxoid, which are isolated from the rest of the material by superconducting currents loops. The radius of the vortex corresponds to the coherence length ξ. Away from the center, the magnetic field gradually decreases within a distance to the core approximately equal to λ. Beyond this distance, the magnetic field can be regarded as equal to zero. Therefore, the superconducting current can flow in the regions located between the vortices, and the resistance of the material is still equal to zero. Fig.1-5 (C) shows a vortex schematically.

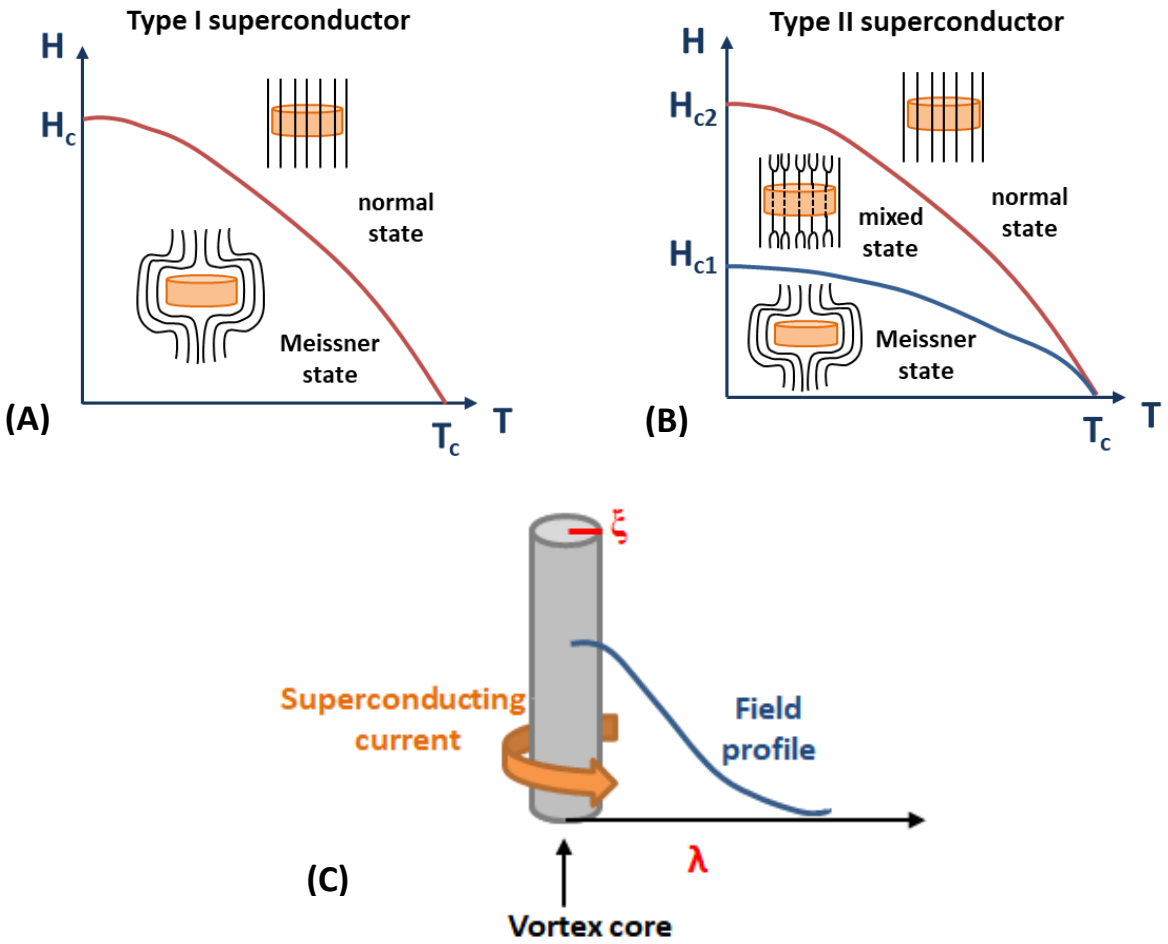

Fig.1-5 Phase diagram *H=f (T)* of (A) type I and (B) type II superconductor. (C) Schematic of a vortex produced by magnetic flux penetration in the mixed state of a type II superconductor

The magnetic flux of a vortex is quantized as shown in [Eq.1.2]

$$\varphi_0 = \frac{h}{2e} \quad \text{[Eq.1.2]}$$

where h is the Planck constant. The vortex axis is along the applied field, B_{appl}, and the surface density of the vortices, n, can be written as :

$$n = \frac{B_{appl}}{\varphi_0} \text{ [Eq.1.3]}$$

The thermodynamic critical field H_c, the lower critical field H_{c1} and the upper critical field, H_{c2}, of the type II superconductors are functions of ξ, λ and κ. We have [28]:

$$H_c = \frac{\varphi_0}{2\sqrt{2}\pi\xi\lambda\mu_0} \quad \text{[Eq.1.4]}$$

$$H_{c1} = \frac{ln(1.23\,\kappa)}{\sqrt{2}\kappa} H_c \quad \text{[Eq.1.5]}$$

$$H_{c2} = \sqrt{2}\kappa\, H_c = \frac{\varphi_0}{2\pi\xi^2\mu_0} \quad \text{[Eq.1.6]}$$

From Eq.1.5 and 1.6, we have $H_c \sim \sqrt{H_{c1}H_{c2}}$. The critical temperatures of the type II superconductors is higher than those of Type I. Currently, the highest temperature without applied pressure was observed on a cuprate compound containing mercury and was around 138 K.

1.2.4 Magnetic flux pining mechanism

The vortices in an ideal type II superconductor form a regular triangular lattice called Abrikosov lattice [29] in order to minimize the magnetic repulsion between fluxoids. Fig.1-6 shows the first observation of a triangular vortex lattice that was achieved in polycrystalline Pb-4at%In. However, if defects are present in the material, the vortices are preferentially located on these defects. This is generally the case for high T_c superconductors.

When a current flows in a superconductor penetrated by a magnetic field, the Lorentz force, $F_{Lorentz}$ [Eq.1.7]:

$$\overrightarrow{F_{Lorentz}} = \vec{J} \times \mu_0 \vec{H} \quad \text{[Eq.1.7]}$$

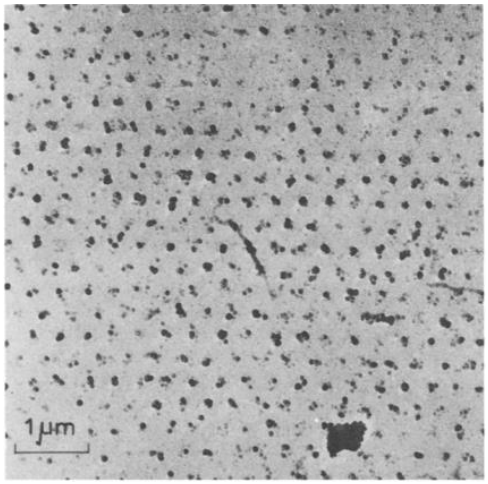

Fig.1-6 “Perfect” triangular lattice of flux lines on the surface of a lead-4at%indium rod at 1.1 K. [30]

acting on the vortices can result in a flux migration through the material. The heat and voltage generated by the vortex motion cause energy dissipation. However, the voids, disorders and impurities present in the material, can behave as pinning centers that prevent the flow of vortices and minimize the energy dissipation. The ability of superconductors to carry transport current in magnetic field depends on the density, distribution, and strength of the pinning sites. The pinning force is the largest Lorentz force that can be exerted on a motionless vortex while field $\mu_0 H$ is applied and a current with density $J_c(H)$ flows in the material. The pining force density, F_p, takes the form:

$$\overrightarrow{F_p} = \overrightarrow{J_c}(H) \times \mu_0 \vec{H} \quad \text{[Eq.1.8]}$$

When the density of current flowing in materials is above its critical value, vortices are set in motion leading to energy dissipation. Depinning and free motion of the vortices can also occur if the applied field is above a threshold field called irreversibility field, H_{irr}.

The flux pinning mechanisms depend on the operating magnetic field range. At fields not much larger than H_{c1}, the distribution of the vortices is mainly determined by weak interaction between flux lines. At intermediate fields, the vortices are subjected to the Lorentz force and pinned by pinning centers that hinder the fluxoids migration. When the number of vortices greatly exceeds that of the pinning centers, the flux motion is mainly determined by the combination of the pinning strength and the shear strength of the flux line lattice predicted by Kramer [31]. According to the Dew-Hughes model [32], which is usually utilized to represent the pinning mechanism in type II superconducting bulks, the type of pinning sites depends on their nature (superconducting or non-superconducting) and size. Two fundamental sources of pinning were determined: 1) the spatial fluctuation of the Ginzburg parameter associated with superconducting particles; 2) a scattering of the electron mean free path associated with non-superconducting (normal) particles existing in the superconducting matrix. The pinning centers can be classified as pinning points, surfaces and volumes by comparing the inter-flux-line spacing d (=1.07 $(\varphi_0/B)^{1/2}$) to the size of pins. Point pinning means all the dimensions of the pinning centers are less than d. Each point pin can interact with only one flux-line. In most of the materials, the grain-boundaries, stacking faults or dislocation arrays have two dimensions larger than d and plays the role of surface pinning centers. They can provide a large interaction force when the direction of the Lorentz force is parallel to their plane. Volume pins are usually due to large precipitates. All their dimensions are greater than d.

The pinning behavior can be analyzed using the normalized flux pinning force density, f_p with the following expression [Eq.1.9]:

$$f_p = \frac{F_p}{F_{p,max}} = Ah^p(1-h)^q \quad \text{[Eq.1.9]}$$

where A denotes a parameter related to the pinning strength, h is the reduced magnetic field (H/H_{c2}) and p and q are parameters that are related to the nature of the pinning sites (points, surfaces or volumes) and if they are superconducting or not superconducting.

However, in the literature h is usually calculated replacing H_{c2} by H_{irr} as a consequence of the limitation of the practical field applied to some high H_{c2} superconductors. Table 1-1 shows the flux pinning mechanism analyzed by the Dew-Hughes model. Nevertheless, several reports have mentioned that this model is not suitable in all cases. Other models will be discussed in Chapter 3.

Table 1-1 pinning behavior summarized by Dew-Hughes [32]

Geometry of pin	Nature of center	Peak of *h*	*p*	*q*
Volume	superconducting	0.5	1	1
	non-superconducting	-	0	2
Surface	superconducting	0.6	3/2	1
	non-superconducting	0.2	1/2	2
Point	superconducting	0.67	2	1
	non-superconducting	0.33	1	2

1.3 Superconducting materials MgB_2

1.3.2 Background and fundamental properties

Magnesium diboride, MgB_2 is an intermetallic compound, first reported by Morton E. Jones and Richard E. Marsh in 1954 [33]. In 2001, a research team at Okayama University in Japan announced that it was a type II superconductor with a critical temperature close to 40 K [16]. It is the "hottest" superconductor that can be described with the BCS theory, but it is also a "fairly close" member of the high critical temperature superconductor (HTS) family. MgB_2 shows various prominent aspects, especially: (i) a simple stoichiometry and a medium high critical temperature, T_c = 39 K, for a non-oxide superconductor, (ii) a low density and a strong hardness, (iii) a reasonably high upper critical field H_{c2} [34,35], (iv) a large current transport capability [36,37], generating the possibility to trap high magnetic fields [38–41] and to obtain large levitation forces with bulk samples [42,43]. In addition to bulks, this material can be fabricated in the form of thin-films [44,45], wires [46,47] and tapes [48,49], etc. Basically, the working temperature of MgB_2-based superconductors is around 20-27 K, which is obviously higher than that of the conventional metallic superconductors. Compared to cuprates HTS, although its transition temperature is relatively low for many applications, MgB_2 has fewer problems of anisotropy and no weak-links behavior at the grain boundaries in contrast to cuprates. The processing conditions of MgB_2-based materials are also simpler and quite cheaper than those of HTS materials. Otherwise, for applications, costs can be saved by developing technologies that use liquid hydrogen as cooling fluid.

MgB_2 shows a low anisotropy due to a simple hexagonal AlB_2 type crystallographic structure. It is composed of two honeycomb boron atoms sheets and a hexagonal magnesium layer (Fig.1-7). The magnesium layer is arranged in a triangle matrix between the two layers of boron. The mesh parameters of MgB_2 are $a = b$ = 3.0834 Å and c = 3.5213 Å [33].

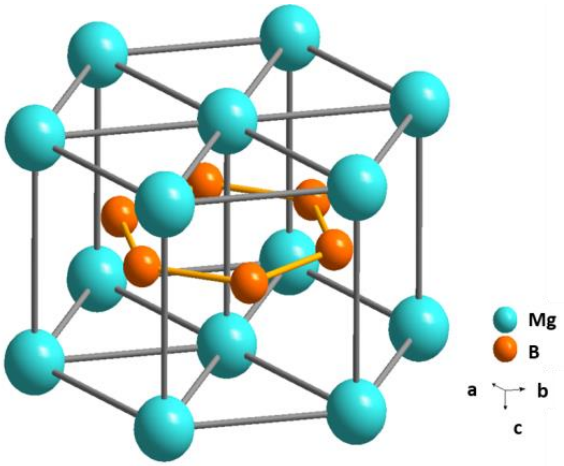

Fig.1-7 Crystal structure of MgB_2

At 0 K, the penetration depth, λ of MgB_2 is around 100-140 nm and the coherence length, ξ is approximately 5-12 nm. This large ξ value makes the materials unaffected by weak-link issues, in contrast to cuprate HTS. Furthermore, ξ along the *c*-axis is shorter than in the a-b plane [50], resulting in a higher value of the upper critical magnetic field H_{c2} when the magnetic field direction is perpendicular to the *c*-axis.[51].

Fig.1-8 shows the average superconducting properties of MgB_2 as compared to those of other common superconductors. Considering the practical applications of MgB_2, since J_c decays dramatically under a high external field, improving J_c in self-field (zero field) and under a strong applied field is one of the research "hotspots". If MgB_2 bulks present a low relative density as compared to the theoretical value, the resulting poor grain connectivity leads to a decrease of J_c at low magnetic field. Otherwise, the drop of J_c at high field is related to the lack of pinning centers in the materials, which also results in a reduction of H_{irr} as compared to H_{c2} (Fig.1-8 (B)). These superconducting properties can be improved by various factors, such as the synthesis method and sintering conditions, the stoichiometry, purity and particle size of the precursors, the type of dopants or additives etc. Unlike cuprate HTS, the J_c and H_{c2} values of MgB_2 can be strongly enhanced by increasing the grain boundaries number while decreasing the size of the grains [52,53], as a result of the lack of weak-link issues. Dense MgB_2 bulks can be prepared by applying an external sintering pressure [35,54,55]. Furthermore, based on the results of various studies, C, Ti and nano-SiC are effective dopants. They play the role of pinning sites, improving H_{irr} and H_{c2}, thus enhancing the J_c value under high magnetic field without causing a significant decrease of T_c [35,56–58]. Some metallic elements, such as Ag and Cu are also used with the objective to decrease the formation temperature of MgB_2 phase[57].

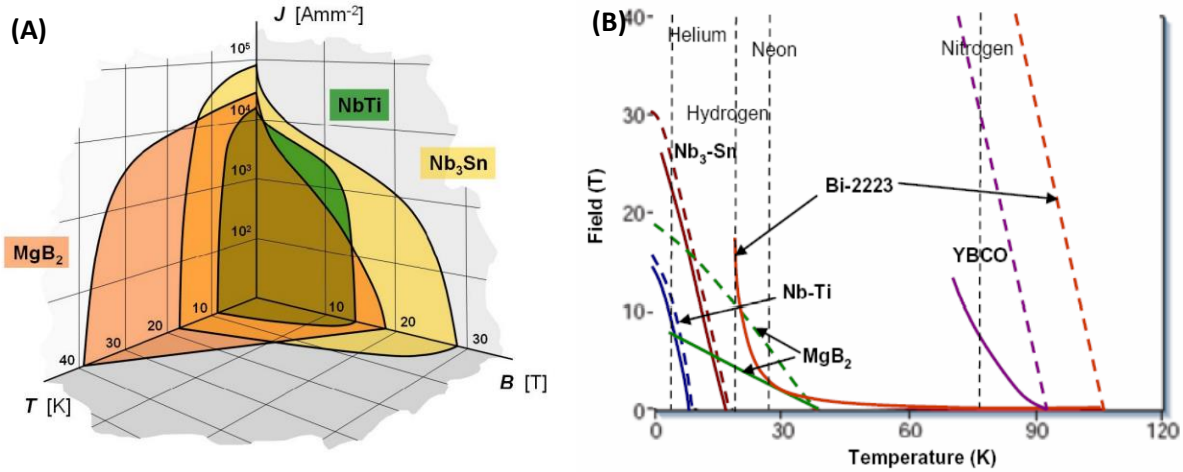

Fig.1-8 (A) Critical surfaces of MgB_2, NbTi and Nb_3Sn [59]. (B) Magnetic field vs. temperature phase diagram for several type II superconductors. The upper critical fields, H_{c2}, are indicated by dashed lines, the irreversibility fields, H_{irr}, by solid lines. [60]

1.3.2 Fabrication method of bulk MgB_2

The **conventional sintering (CS)** is the initial and most used method to prepare MgB_2 bulks. This simple technology consists in heating the compact powder prepared at room temperature without applying any external pressure during the process. Fig.1-9 (A) shows the phase diagram of the Mg-B system at ambient pressure. The melting point of magnesium is around 650°C and the decomposition temperature of MgB_2 is around 1174°C. MgB_4 appears in the MgB_2 phase if the Mg:B atomic ratio is between 1:4 and 1:2. The preferred process conditions of conventional sintering are temperatures in the 750°C – 850°C range and a 3 h sintering time [61].The main problem of this technology is the highly porous structure (around 50%) resulting from the evaporation of Mg at high temperature (See Fig.1-10 (A)). Another disadvantage is that the total time for sintering samples is long (more than 15 hours [62]).

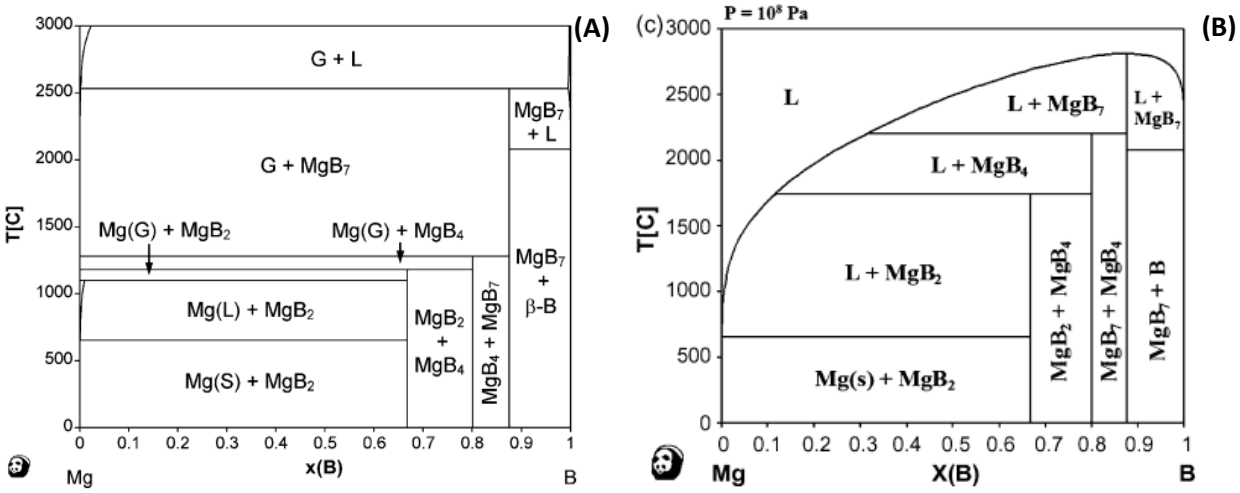

Fig.1-9 Mg–B binary phase diagrams at (A) atmospheric pressure and (B)100 MPa [63]

The Infiltration and growth process (IG) is also a frequently used technique to prepare MgB_2 bulks. Boron bulks with a relative density of about 50% of the theoretical value are infiltrated by excess liquid Mg, which makes contacts in the residual pores of the bulk microstructure. Bulks MgB_2 with a density around 90% [64,65] have been fabricated by IG method.

The phase diagram of the Mg-B system shown in Fig.1-9 (B), especially the increase of the decomposition temperature of the MgB_2 phase and the absence of Mg gas phase at high external pressure, demonstrates the possibility to promote densification by **hot pressing or hot isostatic pressing sintering (HP/HIP)**. The best result obtained by Prikhna et al. [66] shows a relative density of nearly 99% for bulks sintered at 2 GPa and 1050°C. However, the disadvantages of this technology are similar to the traditional preparation process. The time for heating and cooling the furnace is usually more than 10 hours.

Spark plasma sintering (SPS) [67–69] is one of the preferred techniques to prepare highly dense MgB_2 bulk superconductors. It is a rapid consolidation method that results in a better understanding and control of the sintering kinetics than the other techniques. The heat source is not external but is an electric current (AC, DC or pulsed) that flows across the die containing the powder to sinter. Simultaneously, a uni-axial pressure is applied. SPS sintering is controlled by 3 main parameters: sintering temperature, dwell time and applied pressure. These parameters determine the speed of densification and the granular growth. The main difference between SPS and other sintering methods is that SPS allows to prepare dense samples while controlling the grain growth and to save processing time (usually the total time is about 1 to 2 hours). However, this technique was not optimized, the maximum density of the MgB_2 bulks obtained by reactive sintering being around 90% (see table 1-2), although highly dense (99%) MgB_2 bulks could be prepared by sintering directly a commercial MgB_2 powder [54,70]. Hence one of the main objectives of my thesis was densifying MgB_2 bulks by SPS in order to improve their superconducting properties. Fig.1-10 (B) shows the compact microstructure of a MgB_2 sample with a relative density of 98% fabricated during my thesis.

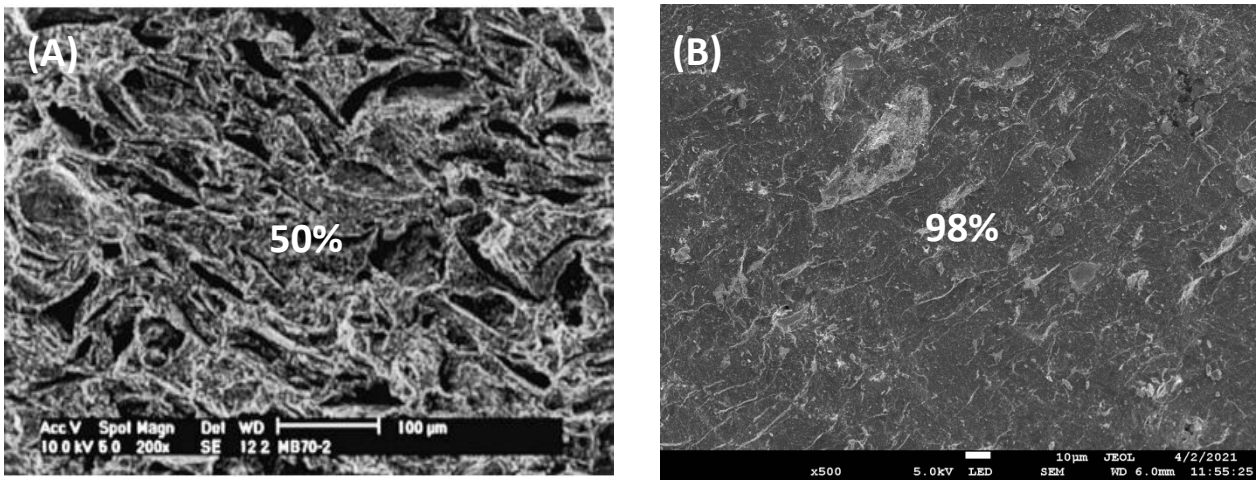

Fig.1-10 Microstructure of MgB_2 bulk fabricated by (A) CS [71] and by (B) SPS

Table 1-2 shows the density and grain size of MgB_2 bulks fabricated with different methods, correlated with their critical current density measured at 20 K. A significantly high density and small grain size samples are obtained by applying a high pressure during sintering with

the HP/HIP or the SPS technique. As a result, the J_c value increases in both low and high field. Nevertheless, as mentioned in several reports [72,73], the size of the specimen has a great effect on the measured J_c (this aspect will be discussed in Chapter 7) and unfortunately, some papers claiming extremely high J_c values didn't specify this.

Table 1-2 Characterization of MgB_2 bulks prepared by different technologies

Method	Process	Density	Grain size (nm)	$J_{c\text{-}0T}$ (A/cm^2)	$J_{c\text{-}2T}$ (A/cm^2)	$J_{c\text{-}4T}$ (A/cm^2)	Reference
CS	775-800°C 3h	50-60%	~ 100	2-3.10^5	2-7. 10^4	10^2-10^3	[61,74]
IG	750°C 2h	~ 90%	500	2.10^5	10^4	10^2	[65,75]
HP/HIP	1050°C 2GPa 1h	99%	17-37	5-9.10^5	1-2.10^5	1-2. 10^4	[66,76]
SPS	950-1000°C 50MPa 20 min	90%	~ 120	5.10^5	10^5	4.10^3	[54,70]

1.3.3 Applications of MgB_2 materials

Nowadays, the applications of superconductivity involve energy, transportation, industry, medicine, communication, environmental protection and many other aspects. They can be fundamentally divided into three categories according to the superconductor shape:

-Thin film, which are mainly used in electronics based on Josephson junction (superconducting computers and SQUID detectors, see Chapter 2).

-Tapes or cables, which could be used for current transport, in superconducting motors and generators, fault current limiters, generating the high magnetic fields required for scientific devices such as synchrotrons, particles colliders and fusion reactors, magnetic resonance imaging (MRI), and nuclear magnetic resonance (NMR).

- Bulks as electrical current leads and also could be applied for magnetic screening, energy storage and magnetic levitation.

However, only a few high-performance superconductors have been developed for applications and most of them are conventional low temperature superconductors (LTS) such as NbTi, Nb_3Sn and some cuprate high temperature superconductors (HTS) like YBaCuO. Nevertheless, with the discovery of superconductivity in MgB_2, the unique performances of this material have attracted the attention of industry, especially for its light weight, strong

hardness, simple and low cost manufacturing. Its suitable working temperature is around 20-30 K, which means that cooling cost could be reduced by using liquid hydrogen.

The J_c required for different applications and the J_c of different superconducting materials measured at 4.2 K are shown in the Fig.1-11. Considering the cooling costs of LTS and the production costs of HTS, MgB_2 could be a good candidate for many applications requiring a high J_c under a 0 - 7 T field, especially electrical transmission cable [77,78], MRI systems [79] and superconducting motors and generators [80]. Furthermore, in 2021, China rolled out a prototype of levitating train, levitation resulting from the interaction of a magnetic guideway with superconducting cuprates located in the train. This train has reached a maximum speed of 620 km/h [81,82]. However, the cost of the required superconducting material is high. The simple fabrication process of large size MgB_2 bulks with a levitation force similar to that of the best superconducting cuprates [42,83] shows the enormous potential of this material for magnetic suspension devices applications.

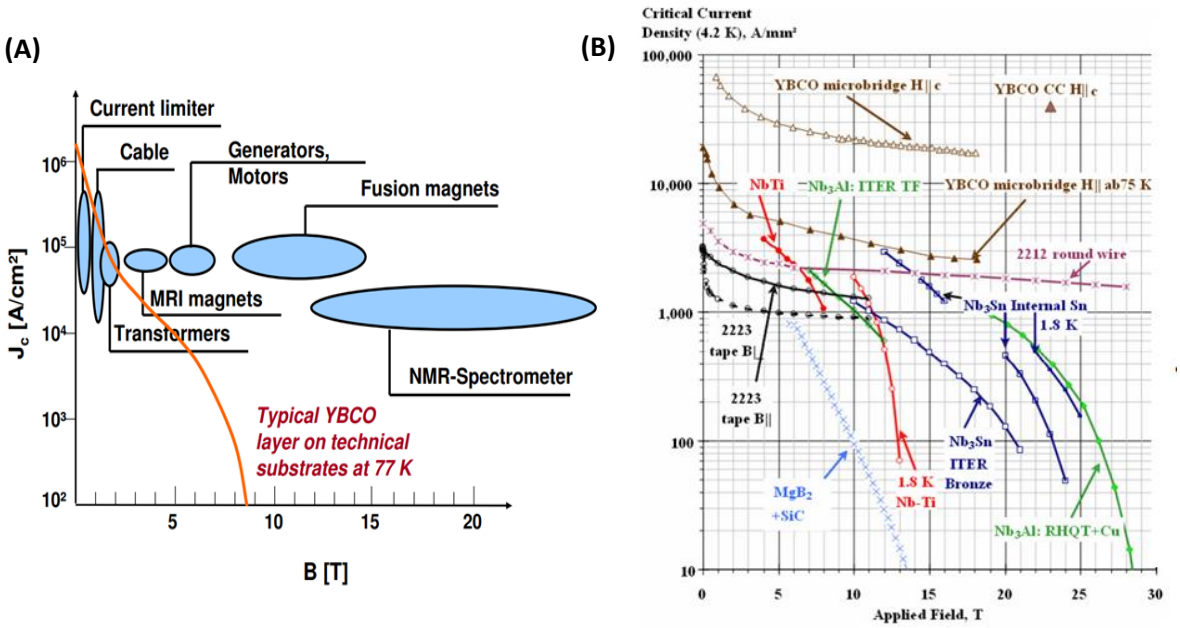

Fig.1-11: (A) Required properties for different power applications. (B) The critical current density of several type II superconductors dependence of applied field at 4.2 K [84]

1.4 Motivation and objectives

According to the above introduction and as a result of the superconducting properties of MgB_2 as well as of their potential applications, the objective of this thesis is:

• to investigate and understand the rapid "Spark Plasma Sintering-SPS" sintering mechanisms of magnesium borides (MgB_2) bulks. Precursor powders of different formulations have been synthesized, on the one hand from mechano-synthesis and reaction at the solid state, in collaboration with the chemists and material scientists of the Shibaura Institute of Technology (Tokyo) and on the other hand by optimizing the mixing-grinding process.

• to investigate the influence of the control of the microstructure on the superconducting properties.

• to fabricate and investigate the functional properties of large size MgB_2 discs at 20 K (working temperature of hydrogen liquid).

• to investigate the properties of bulks fabricated with various shapes for example, rings in addition to cylinders, discs reinforced with a metal ring, bulks with multiple holes in order to overcome magnetic flux jumps, one of the key points to obtain high trapped fields.

The characterization of the samples has been mainly done with the techniques available at the CRISMAT laboratory in Caen: measurements with a SQUID magnetometer of the magnetic moment created by the superconducting currents flowing in the samples, determination of their critical temperature by measuring their resistance as a function of the temperature and measurements of the levitation and lateral forces resulting from their interaction with NdFeB permanent magnets. Other magnetic forces measurements were carried out at the LIMSA laboratory in Bologna in Italy. Measurements of the trapped fields after magnetization of the superconductors either by a continuous field or by means of a pulsed field were carried out both at CRISMAT laboratory, institute Néel (Grenoble) and Shibaura Institute of Technology.

Chapter 2 Fabrication and Analysis way

2.1 Fabrication process of MgB_2 bulks

2.1.1 Fundamental principles of spark plasma sintering

Spark Plasma Sintering-SPS or Flash Sintering is an interesting emerging technique for forming, densifying and synthesizing different families of materials, such as polymers, metals and nanostructured ceramic materials as well as nanocomposites. This technology was initiated by Inoue [85] in Japan in 1962. It was not widely used due to the high cost and low sintering efficiency of the system at that time. It was developed during the 1980s and the 1990s and has received increasing attention over the past two decades due to its remarkable performances. SPS makes it possible to increase the sintering kinetics and thus to reduce the time required for grain growth by simultaneously applying a pulsed current of high intensity and an uniaxial pressure.

The principle of SPS (Fig.2-1(A)) is hot pressing the material with an uniaxial pressure. The heat source is not external but comes from an electric current (DC, pulsed, or AC) which goes through the conductive pressing chamber and also through the sample if it is conductive. The sintering temperature is controlled with a thermocouple or a pyrometer.

The powder in the mold is heated by Joule effect. When the current flows through the sample, it generates electric arcs or plasma discharges between the grains that result in an increase of the grain boundary diffusion and promote material transfer as well as grain growth (Fig.2-1(B)).

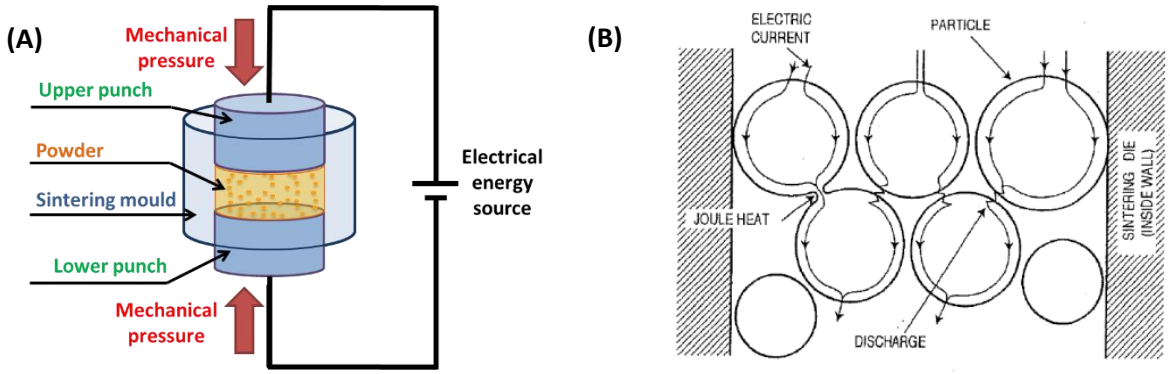

Fig.2-1 Schematic representation of (A) SPS device and (B) pulsed current flow through powder particles [67]

Almost all conventional SPS molds are made of graphite, which is a good and cheap conductor, allowing a high sintering temperature which can attain 2500°C but which limits the maximum pressure to 140 MPa. In a few cases, more expensive tungsten carbide (WC) dies can be used to increase the applied pressure up to 1 GPa with a maximum temperature of 800°C.

The main benefits of SPS technology are: i) significant sample densification, ii) grain growth control, iii) texturing in the case of layer structure materials [54,86].

The main difficulties of the SPS technology are to achieve the batch processes required for industrial applications and thermal gradients occurring during sintering. Different tool designs have been considered to solve the first problem [87]. The second one depends on the sintered powder and the components of the die. Fig.2-2 shows a simulation of current flow in different cases proposed by O. Guillon et al. [85]. The authors have mentioned that if the sample is conductive, a higher current density is obtained by using an insulating die, which forces the current to go through the powder (Fig2-2(A) and (B)). As a result, an electrical insulating coating layer such as a BN coated carbon foil inserted between the conductive powder and the inner surface of the graphite mold could enhance the current intensity and thermal uniformity. Insulating powders can be sintered by a rapid HP process (Fig.2-2(C)). However, the sintering efficiency can be improved by adding electrically conductive phases.

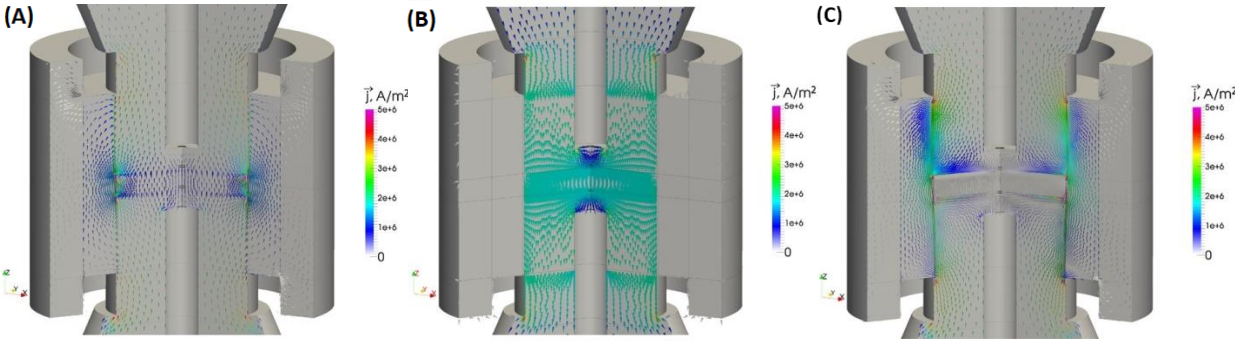

Fig.2-2 Schematic current flow in the case of: (A) conductive powder and die, (B) conductive powder and insulating die, (C) non-conductive powder and conductive die [87]

2.1.2 MgB_2 sample preparation

To investigate the characteristics and optimize the superconducting and functional properties of the fabricated bulks, different batches of samples were prepared with various precursor powders and SPS sintering conditions. The main precursor used during my thesis was the commercial powder purchased from PAVEZYUM advanced Chemicals, Turkey and abcr GmbH Germany (which we call ex-situ MgB_2 in the manuscript) and the in-situ mixing of magnesium (99.8%, 325 mesh, Alfa Aesar, USA) and nano-boron (99%, <400 nm, PAVEZYUM) in the 1:2 stoichiometric ratio. Other formulations were also tested, especially the mixture of Mg and MgB_4 powder provided by the Korea Atomic Energy Research Institute (Mg+MgB_4, from Prof. C-J. Kim group) and the boron powder coated with carbon provided by the Shibaura Institute Technology (Mg+2B/C, Prof. M. Muralidhar group). All the in-situ powders were grounded in an agate mortar for 10 minutes into the glove box under an argon atmosphere to suppress the oxidation reaction during the sintering process [62,88]. We have also studied the doping effect of Ti-6Al-4V (Ti64 alloy) and SiC additions on the superconducting properties of the bulks.

As mentioned above, the conductive powder is heated by Joule effect. Table 2-1 gives some basic parameters of the materials and molds used as a reference to the sintering process conditions. We emphasize that Mg and the MgB_2 powder have good thermal and electrical conductivity at room temperature, while boron is a semi-conductor that has a high resistivity

at room temperature, which decreases at high temperature. More details on the effects of the powders on the characteristics and properties of the sintered bulks will be presented in Chapter 3.

Table 2-1 Characterization of different compounds

Material	Melting point (°C)	Thermal conductivity (W/(m·K))	Resistivity (Ω·m)	Band gap [89] (eV)
Graphite	3600	4180	3-60 10^{-5}	0
WC	2870	110	2 10^{-7}	0
Mg	649	156	4.4 10^{-8}	0
B	2076	27	10^{6}	1.522
MgB_2	830	10-70	1-12 10^{-7} [90]	0
MgB_4	2076	-	-	0.365
SiC	2830	150-300	-	1.594-2.33

Two types of thermomechanical processing were used to prepare the samples: a one-step pattern for ex-situ sintering and a four-step pattern for in-situ reactive sintering. The introduction of several steps in in-situ sintering aimed at pre-synthesizing the MgB_2 phase and avoiding magnesium evaporation. The samples were sintered between 650°C and 1100°C with different durations, while an axial pressure between 50 and 300 MPa was applied under dynamic vacuum (10^{-3} bar). Fig.2-3 shows schemas of the processing patterns.

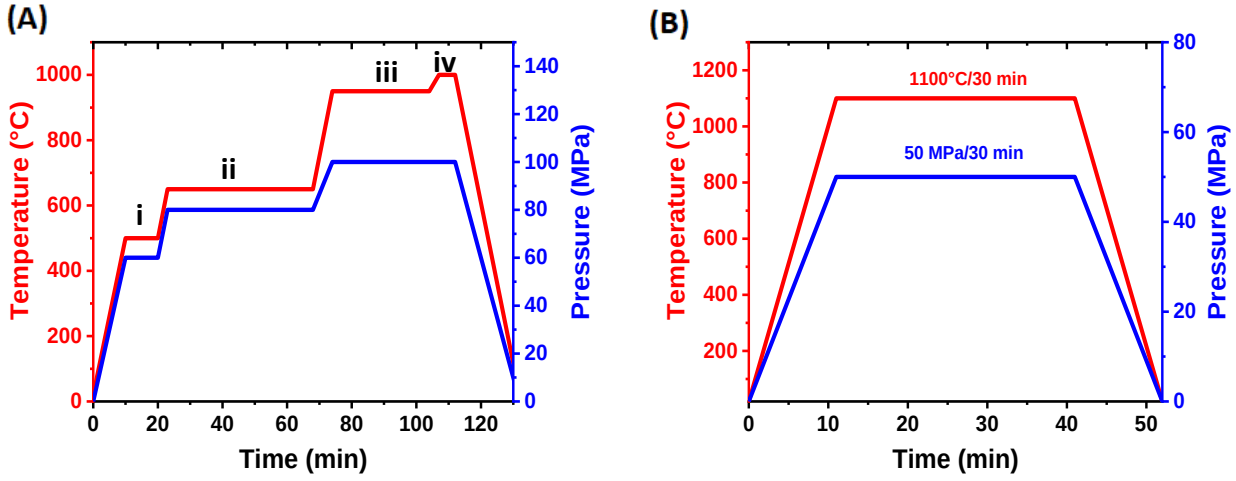

Fig.2-3 Heat treatment profiles of (A) in-situ sintering and (B) ex-situ sintering. The four steps of in-situ sintering are: i) 500 °C + 60 MPa / 10 minutes (compaction + pre-synthesis), ii) 650 °C + 80 MPa / 45 minutes (synthesis), iii) 950 °C + 100 MPa / 30 minutes (sintering) and iv) 1000 °C + 100 MPa / 5 minutes (densification)

2.2 Characterization techniques

This section describes briefly some common methods and measurements systems used to investigate the chemical and physical properties of MgB_2 samples.

2.2.1 Thermal analysis (DSC)

Differential scanning calorimetry (DSC) is a thermal analytical technique. When the sample undergoes a transformation, such as phase transitions or chemical reactions, it will absorb or release heat. DSC controls the temperature of the sample and of the references while recording the changes of heat flow as a function of temperature. In this work, the DSC device used is STA 449 F3 Jupiter (NETZSCH, Germany). The powder was loaded in an alumina crucible and measured from room temperature to 800°C in Ar atmosphere.

2.2.2 Density measurements

The small samples density ($D_{SC} \leq 20$mm) was measured by the Archimedes method with ethanol. The Archimedes principle refers to a buoyancy force received by an object immersed in a static fluid, which is equal to the weight of the fluid displaced by the object. The density of the sample can be calculated with the relation:

$$d_{sample} = \frac{w_{air}}{w_{air} - w_{fluid}} \cdot d_{fluid} \quad \text{[Eq.2.1]}$$

where w_{air} and w_{fluid} are the weight measured in air and in fluid, respectively while d_{fluid} is the density of the fluid.

The relative density of large size samples was simply determined with the following equation:

$$d_{sample} = \frac{m_{sample}}{V_{sample}} \quad \text{[Eq.2.2]}$$

2.2.3 Phase formation analysis (XRD)

The crystalline phases present in the samples were analyzed by X-ray diffraction (XRD) with a Philips θ-2θ diffractometer and the monochromatic Cu-Kα radiation. This characterization technique is based on the periodic scattering of X-rays by the regular arrangement of atoms in a crystallized solid. The distance between these regularly arranged atoms is of the same order of magnitude as the wavelength of the incident X-rays. The X-rays reflected by the different atoms interfere with each other, resulting in a reinforcement of the X-ray amplitude at typical angles. This diffraction phenomenon is closely related to the crystal structure and is described by the Bragg's law [91]:

$$2d_{hkl} \sin\theta = n\lambda \quad \text{[Eq.2.3]}$$

where d_{hkl} is the distance between parallel lattice planes with indices h, k and l, θ the X-ray incident angle, n the diffraction order and λ the wavelength of X-rays. The X-ray diffraction has been developed and applied to the refinement of crystal structures, microstructure

analysis (crystallite size, texture, microstrain), crystallinity, detection of unknown phases and quantitative analysis.

2.2.4 Microstructure characterizations (SEM)

The microstructure of the samples was studied by scanning electron microscopy (SEM). This is an observation technique the resolution of which is between that of transmission electron microscopy (TEM) and that of optical microscopes. The surface of the sample is scanned by a focused beam of electrons and the interaction of the electrons with the sample results in secondary electrons, backscattered electrons, Auger electrons and X-rays that give physical and chemical information. The secondary and Auger electrons are emitted by atoms located at a distance below 10 nm from the specimen surface, which is suitable for the analysis of the surface morphology and chemical composition. The backscattered electrons and the X-rays are emitted by atoms located at a distance between 100 nm and 5000 nm from the surface and are used for the qualitative and quantitative analysis of the chemical composition of the sample.

In this work, the microscope used were a Zeiss Supra 55 and a JEOL 7200.

2.3 Measurements of Superconducting properties

This section presents on the one hand, the systems used to determine the basic superconducting properties of the samples (T_c, J_c, H_c and H_{irr}) by measuring their magnetic moment and resistivity; on the other hand, the systems used to measure the functional properties of large size bulks, especially the levitation and stabilizing forces when interacting with a magnet and the field trapped after the application of a magnetic field are described.

2.3.1 Magnetization measurements (SQUID)

The T_c and J_c of samples were determined by measurements carried out with a very sensitive magnetic flux sensor called Superconducting Quantum Interference Device (Quantum Design MPMS SQUID, San Diego, USA) that is based on the Josephson effect [9] and magnetic flux quantization.

The Josephson effect refers to the current flowing across a Josephson junction. A Josephson junction consists of two superconducting electrodes separated by a thin barrier layer the thickness of which is in the range of the coherence length of the electrodes material. The barrier can be either insulating (S-I-S junction) or made with a normal metal (S-N-S junction), or be a narrow superconducting bridge in the normal state. When carrying out measurements with the SQUID, the sample is moved vertically. The SQUID includes a superconducting loop containing two Josephson junctions which detects the small variations of current induced by the motion of the magnetized sample and converts them into voltage variations which are proportional to the magnetic moment of the sample [92]. In general, two techniques are used for measuring the magnetization of superconductors. They are called Zero Field Cooling (ZFC) and Field Cooling (FC). In the ZFC case, the superconductor is firstly cooled down to a temperature below its critical temperature and then an external

magnetic field is applied. In the FC case, the magnetic field is applied while the superconductor is cooled down below its critical temperature.

Our measurements were basically carried out on specimens with dimensions approximately equal to 1.5 x 1.5 x 1.5 mm^3 cut from the bulk to characterize. The magnetic moment of the sample was measured from 20 K to 40 K with a 20 Oe applied field after ZFC to determine its critical temperature. Magnetization hysteresis loops (Fig.2-4) were measured at different temperatures below T_c. For these measurements, after temperature stabilization, the field was slowly increased from 0 T to 5 T, then decreased to -5 T and finally brought to 5 T. The critical current density was estimated using the extended Bean model [93] for rectangular samples with the equation:

$$J_c = \frac{20\Delta M}{a^2 c\left(b-\frac{a}{3}\right)} \quad \text{[Eq.2.4].}$$

In [Eq.2.4] a, b ($a \leq b$) and c are respectively the width, the length and the thickness of the specimens; ΔM is the difference in magnetic moment for the same absolute value of the applied field between the increasing and decreasing field steps (Fig.2-4). The direction of the external magnetic applied field for all measurements was conventionally parallel to the pressure applied during the SPS sintering process. Furthermore, the flux pinning forces of some samples were investigated from M ($\mu_0 H$) data.

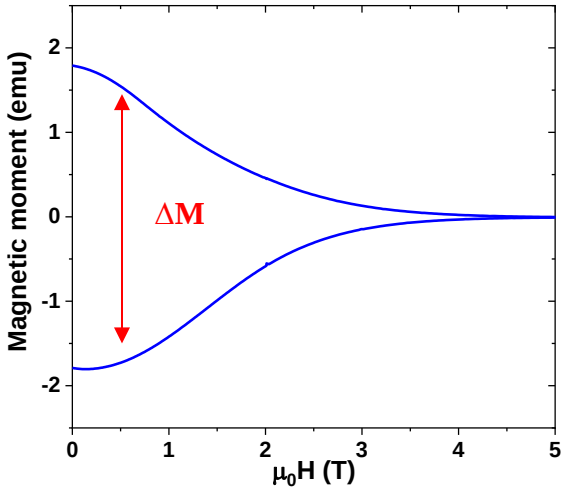

Fig.2-4 M-H loop obtained by SQUID used for determination J_c

2.3.2 Resistivity measurements (PPMS)

The critical temperature T_c, and the H_{irr} and H_{c2} fields can be determined by measuring the resistivity of samples. Rectangle bars were cut from sintered samples with dimensions about 1.5 x 1.5 x 10 mm^3. The electrical resistance was measured by the DC 4-probe method with a PPMS (Quantum Design, San Diego, USA) system. The contacts on the samples were made using silver paste (4929N). The current applied into the bar sample was 5 mA. The resistance was measured as a function of the temperature (10 K-300 K) while applying a magnetic field up to 14 T. The resistivity was then calculated with following equation:

$$\rho = \frac{R \cdot S}{L} \quad \text{[Eq.2.5]}$$

where R is the resistance value measured with the PPMS, S the cross-sectional area of the sample and L the distance between the 2 voltage measurements electrodes. Distance L is measured accurately with an optical microscope (Fig.2-5).

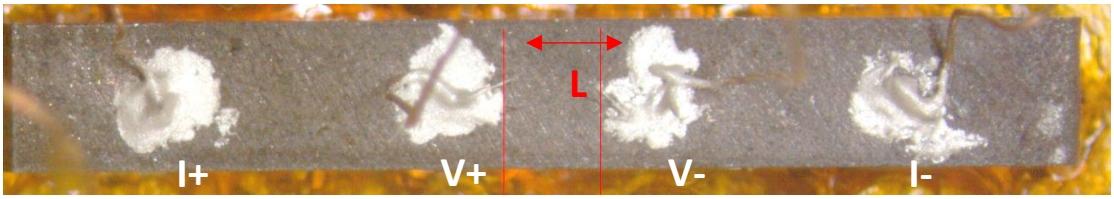

Fig.2-5 One sample in 4-probes configuration

The irreversibility field H_{irr} and upper critical field H_{c2} were determined from 10% and 90% of ρ_{40K} at normal state as reported elsewhere [88,94].

2.3.3 Levitation and lateral forces measurements

Superconducting Magnetic levitation (SML) is an important application of superconductors. The levitation force and its stability are closely related to the superconducting material, the source of the magnetic field, and geometrical dimensions. The measurements of the levitation and lateral forces were carried out at our laboratory and also at LIMSA laboratory in Bologna (Italy).

2.3.3.1 Measurements at *CRISMAT*

The levitation and lateral forces were measured after field cooling the superconductor using NdFeB permanent magnets. These measurements were made by fixing the superconducting bulk in the chamber of a cryostat cooled by a cryogenerator (Fig.2-6). The temperature in the cryostat could be tuned between 14 K and 300 K. The cryogenerator consists of a gaseous-helium cooling system with refrigerated water and a two-stage expansion system. A turbomolecular pump achieves vacuum down to 5.10^{-6} mbar in the cryostat. A 3D displacement system (Micro-Contrôle Spectra-Physics) carrying the magnet and the vertical and lateral force sensors allows to measure the levitation and the stabilizing forces in the vertical and the lateral direction, respectively. The maximum force which can be measured with this system is 250 N. Since the interaction force between the magnet and the superconductor can be extremely large, ($\approx$200 N for superconductors of 70 mm in diameter), it is necessary to fix them securely. In the cryostat chamber, the sample is blocked above a copper holder by 4 horizontal screws going through a ring screwed to the copper holder (Fig.2-6(B)). The thermal contact between the superconductor and the sample holder is provided by silicone vacuum grease that solidifies at low temperatures and reinforces the fixation. The magnet is held in place thanks to an iron piece screwed firmly to a bracket mounted on the displacement table. The temperature of the sample is measured with a platinum temperature probe (Pt100) placed on the surface of the superconductor and protected by a Teflon tape to avoid electrical contact with the sample holder.

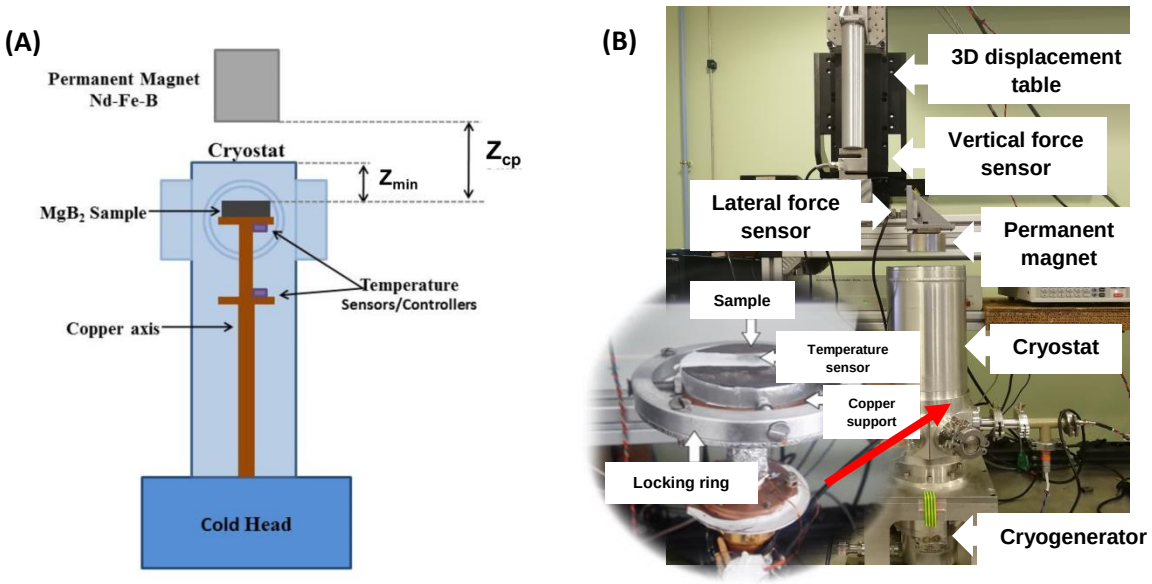

Fig.2-6 (A) Schema of the force measurements set-up. (B) picture of the cryocooler system and of the inside of cryostat

Levitation force measurements: the magnet was located above the cryostat at distance Z_{cp} (cooling height) from the superconductor surface with the 3-axes positioning system, in order that its axis was along the superconductor axis ($Y = 0$). Then, the MgB_2 disc was cooled down to the measurement temperature T. When the sample temperature was stabilized, the magnet was moved down vertically in the direction of the cryostat. Once in contact with the top of the cryostat at $Z = Z_{min}$, its direction of motion was reversed and it was moved up, as shown in Fig.2-7(A). The interaction force between the magnet and the superconductor was recorded as a function of Z during the whole process (Fig.2-7(B)).

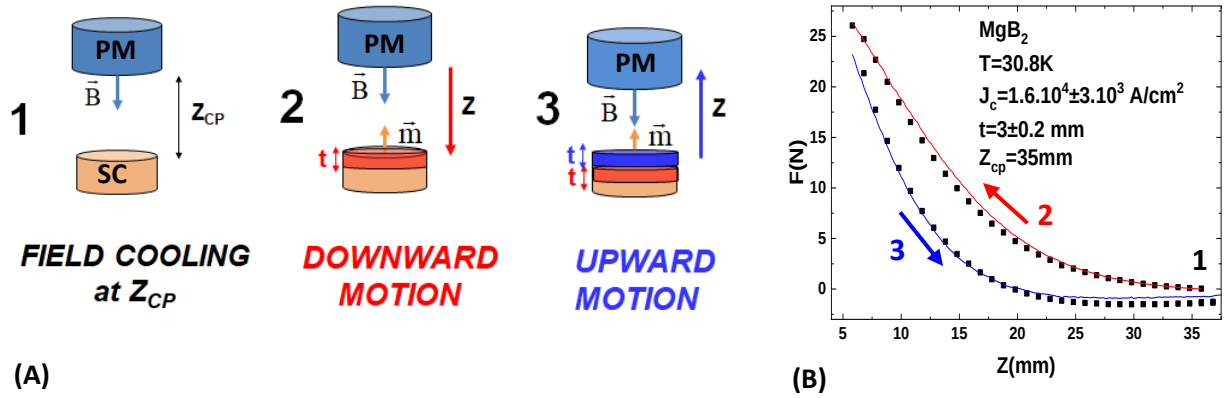

Fig.2-7: (A) Measurement procedure of the levitation force with the assumed locations of the currents interacting with the field of the magnet. (B) Levitation force hysteresis loop carried out between a 29.6 mm diameter MgB_2 bulk and a 45 mm diameter magnet at 30 K after FC at Z_{cp} = 35 mm. The continuous lines show the values calculated with Eq.2.6-14. and the J_c and t values indicated in the figures [43].

These results are interpreted as follows: during field cooling, vortices enter the superconductor at T_c and channel the magnetic field lines. No current flowing in the sample at that time, its magnetic moment and the interaction force with the magnet are zero. The

average value of the field inside the material is equal to the field applied at T_c. When the magnet approaches the superconductor, this last condition is no longer respected and shielding currents appears to restore it. The magnetic moment of these currents interacts with the external field generating a force that can be calculated with a mean field model [43,95]. The model assumes that the superconducting currents don't flow in the whole volume of superconductor but in a restricted region with thickness *t*. During the downward motion of the magnet, the magnetic moment, m_{down} depends on the difference between the average value on thickness *t* of the magnetic field along the superconductor axis at altitude *Z* [$\bar{B}_{PM}(Z)$] and the average value on thickness *t* of the magnetic field along the axis at altitude Z_{cp} [$\bar{B}_{PM}(Z_{cp})$]. According to the expression proposed by Brandt [96] for the magnetic moment of a cylindrical superconductor with diameter D_{SC} we have:

$$m_{down} = -\frac{2}{3} J_c \, t \, \frac{D_{SC}}{8}^3 \left[\cos^{-1}\left(\frac{1}{\cosh\left(\frac{2\Delta B}{\mu_0 J_c t}\right)} \right) + \frac{\sinh\left|\frac{2\Delta B}{\mu_0 J_c t}\right|}{\cosh^2\left(\frac{2\Delta B}{\mu_0 J_c t}\right)} \right] \quad \text{[Eq.2.6]}$$

with:

$$\Delta B = \bar{B}_{PM}(Z) - \bar{B}_{PM}(Z_{cp}) \quad \text{[Eq.2.7]}$$

From the expression of the force $\vec{F}$ applied to a magnetic moment located in an inhomogeneous magnetic field $\vec{B}$:

$$\vec{F} = \left[\vec{m} \cdot \vec{\nabla}\right]\vec{B} \quad \text{[Eq.2.8]}$$

the levitation force is written as:

$$F_Z(Z) = m_{down} \cdot \frac{\partial \bar{B}_{PM}(Z)}{\partial Z} \quad \text{[Eq.2.9]}$$

The value of the magnetic moment reaches its maximum at Z_{min} when the magnet is as close to the sample as possible. After the motion of the magnet is reversed, the induced currents present in the superconductor at Z_{min} do not disappear and they generate magnetic moment m_{max}. At $Z>Z_{min}$, the average value of the field generated in the material by the vortices and these currents is no longer equal to the field applied at T_c. To restore this field, a new current layer circulating in the direction opposite of the first one appears generating moment m_r. Therefore, the magnetic moment during the upward motion of the magnet includes two components: m_{max}, which depends on the difference between the average fields at Z_{min} and Z_{cp}, and m_r, which depends on the difference between the average fields at *Z* and Z_{min}. [Eq.2.10-13].

$$m_{max} = -\frac{2}{3} J_c t \, \frac{D_{SC}}{8}^3 \left[\cos^{-1}\left(\frac{1}{\cosh\left(\frac{2\Delta B_{max}}{\mu_0 J_c t}\right)} \right) + \frac{\sinh\left|\frac{2\Delta B_{max}}{\mu_0 J_c t}\right|}{\cosh^2\left(\frac{2\Delta B_{max}}{\mu_0 J_c t}\right)} \right] \quad \text{[Eq.2.10]}$$

and

$$m_r = -\frac{2}{3} J_c t \frac{D_{SC}}{8}^3 \left[\cos^{-1}\left(\frac{1}{\cosh\left(\frac{2\Delta B_r}{\mu_0 J_c t}\right)} \right) + \frac{\sinh\left|\frac{2\Delta B_r}{\mu_0 J_c t}\right|}{\cosh^2\left(\frac{2\Delta B_r}{\mu_0 J_c t}\right)} \right] \quad \text{[Eq.2.11]}$$

where:

$$\Delta B_{max} = \bar{B}_{PM}(Z_{min}) - \bar{B}_{PM}(Z_{cp}) \quad \text{[Eq.2.12]}$$

and

$$\Delta B_r = \bar{B}_{PM}(Z) - \bar{B}_{PM}(Z_{min}) \quad \text{[Eq.2.13]}$$

It has turned out that the experimental measurements are well reproduced with this model if it is supposed that the current layer generating m_{max} is located just below that generating m_r.

The resulting force is written as:

$$F_Z(Z) = m_{max} \cdot \frac{\partial \overline{B}_{PM}(Z+t)}{\partial Z} + m_r \cdot \frac{\partial \overline{B}_{PM}(Z)}{\partial Z} \quad \text{[Eq.2.14]}$$

The reproduction of the force cycle due to the interaction between a 29.6 mm diameter MgB_2 bulk and a 45 mm diameter magnet at 30 K is shown in Fig.2-7(B) with continuous lines. Although the temperature is not present in [Eq.2.6-14], moments m_{down}, m_{max} and m_r depend on T since t, as well as J_c, are functions of temperature.

Lateral force measurements: after field cooling at $Z = Z_{cp}$ and $Y = 0$, the magnet was moved parallel to the disk surface up to Y_{max} where the direction of motion was reversed and distance Y decreased down to Y_{min} before increasing to zero. The lateral force was recorded as a function of Y along the whole process (see Fig.2-8(A)). Then, the magnet-superconductor distance was slowly set to other altitudes $Z<Z_{cp}$ and the same measurements were carried out down to the region where the slope of F_Y, the lateral force, is positive (solid square in Fig.2-8(B)) which means that levitation is unstable.

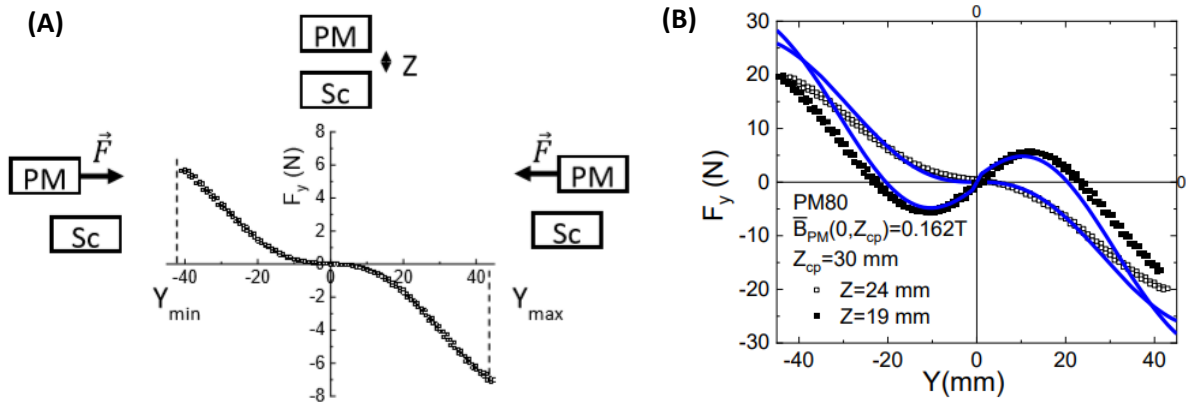

Fig.2-8: (A) Measurement of the lateral force: the figure shows the positions of both the permanent magnet (PM) and the superconductor (Sc) as well as the lateral force F_Y at different steps of the measurement procedure. The graph is an example of the obtained curves. (B) Lateral forces F_Y measured at 20K with a 70 mm diameter MgB_2 disc and a 80 mm diameter magnet at Z=24 mm and Z=19 mm after cooling down the MgB_2 disc at Z_{cp}=30 mm. The square symbols show the measurements and the continuous lines the forces calculated with the model. [97]

For modeling the lateral force, we take a point of view similar to that of the model described above for the levitation force. Since the system is not axisymmetric for *Y≠0*, we assume that:

$$\Delta B = \bar{B}_{PM}(0, Z_{cp}) - B_{\phi}(Y, Z) \quad \text{[Eq.2.15]}$$

where:

$$B_{\phi}(Y, Z) = \frac{\phi(Y,Z)}{\pi\frac{D_{SC}^2}{4}} \quad \text{[Eq.2.16]}$$

In [Eq.2.16], $\phi(Y, Z)$ is the flux of the mean value on thickness *t* of the field threading the disc when the magnet is at location (Y, Z). Since for $Y = 0$ the field takes its maximum value along the disc axis, we have $\bar{B}_{PM}(0, Z) > B_{\emptyset}(Y, Z)$ for any *Z*. Otherwise, using the Brandt relation [Eq.2.7] for calculating the magnetic moment $m(\Delta B, J_c, t)$, the lateral force F_Y takes the form:

$$F_Y = m(\Delta B, J_c, t) \cdot \frac{\partial B_{\emptyset}(Y,Z)}{\partial Y} \quad \text{[Eq.2.17]}$$

2.3.3.2 Measurements at LIMSA

Other forces measurements were carried out at the Laboratory of Magnet Engineering and Applied Superconductivity (LIMSA) of the University of Bologna (Unibo) in the case of framework collaboration between CRISMAT and LIMSA laboratories. One of the objectives of this study was to compare the levitation and guidance forces measurements carried out at CRISMAT to those carried out with the LIMSA system. Otherwise, the LIMSA system can measure forces larger than the CRISMAT system, as well as samples too large to be measured at CRISMAT.

The principle of the LIMSA measurements system is similar to that of our equipment. This facility, originally developed by EDISON SpA, consists of a vacuum chamber surrounding a copper plate connected to the second stage of a Sumitomo RDK 415D cryocooler. The superconductor is in thermal contact with the copper plate and can reach a temperature of 16 K. Temperature is measured by means of two diodes (LakeShore, type D-670- SD-4L) mounted onto the bottom side of the disk. Cooling the superconductor at 20 K can be done in about 3 hours. Superconductor bulks with maximum size up to 200 mm can be cooled and measured by means of the facility. The temperature of the superconductor can be controlled in the range 16 K – 90 K. The facility is equipped with a mechanical apparatus able to drive a permanent magnet along the vertical (*Z*) and the horizontal (*Y*) axes of measurement and with a pair of strain gauges (Burster Italia model 8432) that measure the forces along *Z* and *Y*. Both force sensors are able to measure forces up to **1000 N**. The Maximum excursion of the moving arm along the vertical and the horizontal direction is 56 mm. Fig.2-9 shows pictures of the facility.

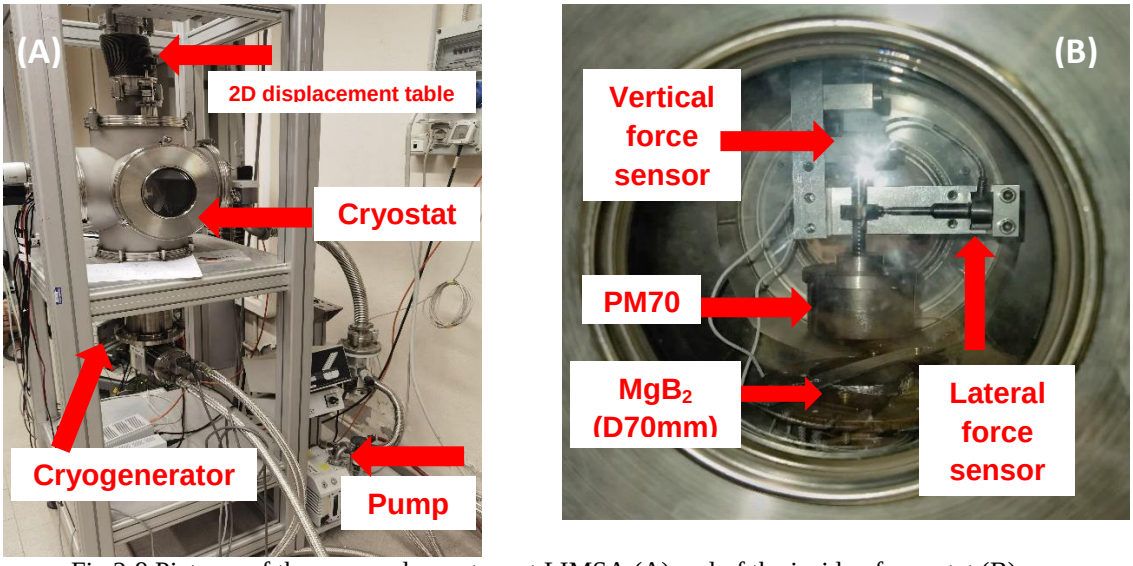

Fig.2-9 Pictures of the cryocooler system at LIMSA (A) and of the inside of cryostat (B)

Force measurements were carried out with different MgB_2 samples and magnets. The results were compared to measurements carried out in our laboratory and were used to improve the models for levitation and guidance described above.

2.3.4 Trapped field measurements

Bulk superconductors can be used as cryo-magnets. For this purpose, the superconductors are magnetized with a large magnetic field that is subsequently suppressed. The techniques used to magnetize superconductors are: zero field cooling, field cooling and pulsed-field magnetization [98,99]. In this work, the samples were magnetized by field cooling and all the measurements were carried out at CRISMAT laboratory (Caen, France) and at Néel institute (Grenoble, France, collaboration with Dr. X. Chaud).

2.3.4.1 Magnetization with a NdFeB Permanent Magnet

An axial Hall probe was attached to the 3D displacement table. The magnet was placed above the superconductor at Z_{min}, and the sample was cooled down to the working temperature. When the temperature was stabilized, the magnet was slowly moved upwards at a speed of 1 mm/s. The low magnet speed reduces vortex depinning and as a result, energy dissipation in the superconductor. When the magnet was far enough away from the superconductor, it was replaced by the Hall probe. A mapping of the field generated by the superconductor at given distances from its surface was then plotted.

2.3.4.2 Magnetization by field applied from the PPMS system

Trapped field measurements of small size bulks ($D_{SC} \leq 20$ mm) were carried with the PPMS system. According to the process described by Aldica G et al. [100], we have designed several sample holders adapted to the measuring conditions. Fig.2-10 shows one of the

holders. The sample was fixed by resin varnish and some copper wires. The field was measured with a Hall sensor (HE144T, Asensor) placed above the center surface of superconductor. A buffer layer made with PLA plastic was used to protect the sensor. Compared to the first method, using the PPMS system allows to apply a higher magnetic field but the maximum diameter of the sample is smaller.

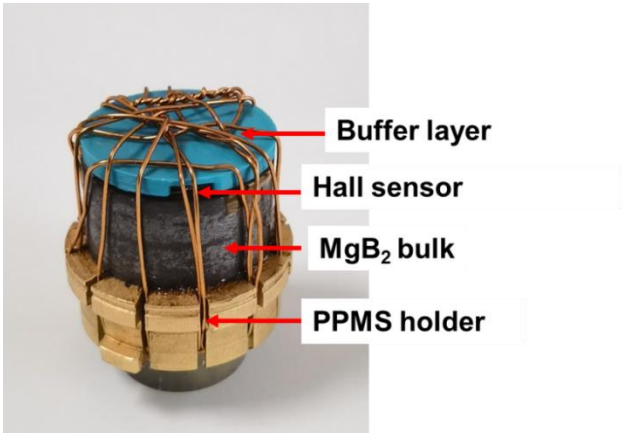

Fig.2-10 Picture of the PPMS sample holder with a MgB_2 bulk

2.3.4.3 Magnetization by using Superconducting Coil (Néel Institute)

Magnetization with a superconducting coil is the most commonly used method to trap magnetic fields in large size bulks [39,101]. At Institute Néel the superconductor was magnetized with an Oxford superconducting coil which can generate fields up to 7 T. The measurements were carried out with a cryocooler provided by the LNCMI laboratory. Three temperature sensors (Cernox) and three Hall sensors (Arepoc) were mounted in the copper sample in order to measure the temperature and field homogeneity of the measured discs. The maximum diameter of the discs was 80 mm. Fig.2-11 shows a picture of the measurements system.

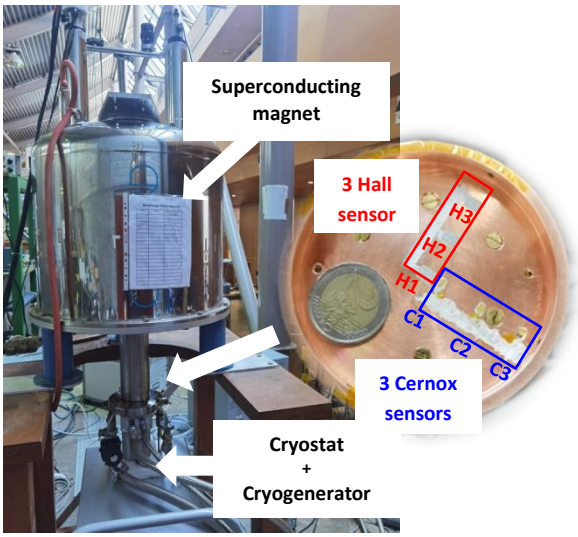

Fig.2-11 Picture of the device used for measuring the field trapped by superconducting discs at Institute Néel. The sample holder is shown on the right.

Chapter 3 Properties of MgB_2 processed by different precursor materials

This chapter discusses the SPS process of MgB_2 bulks and its optimization using different precursors listed below:

i) Ex-situ MgB_2 (purity >97%, 100 meshes, provided by PAVEZYUM advanced Chemicals, Turkey), namely lot1

ii) Ex-situ MgB_2 (<100 meshes, provided by abcr GmbH Germany), namely lot2

iii) In-situ mixing of Mg metal (99.8%, 325 mesh, provided by Alfa Aesar, USA) and amorphous B (99%, <400 nm, provided by PAVEZYUM), mixed in the molar ratio of 1:2.

iv) In-situ mixture of Mg (99.8%, 325 mesh, provided by Alfa Aesar, USA) and MgB_4 provided by the Korea Atomic Energy Research Institute, mixed in the molar ratio of 1:1.

v) In-situ mixture of Mg powder (99.9% purity, 200 meshes, provided by Furu-uchi Chemical Corporation) and carbon-encapsulated boron B/C (same amorphous nano boron from PAVEZYUM with 1.5 wt% of carbon) mixed in the molar ratio of 1:2, provided by Shibaura Institute Technology.

The precursors were divided into three groups for comparison: i) ex-situ powders from different suppliers, ii) different formulation syntheses, and iii) special treatment of boron powder. Firstly we have studied the basic information of each powder. Then high-density samples were fabricated, and their superconducting properties were comprehensively investigated.

3.1 Ex-situ powders investigations

3.1.1 Initial powder analysis

In this part, we have mainly investigated and compared the performances of ex-situ MgB_2 powders from lot1 and lot2. Fig.3-1 shows the XRD refinement results of the two precursors evaluated by the Maud software [102]. Both powders have a small quantity of MgO and hexagonal boron nitride (h-BN) phases, which was verified by following microstructure analysis. Some traces of magnesium were also detected in lot1.

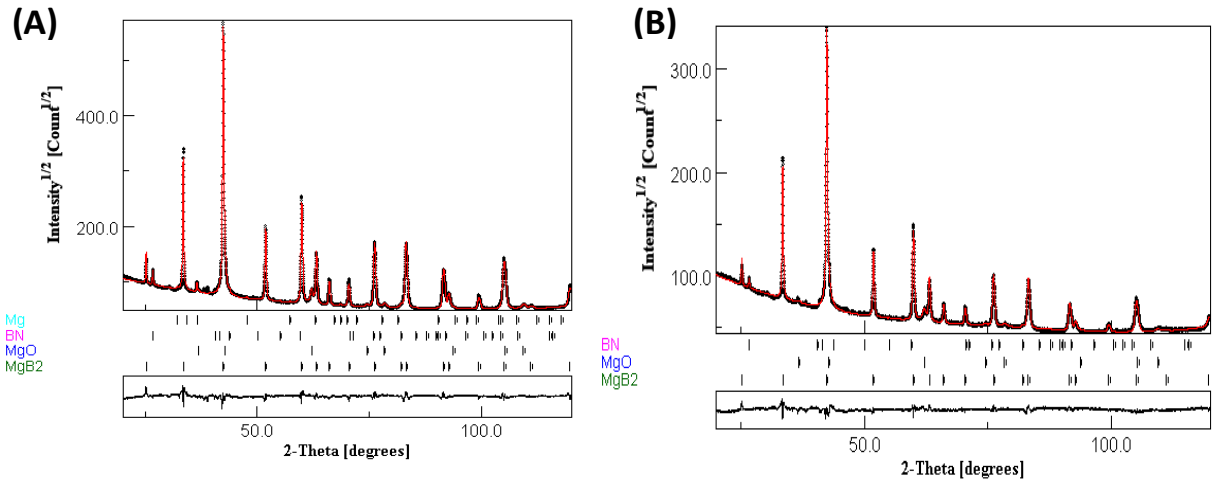

Fig.3-1 Refinement of XRD analysis of (A) lot1 and (B) lot2 ex-situ powder

Detailed refinement of their crystal structure is shown in table 3-1. The lattice parameters and crystallit size calculated for both lots are similar. Their lattice parameters correspond to the values reported in the review of Buzea C. [103], with a = 3.086 Å and c = 3.524 Å. Later we will compare these results to those obtained with the sintered bulks.

Table 3-1 Lattice parameters, *c/a* ratio, amount of each phase and crystallite size of the initial powders and the fabricated bulks

Reference	a (Å)	c (Å)	$\Delta c/a$	MgB_2 (wt%)	BN (wt%)	MgO (wt%)	Mg (wt%)	MgB_4 (wt%)	crystallite size (nm)
lot1	3.0858	3.5238	1.1419	93.66	1.35	4.59	0.39	-	92
lot2	3.0861	3.5233	1.1417	93.43	1.05	5.52	-	-	82
A1	3.0846	3.5277	1.1436	81.8	1.35	6.5	-	10.34	93
A2	3.0853	3.5265	1.1430	78.19	1.06	6.47	-	14.29	80

Fig.3-2 shows the microstructure of these two precursors. Similar small spherical MgB_2 grains ranging from 200-1000 nm can be observed in both powders. The size of the grains observed by SEM is quite different from that estimated by the XRD refinements. Since the XRD refinements give the approximate average crystallite size only, the results cannot be considered as the actual size of the grains if they are inhomogeneous and irregular grains [104]. Nevertheless, in some cases, this value could be correlated with the critical current density J_c. Some platy particles were observed in lot2 powder (see the inset in Fig.3-2(B)). In addition, tiny white particles present in both powders are the impurity phase MgO.

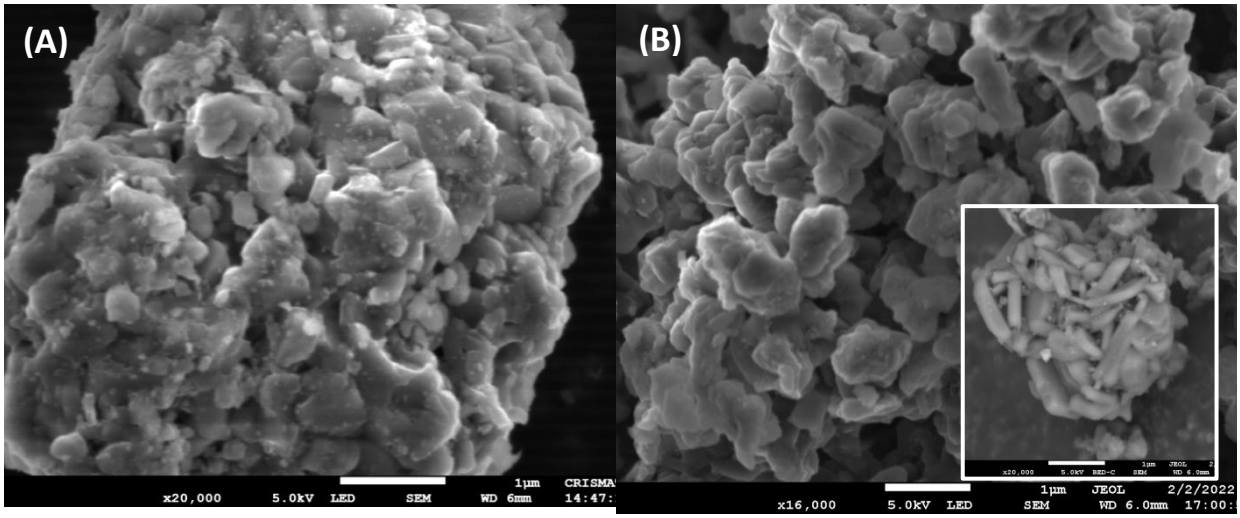

Fig.3-2 SEM micrographs of ex-situ powders supplied by (A) PAVEZYUM, Turkey, lot1 and (B) abcr, Germany, lot2. The inset in Fig.3-2(B) shows the platy structure of MgB_2 grains present in lot 2 powder.

The Energy Dispersive X-Ray Spectrometer (EDS) analysis of lot1 powder is shown in Fig.3-3. Two zones were selected to estimate their chemical compositions. The main phase in region 1 is MgB_2. The dark grey zone 2 correspond to the impurity phase BN and the presence of MgO is evidenced in all areas.

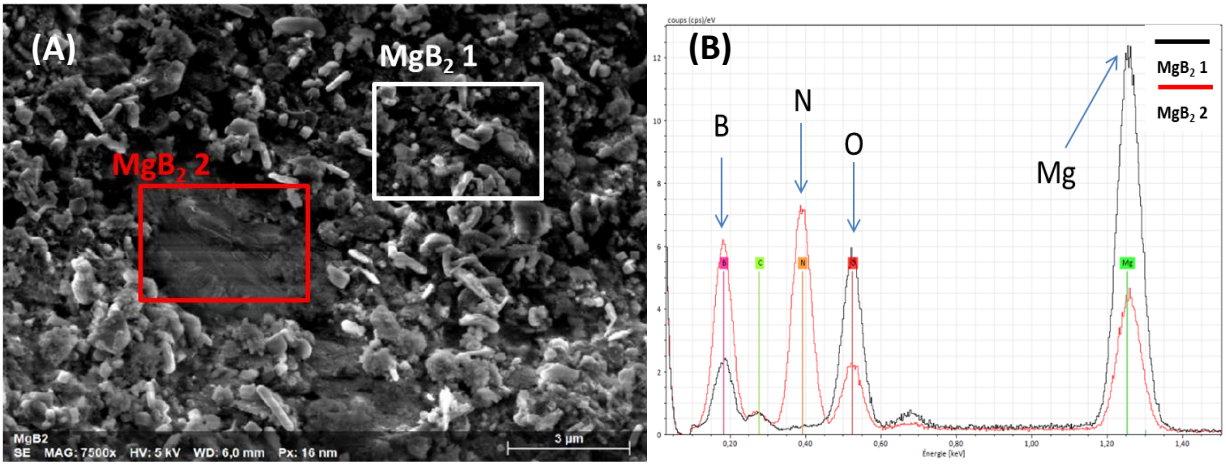

Fig.3-3 EDS analysis of lot1 ex-situ powder

3.1.2 Sample fabrication

Two samples, labelled as A1 (from lot1 powder) and A2 (from lot2 powder), were fabricated using the same processing conditions. For this purpose, 1.5 g of powder was weighted and loaded into a 20 mm diameter graphite mold. Graphite foils were wrapped alongside the inner wall of the mold and inserted between the powder and the two punches to facilitate demolding. The samples were sintered in DC mode with high-intensity current pulses (2000

A, 4 V) and a 100 MPa uniaxial pressure under dynamic vacuum (10^{-3} bar). The sintering temperature was 1000°C for 30 minutes. The heating and cooling rate was 100°C/min. During the whole process, the temperature, the applied pressure, the shrinkage curve as well as the piston speed were recorded. Before characterization the bulks were polished to remove the carbon traces from the graphite foils. The density of both samples was 2.56 g/cm^3, corresponding to 98% of the theoretical value.

3.1.3 Structure and microstructure characterizations

The structural and microstructural analyses carried out with these samples were correlated with their superconducting properties, in particular their critical current densities, J_c. Fig.3-4 shows the XRD pattern of the two bulks. Compared with the initial powders, the MgO content increases from 4.59% and 5.52 % to 6.5% and 6.47%, respectively, for A1 and A2. Otherwise, the peak (around 26.8°) corresponding to the BN phase overlaps with that corresponding to the carbon due to the residual graphite foil. According to the phase diagram phase of BN [105], this compound is very stable up to 2500°C. Compared to the refinement results shown in table 3-1, this peak seems to correspond to the unreacted BN phase in the initial powder. The lattice parameter *a* decreases and *c* increases after sintering for both bulks, which maybe due to the sintering pressure applied and the growth of MgO precipitates in the MgB_2 grains. Furthermore, anisotropy is visible in their XRD pattern and will be discussed in the final chapter. Another secondary phase, MgB_4 is visible. It is due to the decomposition of MgB_2 at high temperature. The lower amount of MgB_4 in A1 could be explained by the traces of Mg present in lot1 powder. The crystallite size does not change as compared to that of the precursors.

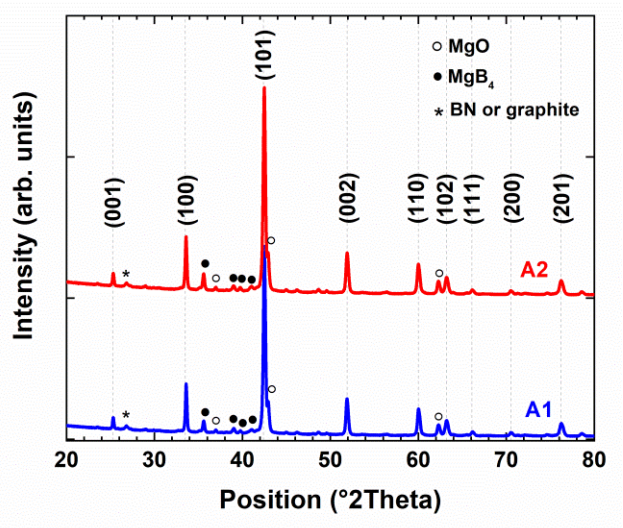

Fig.3-4 XRD analysis of MgB_2 bulks sintered with lot1 and lot2 ex-situ powders

As shown in Fig.3-5, the A1 sample compared to the A2 seems to have smaller MgB_2 grains with larger MgO precipitates, which might have a flux pinning enhancing effect as was verified by following J_c measurements (see section 3.1.4).

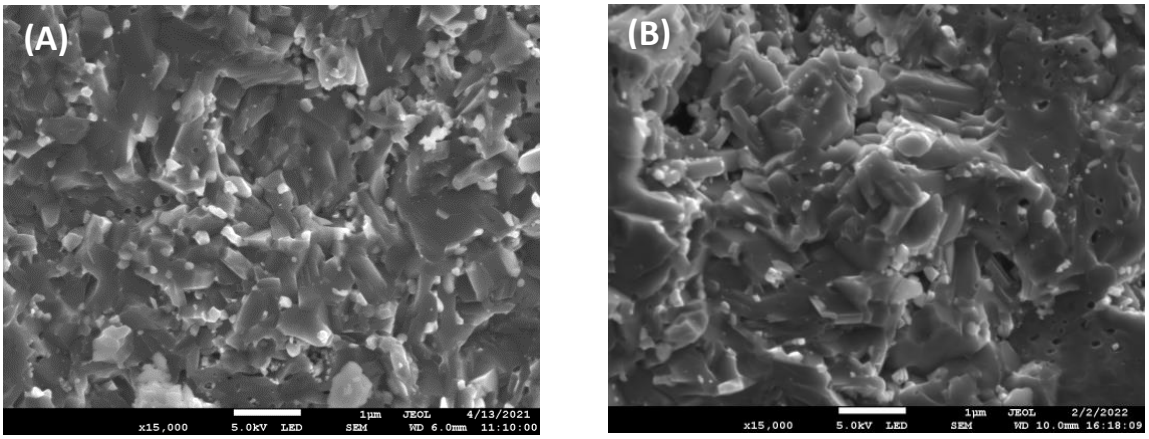

Fig.3-5 SEM micrographs of fractured surfaces of (A) A1 and (B) A2 sample

3.1.4 Analysis of the superconducting properties

Small specimens with dimensions 1.79 x 2 x 0.88 mm^3 and 1.51 x 1.55 x 0.88 mm^3 were cut from the two fabricated bulks to investigate their superconducting properties with the SQUID magnetometer. Fig.3-6 shows the normalized magnetic moment-temperature curves of A1 and A2. The measurements were made while applying a 2 mT external magnetic field. A low

transition width (ΔT < 1 K) at the onset of the superconducting transition, $T_{c,\,onset}$ = 38 K, is observed in both samples. Their critical current density was estimated from the magnetization hysteresis cycles at 20 K and plotted in Fig.3-6(B) as a function of the applied field. A high J_c value equal to 4 10^5 A/cm^2 in self-field can be observed in both bulks, probably due to their high packing factor. However, the J_c of A2 decreases slightly faster than that of A1 above 1.5 T, probably because of the lack of defects playing the role of pining centers in this sample. The pinning mechanisms in the investigated bulks will be discussed later.

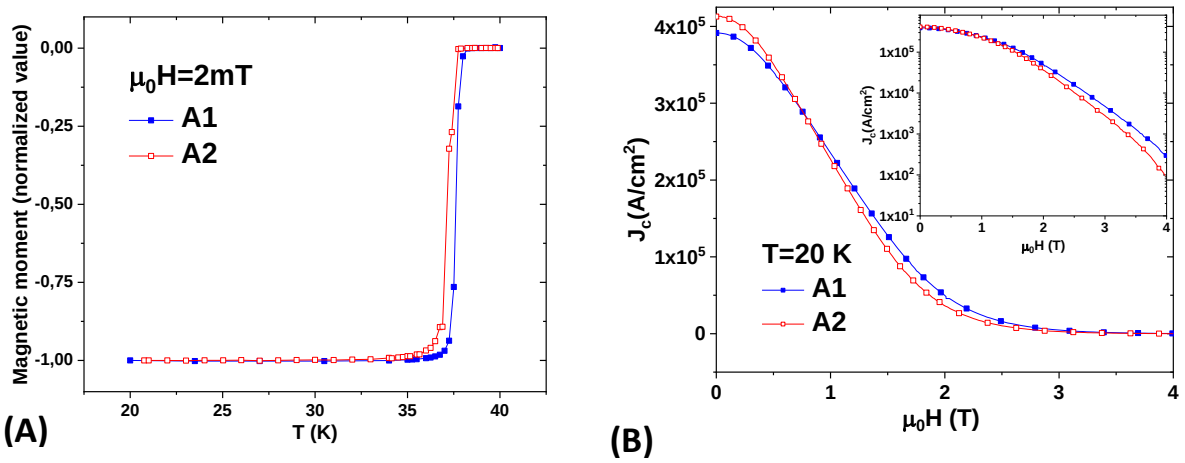

Fig.3-6 (A) Normalized magnetic moment as a function of the temperature. (B) Magnetic field dependence of the critical current density J_c at 20 K. The inset shows the same curves on a logarithmic scale.

3.2 Comparison of bulks made with different formulation synthesis

Three formulations were used here to prepare MgB_2 bulks:

a) Ex-situ MgB_2

b) In-situ $Mg+2B \longrightarrow MgB_2$

c) In-situ $Mg+MgB_4 \longrightarrow 2MgB_2$

The section is divided into two parts:

i) pre-investigation for the various formulation synthesis and

ii) Characterization of the samples fabricated.

3.2.1 Initial powder analyses

We have employed ex-situ MgB_2 powder of lot1 for this study. The magnesium powder used in the two in-situ mixtures was the same. It is well-known that the quality of boron plays an important role for improving the critical current density, J_c [94,106], and that amorphous nano boron is one of the best candidates for the reactive sintering of MgB_2 bulks [37,106]. The microstructure of the nano boron we have used, shown in Fig.3-7, consists of spherical grain the size of which ranges between 100-300 nm. The MgB_4 powder was provided by the group of Prof. C-J. Kim (Korea Atomic Energy Research Institute). The detailed fabrication process of this powder and its characteristics were reported elsewhere [107].

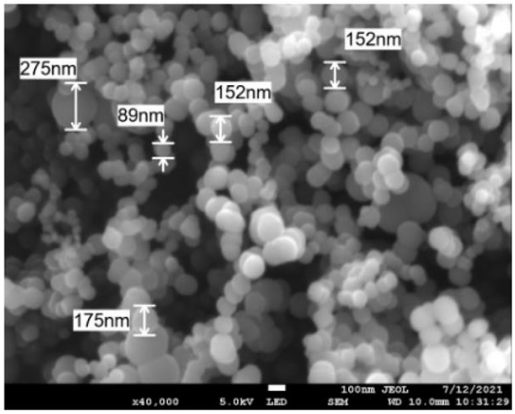

Fig.3-7 SEM micrographs of amorphous nano boron.

The phase transformation of the three precursors was investigated using Differential Scanning Calorimetry (DSC), with a heating rate of 5°C/min under Ar atmosphere. Thermo-analytical curves are shown in Fig.3-8. These powders, even the ex-situ one, have an exothermal peak around 500°C, which could be explained by the redox reaction between the amorphous impurity B_2O_3 and Mg [88,94]:

$$4Mg(s) + B_2O_3(l) \longrightarrow 3\,MgO(s) + MgB_2(s)$$

The B_2O_3 phase was already present in the precursors and could react with Mg due to its low melting point (≈450°C). The second exothermal reaction visible in the Mg+2B powder around 650°C, indicates the formation of the MgB_2 phase. Otherwise, the Mg and MgB_4 powder shows no change below 800°C. Finally, a weak endothermal peak can be found in the two in-situ powders around 650°C. It is related to the melting of Mg.

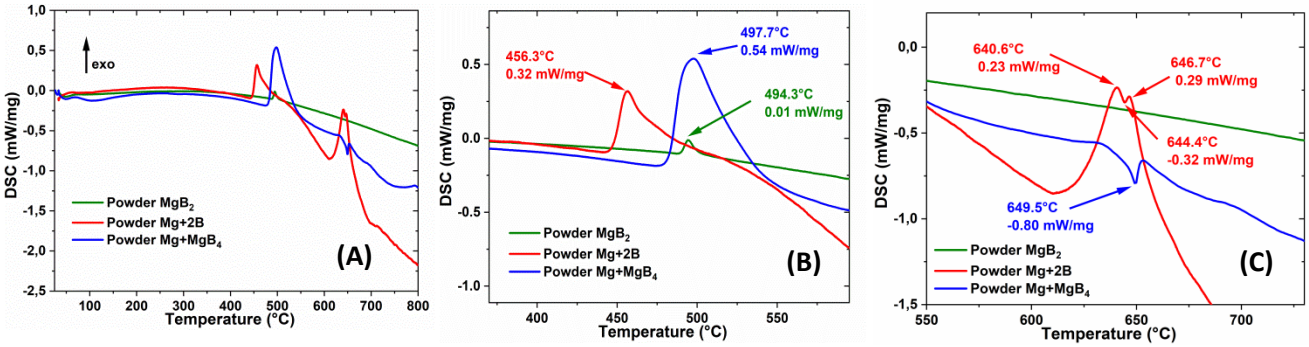

Fig.3-8 (A) DSC curves of the initial powders and the magnification of (B) 370-590°C and (C) 550-730°C.

Fast sample preparation at different temperatures was achieved in order to determine the sintering conditions resulting in dense samples. A mass of 0.3 g of each powder was loaded into a graphite mold with a diameter of 10 mm. All samples were sintered between 500°C and 1000°C under 60 MPa uniaxial pressure for 20 minutes. The obtained bulks were not compact (relative density <80%) except the samples sintered above 950°C. To further understand the reaction process of these powders, X-ray analyses of the initial powders and of the fast sintered pellets were carried out. MgB_2 is synthetized at 600°C (Fig.3-9(B)) for the Mg+2B samples and at 700°C for the Mg+MgB_4 ones (Fig.3-9(C)). The MgB_2 peaks of the ex-situ MgB_2 bulks do not significantly change with the variation of the sintering temperature. However, MgB_4 and MgO impurity phases are present at high temperatures, as they are in the samples of the Mg+2B group (Fig.3-10(A) and (B)). The increase in the amount of MgO is related either to the oxidation of Mg during the sintering process or to the reaction between B_2O_3 and Mg, as mentioned earlier. The MgB_4 phase usually appears at high temperatures and is due to the evaporation of Mg. On the contrary, the Mg+MgB_4 samples sintered at 700°C presents unreacted Mg peaks, while the MgB_4 peaks decrease with increasing temperature (Fig.3-10(C)).

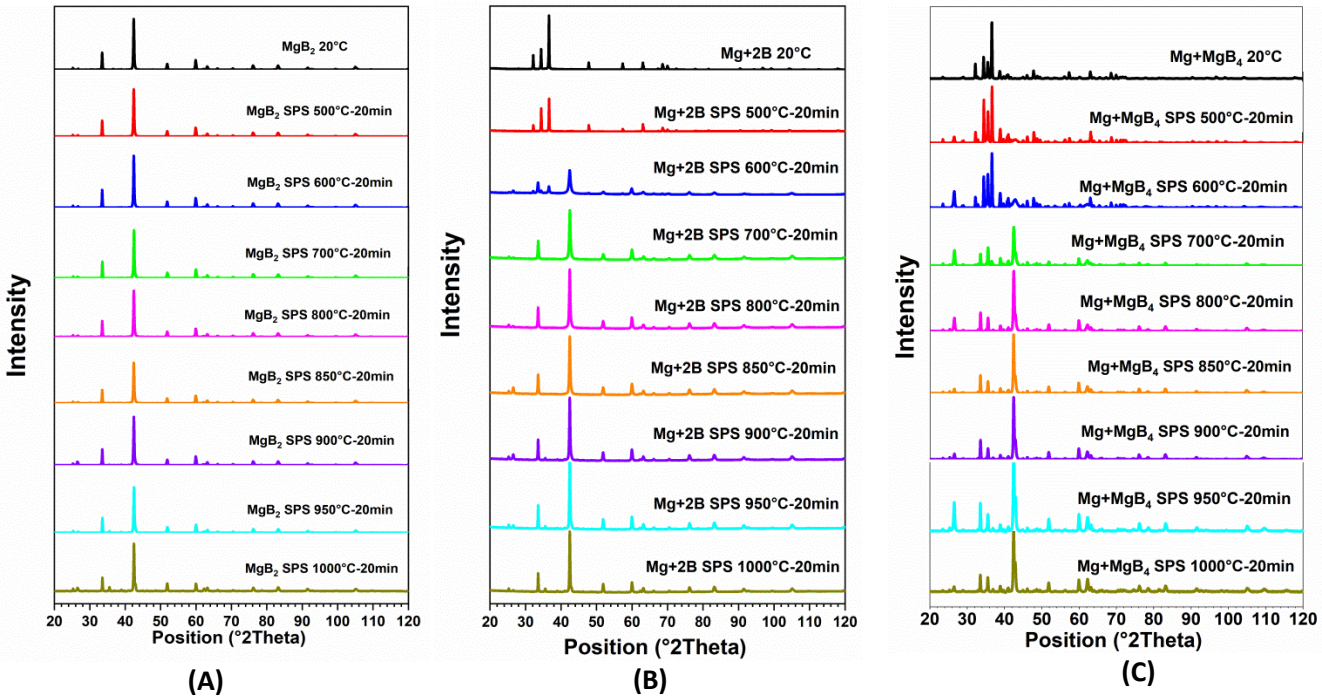

Fig.3-9: XRD of A) MgB_2 B) Mg+2B and C) Mg+MgB_4

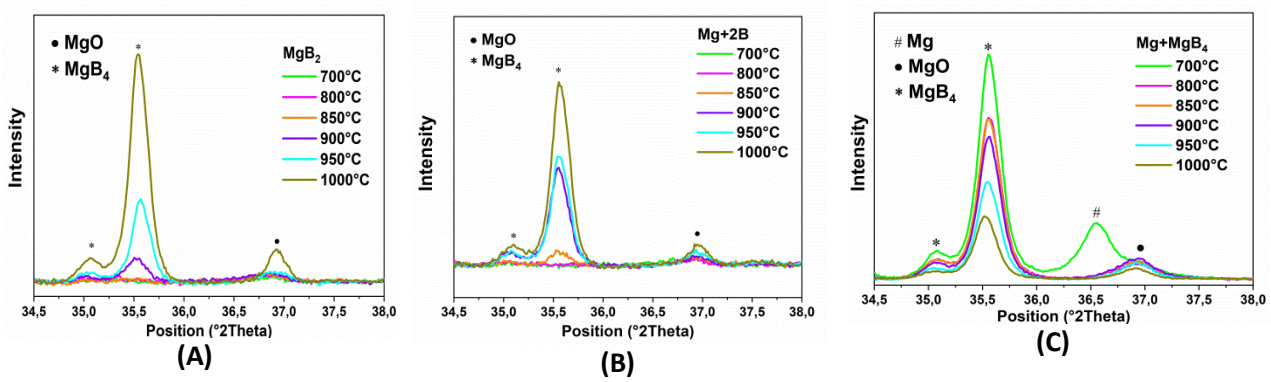

Fig.3-10: Local magnification of the MgO, MgB_4 and Mg peaks of A) MgB_2 B) Mg+2B and C) Mg+MgB_4 series sample sintered at 700-1000°C

The magnetic moments of the selected samples are plotted as a function of the temperature in Fig.3-11. The onset of the superconducting transition, $T_{c,\ onset}$, of the Mg+2B samples increases with the sintering temperature and saturates around 39 K. The enhancement of the T_c values indicates the improvement of the material crystallinity. The superconducting transition width (ΔT_c) decreases as the temperature increases. The ex-situ MgB_2 and Mg+MgB_4 samples have a large ΔT_c when the sintering temperature is below 950°C, which can be attributed to their poor density. An intriguing result is that the ex-situ bulks sintered with the MgB_2 powder that are brittle, which is an indication of a low density, don't show a complete transition at 10 K if the sintering temperature is below 900°C, while the in-situ ones sintered with the Mg+2B powder at 600°C are superconducting below T=33 K. This suggests that the connection between the MgB_2 grains of the ex-situ powder is possible at or above 900°C only. Finally, the results show that to avoid an excessive impurities content and to obtain a high packing factor as well as a good crystallinity of the samples, a temperature of 950°C and an applied pressure of 100 MPa are the best sintering conditions.

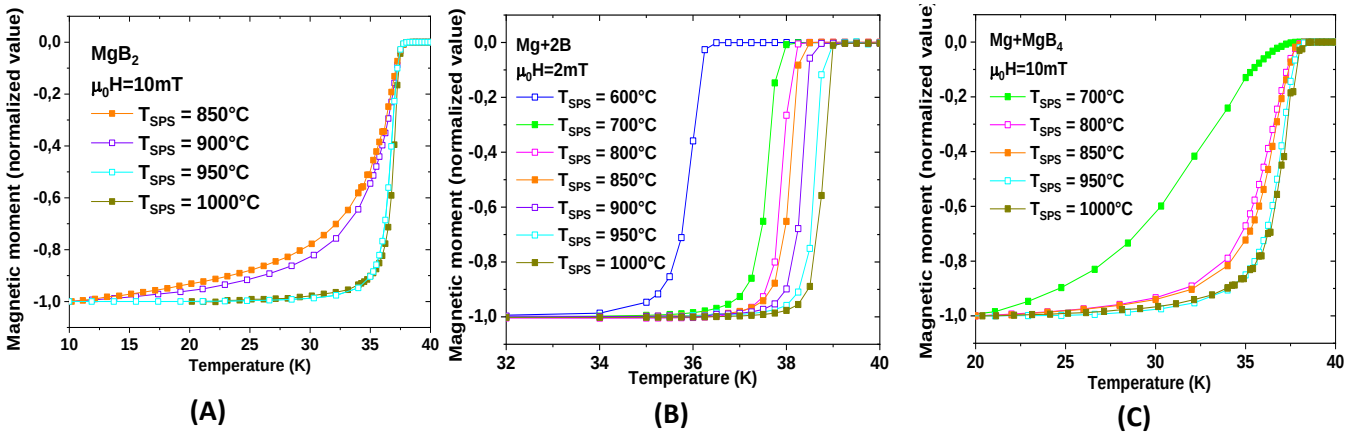

Fig.3-11: Normalized magnetic moment - temperature curves of A) MgB_2, B) Mg+2B and C) Mg+MgB_4 series.

3.2.2 Dense sample preparation

Three 20 mm diameter samples (named B1, B2 and B3) were fabricated with 1.5 g of the different precursors. As mentioned in chapter 2, an insulating coating helps to enhance the current intensity and thermal uniformity during the sintering of a conductive powder. The

MgB_2, Mg+2B and MgB_4 powders are conductive at high temperatures. Hence, all samples were prepared with the protocol described below, using graphite dies coated with insulating BN carbon foils:

i) 500 °C + 60MPa / 10 minutes (compaction + pre-synthesis)

ii) 650 °C + 80MPa / 45 minutes (synthesis)

iii) 950 °C + 100MPa / 30 minutes (sintering)

iv) 1000 °C + 100MPa / 5 minutes (densification)

The role of the two first steps is to avoid magnesium evaporation. The obtained bulks are labelled as B1 for the sample fabricated with the commercial MgB_2 (lot1) powder, B2 for the sample made with the Mg + 2B mixture and B3 for the bulks made with the Mg + MgB_4 powder. The relative densities of B1, B2 and B3 were 99%, 96%, and 92%, respectively. The different packing ratios can be related to the particles sizes and shapes of the starting powders and to the chemical reactions occurring in the Mg + 2B and the Mg + MgB_4 powders during the processing stage. Fig.3-12 shows the sintering stage of these samples as suggested by the piston movement. The MgB_2 phase of the two in-situ powders was synthesized at 650°C, before sintering at 950°C. We emphasize that the densification process of the two in-situ samples was still ongoing at 1000°C, which is the reason why their density is lower than that of the ex-situ bulk.

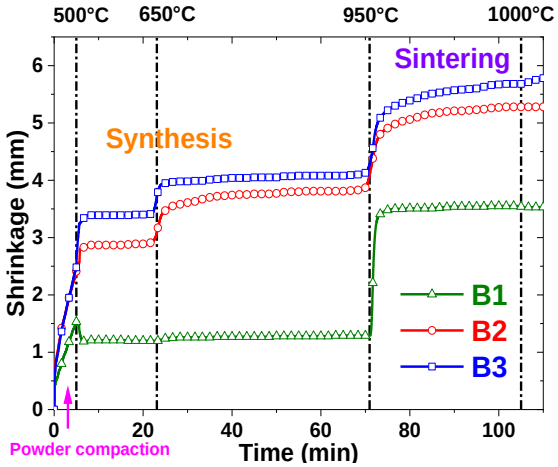

Fig.3-12: Displacement of the piston vs. sintering time curves.

3.2.3 Structure and morphological properties

The XRD patterns (Fig.3-13(A)) show that the major peaks of the three sintered bulks are due to the MgB_2 phase with traces of MgO and MgB_4, which appear at high temperatures. The presence of Mg was also observed in the B3 sample, which was fabricated using the mixture of Mg+MgB_4 powder and surprisingly, the MgB_4 peaks of two in-situ samples are weaker than that of the ex-situ sample (see Fig.3-13(B)). The differences with the fast sintering samples, can be explained by the 2 additional steps of the process, which suppress Mg

evaporation. Another possibility is that the initial powder is not evenly mixed, resulting in Mg residues.

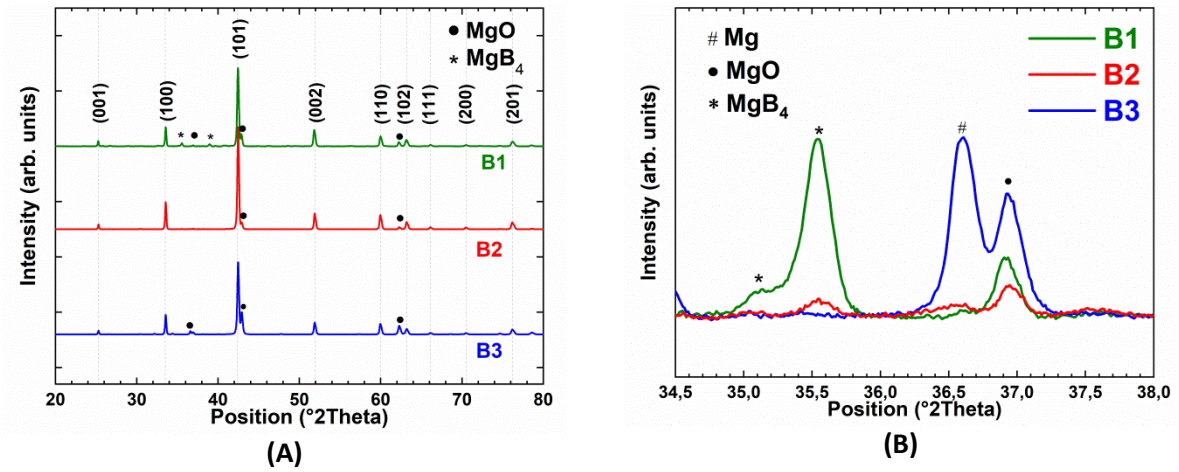

Fig.3-13: (A) XRD pattern of three bulks. (B) Local magnification of the MgO, MgB_4 and Mg peaks.

The detailed parameters after refinement are shown in table 3-2. According to their lattice parameters and estimated crystallite size, the MgB_2 grains in the ex-situ sample B1 are more slender and larger than the others. B3 has the smallest grains, but a high quantity of MgO is observed. Compared to the XRD patterns of the initial powders and fast sintered samples, the significant increase of the oxide phase can be related to the first sintering step at 500°C, during which Mg has reacted with B_2O_3. In addition, we observe that sample B1 has larger crystallites than A1. Even if the sintering temperature of B1 is lower than that of A1, the BN coating of the carbon foils enhances remarkably the temperature in the powder during the sintering process of B1, resulting in an increased growth of the crystallites.

Table 3-2 Lattice parameters, c/a ratio, amount of each phase and crystallite size of the fabricated bulks

Reference	*a* (Å)	*c* (Å)	*c/a*	MgB_2 (wt%)	MgB_4 (wt%)	MgO (wt%)	Mg (wt%)	crystallite size (nm)
B1	3.0837	3.5273	1.1439	81.34	11.66	7	-	160
B2	3.0855	3.5249	1.1424	96.35	0.56	3.08	-	146
B3	3.0849	3.5245	1.1425	79.91	-	18.04	1.9	127

The microstructure of the fracture surface of each bulk is shown in Fig.3-14. The chemical compositions were examined with back-scattered electron (see Fig.3-14(A-C)), while the topographic view of the MgB_2 grains was observed with secondary electrons (see Fig.3-14(D-E)). The SEM images reveal the poor density of the B3 sample. Three colors zones are visible in samples B1 and B2 (Fig.3-14(A) and (B)). The white regions are MgO phases, and the dark grey zones are MgB_4 with pores created by the evaporation of magnesium. The

presence of the excess oxide phases in these two samples is quite different. Sample B1, sintered directly from the commercial MgB_2 powder, has large MgO particles mainly located at the MgB_2 grain boundaries (Fig.3-14(D)), resulting in a reduced grain connectivity [94]. Sample B2, prepared after reactive sintering, has a large amount of MgO nano-particles agglomerates in the MgB_2 phase, which are possible volume pinning centers. In addition, B1 has grains the size of which is around 1 μm and are larger than those of the other samples, as well as the highest relative density. Small size particles, defects, inter- and intragranular MgO nano-precipitates can be observed in B3 (Fig.3-14(F)), indicating a large number of pinning centers.

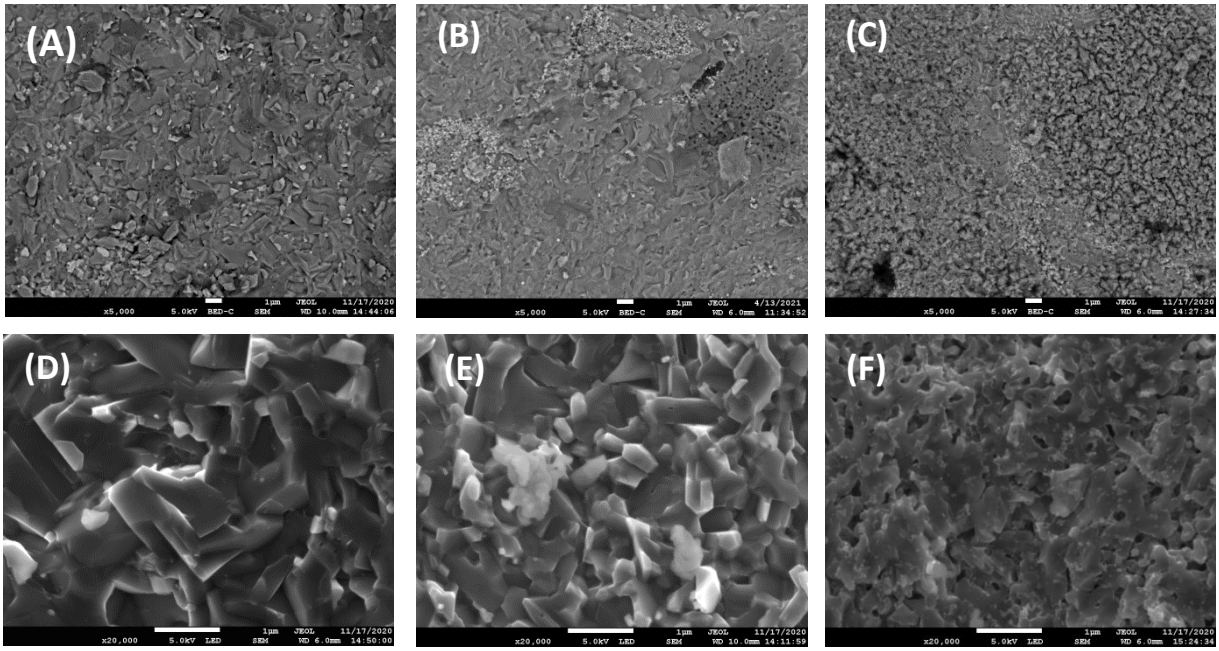

Fig.3-14: SEM micrographs of fractured surfaces of A) B1, B) B2 and C) B3 samples and magnification of MgB_2 grains in the D) B1, E) B2 and F) B3.

3.2.4 Superconducting properties

The resistivity, ρ, of the samples as a function of the temperature measured with the PPMS is plotted in Fig.3-15(A). The results show that the resistivity of the ex-situ sample B1 is higher than those of the in-situ samples and that B2 has the lowest resistivity at room temperature, which indicates that it presents the best grain connectivity. Table 3-3 shows the residual resistivity ratio ($RRR = \rho_{300K} / \rho_{40K}$) of the samples and their electrical connectivity estimated with the Yamamoto expression [108],

$$K = \frac{\Delta\rho_g}{\Delta\rho} \quad \text{[Eq.3.1]}$$

In Eq.[3.1], $\Delta\rho = \rho_{300K} - \rho_{40K}$ and $\Delta\rho_g = \rho_{g\_300K} - \rho_{g\_40K}$ are respectively the differences in the resistivity of the samples and in that of the MgB_2 grains between 300 K and 40 K. According to [108], the average $\Delta\rho_g$ in randomly oriented polycrystalline MgB_2 samples is equal to 6.32 μΩ cm. The high *RRR* and *K* values of the B2 sample confirm that it presents the best

crystallinity, purity and connectivity. The inset of Fig.3-15(A) shows the superconducting transition region. The critical temperature of B2 is above that of B1 and B3, which show the same offset temperature. We can suppose that the magnesium diffusion at low temperature occurring during the synthesis of B2 is useful to improve the crystallinity and the contacts between the grains.

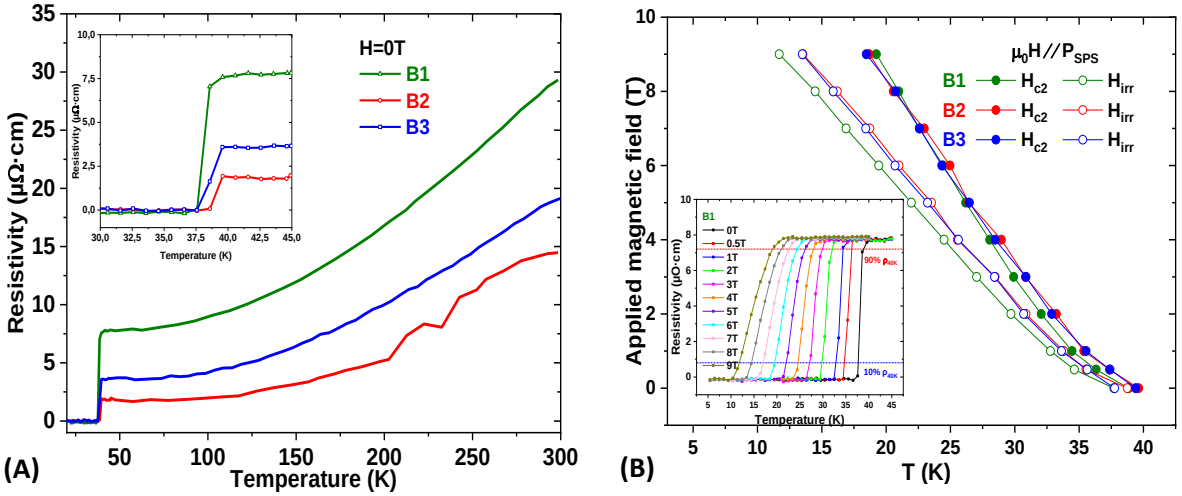

Fig.3-15: (A) Temperature dependence of the resistivity at 0 T of samples B1, B2 and B3 measured with a 5 mA direct current. The inset shows the magnified superconducting transition. (B) Temperature dependence of H_{c2} and H_{irr} for the three samples. H_{c2} and H_{irr} were determined from 90% and 10% of ρ_{40K}. The inset shows the resistivity transition of the B1 ex-situ sample at fields ranging between 0 T and 9 T and orientated parallel to the SPS sintering pressure.

The upper critical magnetic field, H_{c2} and the irreversibility magnetic field, H_{irr} were determined from ρ_{40K} measured at various magnetic fields as reported elsewhere [88,94]. From measurements of the resistivity carried out from 5 K to 40 K at fields ranging between 0 T and 9 T (direction parallel to the pressure applied during the SPS sintering process), its temperature dependence could be determined and is plotted in Fig.3-15(B). The results show that H_{c2} is almost identical for the three samples but that H_{irr} is lower for B1 than for the other samples.

Table 3-3 Offset critical temperature, measured resistivity values, residual resistivity ratios (*RRR*), connectivity (K), irreversibility magnetic field, H_{irr} and the upper critical magnetic field, H_{c2}

Sample	T_c (K)	ρ_{300K} (μΩcm)	ρ_{40K} (μΩcm)	*RRR*	*K*	H_{irr} at 20 K (T)	H_{c2} at 20 K (T)
B1	36.6	29.3	8.0	3.66	0.297	5.8	8.6
B2	38.6	14.7	1.9	7.74	0.492	6.4	8.3
B3	37.6	19.1	3.6	5.31	0.407	6.3	8.3

Specimens with dimensions of 1.5 x 1.51 x 1.34, 1.34 x 1.5 x 1.3 and 1.49 x 1.49 x 1.6 mm^3, respectively, were cut from the B1, B2 and B3 bulk samples. Their magnetic moment, as a function of the temperature, was measured with the SQUID magnetometer. The resulting

normalized values are plotted in Fig.3-16(A). The onset of the superconducting transition, $T_{c,onset}$ occurs at 37.75, 39 and 38.5 K for B1, B2 and B3, respectively, with a narrow transition width (ΔT < 1 K). Otherwise, B2 presents the highest offset temperature, while this temperature is almost the same for B1 and B3, as previously shown by the resistivity measurements. Fig.3-16(B) shows the critical current density dependence of the samples on the magnetic field applied at 20 K. B2 shows the best critical current density (J_c =5 10^5 A/cm^2) in self-field, which could result of its excellent grains connectivity. Consistently, the low J_c of B1 can be attributed to a low grain connectivity, while that of B3 is probably due to the low density of this sample. An effect of the microstructure on the critical current density is visible at high field. The critical current density of B3 above 2 T is higher than that of B1 and higher than that of B2 above 3 T. The good J_c of B3 in high field suggests a strong pinning of the vortices that can be attributed either to porosities and nano-precipitates or to a large quantity of grain boundaries.

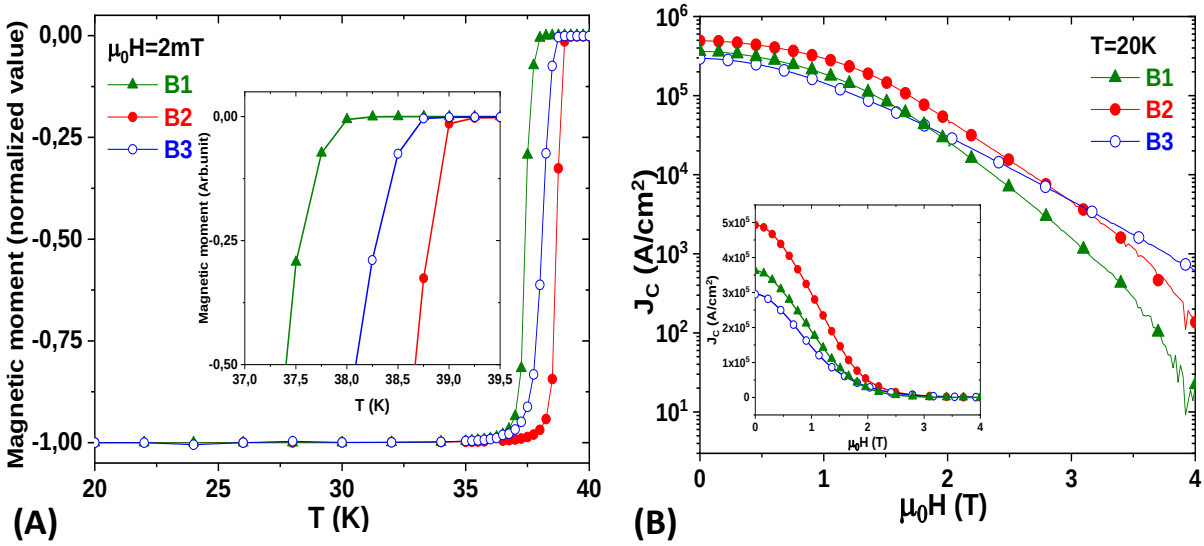

Fig.3-16: (A) Normalized magnetic moment of samples B1, B2 and B3 as a function of the temperature. The inset shows the onset of superconducting temperature. (B) Magnetic field dependence of the critical current density J_c at 20 K. The inset shows the same curves on a linear scale.

3.3 Characterization of bulks prepared with carbon-encapsulated boron

For J_c enhancement, chemical doping or substitution [35,56–58] is a practical and easy technique. Among various chemical dopants, carbon was one of the most effective choice. While carbon as dopant can be provided by various sources, an uniform carbon distribution has always been an issue [109], leading to nonuniform superconducting performances that is not desired. Hence, research focusing on achieving uniform carbon distribution has been carried out in recent decades. One famous recent technique consists in coating boron grains with carbon, resulting in a precursor named carbon-encapsulated boron. Several groups have employed this specific boron powder, which was prepared via pyrolysis of diborane gas (B_2H_6) under inert conditions, and have obtained an uniform carbon distribution as well as a high J_c. Some studies have reported that a low carbon amount around 1.5 wt% is optimum for producing good J_c [110,111]. This section compares the performances of the in-situ mixture

Mg+2B to the mixture of Mg and carbon-encapsulated boron (Mg+2B/C) prepared by Prof. M. Muralidhar group (Shibaura Institute Technology).

3.3.1 Initial powder analyses

The microstructure analyses of the Mg+2B/C powder is shown in Fig.3-17. Plate-like magnesium grains around 20 µm and spherical carbon-encapsulated boron grains ranging from 50-300 nm (inset of Fig.3-17) were observed in the mixture. 4.7 and 4.5 wt% oxygen were detected in zone1 and in zone2 by EDS analysis. However, some other regions with an oxygen content reaching 39 wt% were also observed.

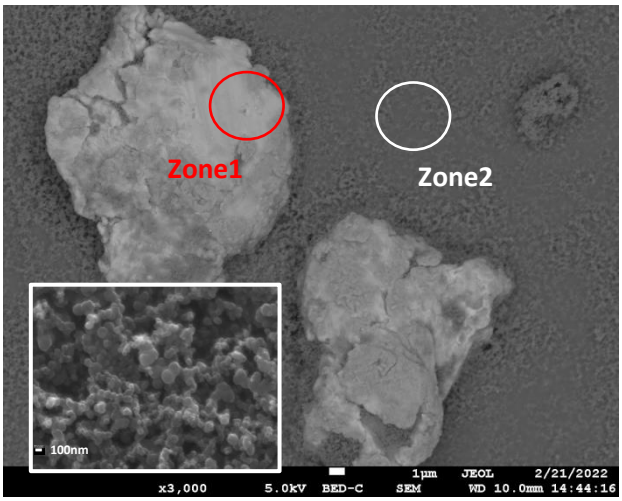

Fig.3-17: Microstructure of Mg+2B/C powder provided by Shibaura Institute Technology. The inset shows the magnified carbon-coated nano boron grains.

The thermos-analytical curves of Mg+2B and Mg+2B/C are plotted in Fig.3-18. As in other in-situ powders an endothermal peak (see Fig.3-8(C)) shows that the magnesium melts at 650°C in the Mg+2B/C mixture. However, an extreme exothermal peak around 620°C is also present. We have repeated the experiment (powder Mg+2B/C_bis) and obtained almost the same result, which shows that this result was not an accident. As reported by other papers [57,112], this peak might correspond to the solid-solid reaction between Mg and B, which occurs at a lower temperature than the liquid-solid reaction according to the Gibbs free energy [88,113]. The authors have also noted that the carbon-coated amorphous boron is more active than amorphous boron and can better react with solid Mg.

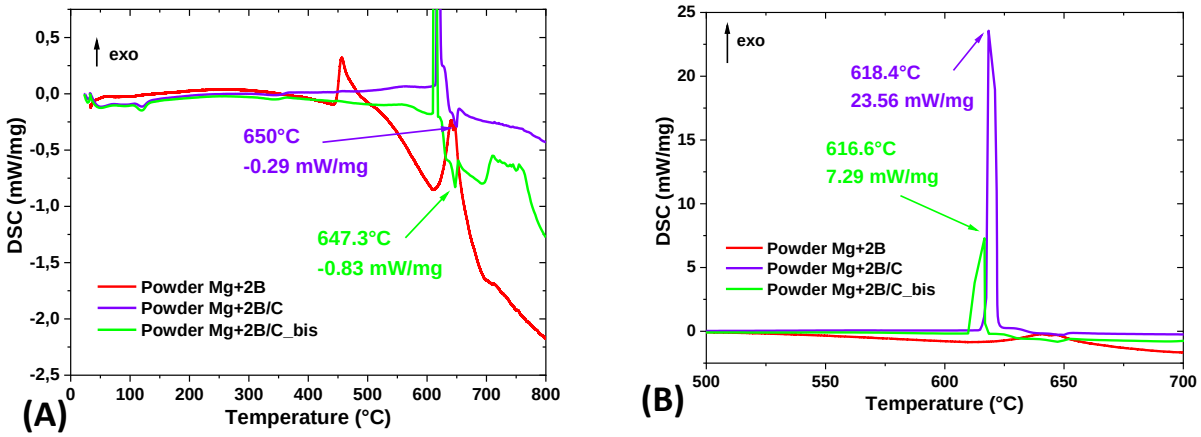

Fig.3-18: (A) DSC curves of the precursors and (B) the magnification between 500 and 700°C

3.3.2 Sample preparation

Considering the results reported in section 3.2.2, we have used the same quantity of precursors (1.5g) and the 20 mm diameter graphite die without BN coating in the graphite foils to avoid excessive grain growth. We have also changed the duration of the first and the second steps to reduce the total sintering time:

i) 500 °C + 60MPa / 15 minutes (compaction + pre-synthesis)

ii) 650 °C + 80MPa / 20 minutes (synthesis)

iii) 950 °C + 100MPa / 30 minutes (sintering)

iv) 1000 °C + 100MPa / 5 minutes (densification)

Two bulks named C1 and C2 were prepared with the mixtures Mg+2B and Mg+2B/C, respectively. Their relative densities were 2.48 and 2.17 g/cm^3, i.e., 95% and 83%, respectively, of the theoretical density. The sintering process is plotted in Fig.3-19. The shrinkage of the C1 sample was still ongoing after being synthesized at 650°C for 20 minutes. Based on the dramatical drop movement of the piston, the reaction of the C2 powder seems to have stopped at the beginning of this step. This behavior can be related to a thermal analysis suggesting that the MgB_2 phase from the Mg+2B powder has formed mainly at 650°C, while the Mg+2B/C powder has violently reacted at 620°C. Moreover, the insufficient densification duration of C2 has resulted in its weak density.

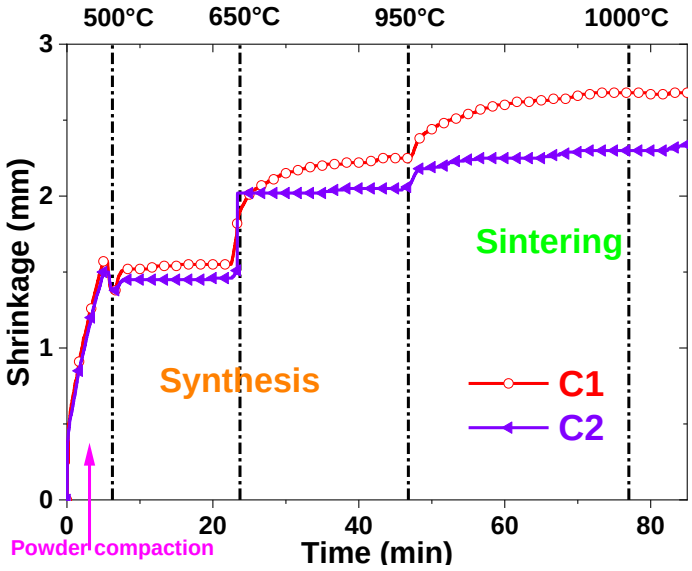

Fig.3-19: Displacement of piston vs. sintering time curves.

3.3.3 Structure, microstructure and superconducting properties

From the XRD patterns of the two bulks (Fig.3-20), it is clear that C1 has a better crystallinity than C2, as shown by its high-intensity and sharp peaks. Extremely high amounts of second phases are visible in C2 (see table 3-4). The presence of MgO can be explained by the oxide phases present in the initial powder and an oxidation reaction during the sintering process. The MgB_4 phase is observed in both bulks and is due to the high sintering temperature. This suggests that amorphous Mg in the Mg+2B/C mixture evaporates more quickly than in the Mg+2B one, leading to a larger quantity of the MgB_4 phase in the C2 sample.

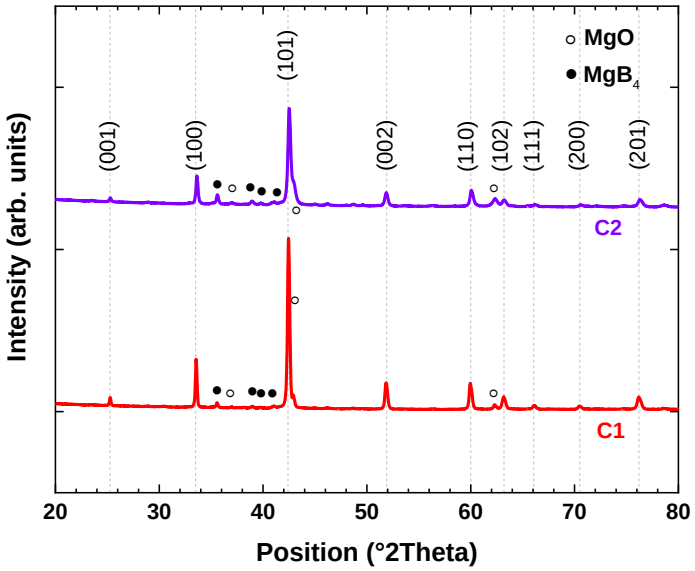

Fig.3-20: XRD pattern of C1 and C2 bulk samples

The lattice parameter *a* of C2 is reduced as a result of the carbon substitution to boron since carbon has a smaller atomic radius than boron [62]. A slight increase of the *c*-axis is also observed. Furthermore, C2 shows a smaller crystallite size as confirmed by the following microstructure analysis.

Table 3-4 Lattice parameters, c/a ratio, amount of each phase and crystallite size of the fabricated bulks

Reference	*a* (Å)	*c* (Å)	*c/a*	MgB_2 (wt%)	MgB_4 (wt%)	MgO (wt%)	crystallite size (nm)
C1	3.0863	3.5273	1.1429	89.17	6.66	4.16	134
C2	3.0822	3.5291	1.145	66.93	17.08	15.99	73

The microstructures of the MgB_2 grains in both samples are shown in Fig.3-21, revealing a large quantity of pinning centers in the C2 bulks. The grains in C2 are well-connected without distinct grain boundaries, and numerous tiny nano white particles are visible, which could be carbon or oxide phases.

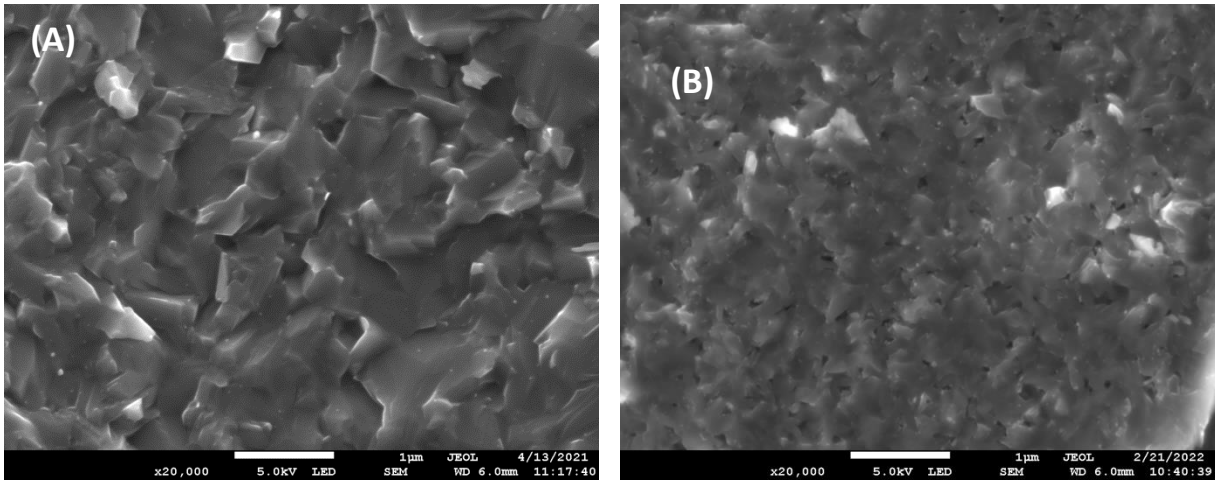

Fig.3-21: morphology of MgB_2 grains in (A) C1 and (B) C2 bulks

The measurement of the superconducting properties has been carried out on specimens with dimensions 1.56 x 1.58 x 1.81 mm^3 and 1.51 x 1.51 x 1.45 mm^3 cut from C1 and C2, respectively. Fig.3-22(A) shows the normalized magnetic moment-temperature curves. The measurements were made while applying a 2 mT external magnetic field. Both samples show a sharp transition width at $T_{c,\,onset}$ = 39.25 K for C1 and $T_{c,\,onset}$ = 37.5 K for C2. The decrease of the $T_{c,onset}$ of the C2 sample could be related to: i) the partial substitution of boron by carbon, which changes the energy gap of the σ band [114,115]; ii) the carbon accumulation in the grain boundaries and the high microstrain that would decrease the critical temperature of C2. Fig.3-22(B) shows the magnetic field dependence of the critical current density J_c at 20 K for the two samples. In self-field, J_c is equal to 4.99 10^5 and 3.13 10^5A/cm^2 for C1 and C2, respectively. The decreasing critical current density from C1 to C2 is linked to the decreasing density of the samples and to the high amount of secondary phases. From 2 T, the higher J_c

values for sample C2 than for C1 are recorded. They reach 5.6 10^3A/cm^2 at 4T, which is the best result presented in this chapter. Compared with the results obtained by Dr. Arvapalli S. S. et al. [62] with the same mixture, the slightly reduced J_c observed in self-field can be explained by the high quantity of contaminants MgO and MgB_4 present in C2. The optimization of the sintering process to avoid the appearance of the MgB_4 phase is discussed in the next chapter.

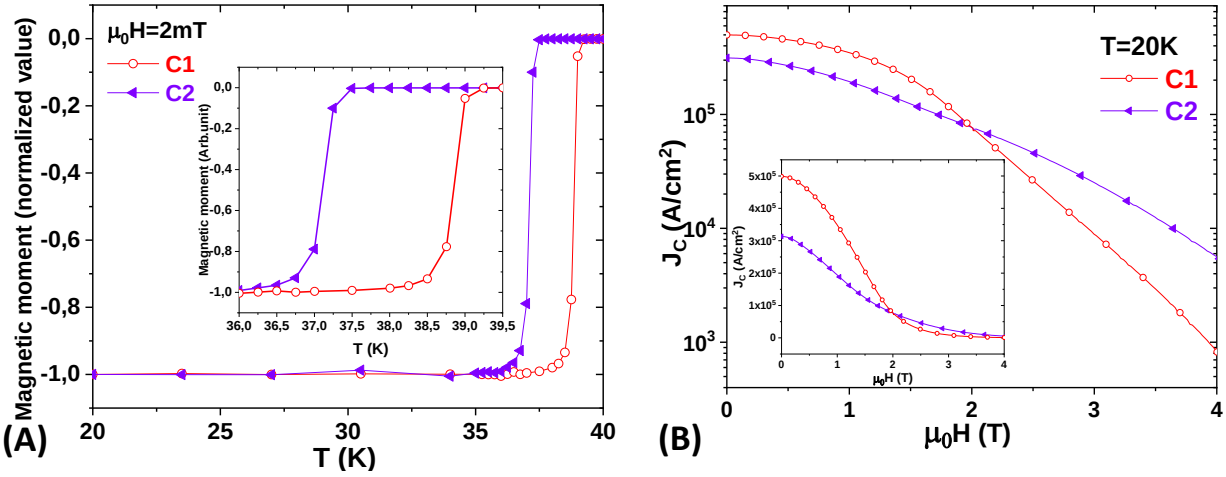

Fig.3-22: (A) Normalized magnetic moment as a function of the temperature. The inset shows the magnified onset of superconducting temperature. (B) Magnetic field dependence of the critical current density J_c at 20 K. The inset shows the same curves on a linear scale.

3.4 Pinning behavior investigation

In this section we discuss the flux pinning mechanisms of the investigated samples. For this purpose, we calculate their pinning force. Fig.3-23(A) shows the magnetic field dependence of the volume-pinning force density at 20 K calculated as $F_p = J_c * \mu_0 H$ for the seven investigated bulks. The maximum pinning force $F_{p,max}$ of C1 sample, 3.55 GN/m^3 at 1.14 T, is twice as large as that of B3 (1.48 GN/m^3 at 0.85 T). C2 shows the most significant pinning forces above 2 T. In order to estimate the dominant pinning centers, we have firstly used the scaling functions proposed by Dew-Hughes [32]. As mentioned in chapter 1, the normalized flux pinning force density, f_p $(F_p/F_{p,max})$, can be calculated with the following formula [Eq.3.2],

$$f_p = Ah^p(1-h)^q \quad \text{[Eq.3.2]}$$

where A is a parameter related to the pinning strength, p and q are related to the type of pinning centers and h is the reduced magnetic field (H/H_{c2}). However, we have carried out this work with the method the most used in the literature, which consists in considering that $h = H/H_{irr}$, where H_{irr} is often taken as the magnetic field for which J_c is equal to 100 A/cm^2 [116–118]. The peak value of h and the quantities p and q calculated using the Dew-Hughes model are shown in table 3-4. Compared to table 1-1, the h_{peak} of all the samples is around 0.2, which suggests that the dominant pinning centers are non-superconducting surface pins (NSP) corresponding probably to grain boundaries). However, the exponents p and q are always far

from the theoretical values (p_{theo}=0.5 and q_{theo}=2). Similar discrepancies have been mentioned by other authors on highly dense SPS bulks [117–120]. As a consequence, they have used another extended proposed by Eisterer [121]. This expression takes into account the anisotropy and the percolation threshold of the samples to evaluate their pinning behavior. The quantity h in the Dew-Hughes model is replaced by $h_n = H/H_n$, where H_n is the field above the peak field for which F_p drops to 50% of its maximum. For MgB_2, typical $h_{n,\,peak}$ values are 0.34 for grain boundaries pinning and 0.47 for normal point pinning (NPP). However, except for the less dense samples (B3 and C2) $h_{n,\,peak}$ is too large for both the grain boundaries pinning and the NPP mechanisms. The high density of the samples can't explain these results because the pinning behavior of highly dense samples prepared by hot pressing can be described with this model [35]. High $h_{n,\,peak}$ values similar to those presented here have been obtained with some MgB_2 bulks fabricated by SPS [35,117], while other samples have shown a good agreement with the Eisterer model [119,122]. The authors suggest that the results are also related to the working temperature [117], the texture of the samples and other parameters [122]. Concerning our results, we have observed an effect linked to the form and the anisotopy of some samples, which will be discussed later. Some authors [45,123–125] have used another extended scaling model proposed by Higuchi [124]. The main advantage of this model is that it avoids errors in the estimation of H_{irr}, since f_p is scaled with $h' = H/H_{max}$ where H_{max} is the field at which F_p reaches its maximum. The different pinning mechanisms correspond to the following equations:

$$f_p(h') = 3h'^2\left(1 - \frac{2h'}{3}\right) \quad \text{for superconducting point pinning (SPP)} \quad \text{[Eq.3.3]}$$

$$f_p(h') = \frac{9}{4}h'\left(1 - \frac{h'}{3}\right)^2 \quad \text{for non-superconducting point pinning (NPP)} \quad \text{[Eq.3.4]}$$

$$f_p(h') = \frac{25}{16}\sqrt{h'}\left(1 - \frac{h'}{5}\right)^2 \quad \text{for non-superconducting surface pinning (NSP)} \quad \text{[Eq.3.5]}$$

Fig.3-23(D) shows the results for all the bulks. Obviously, below H_{max}, the dominant pinning centers for all samples seem to be normal point pins. However, their pinning behaivoir mignt be changed from the Higuchi model in the high fields.

As a conclusion for this section, the dominant pinning centers in B3 and C2 are normal pins at low field, which can be related to their weak density and numerous tiny MgO precipitates in the MgB_2 grains. However, the dominant pinning mechanisms might change and result in both normal point pinning and grain boundary pinning at high field. The other samples show also point pinning at low field. Other aspects will be considered in the next chapter to further refine the pinning mechanisms of the samples and to correlate them to the scaling models.

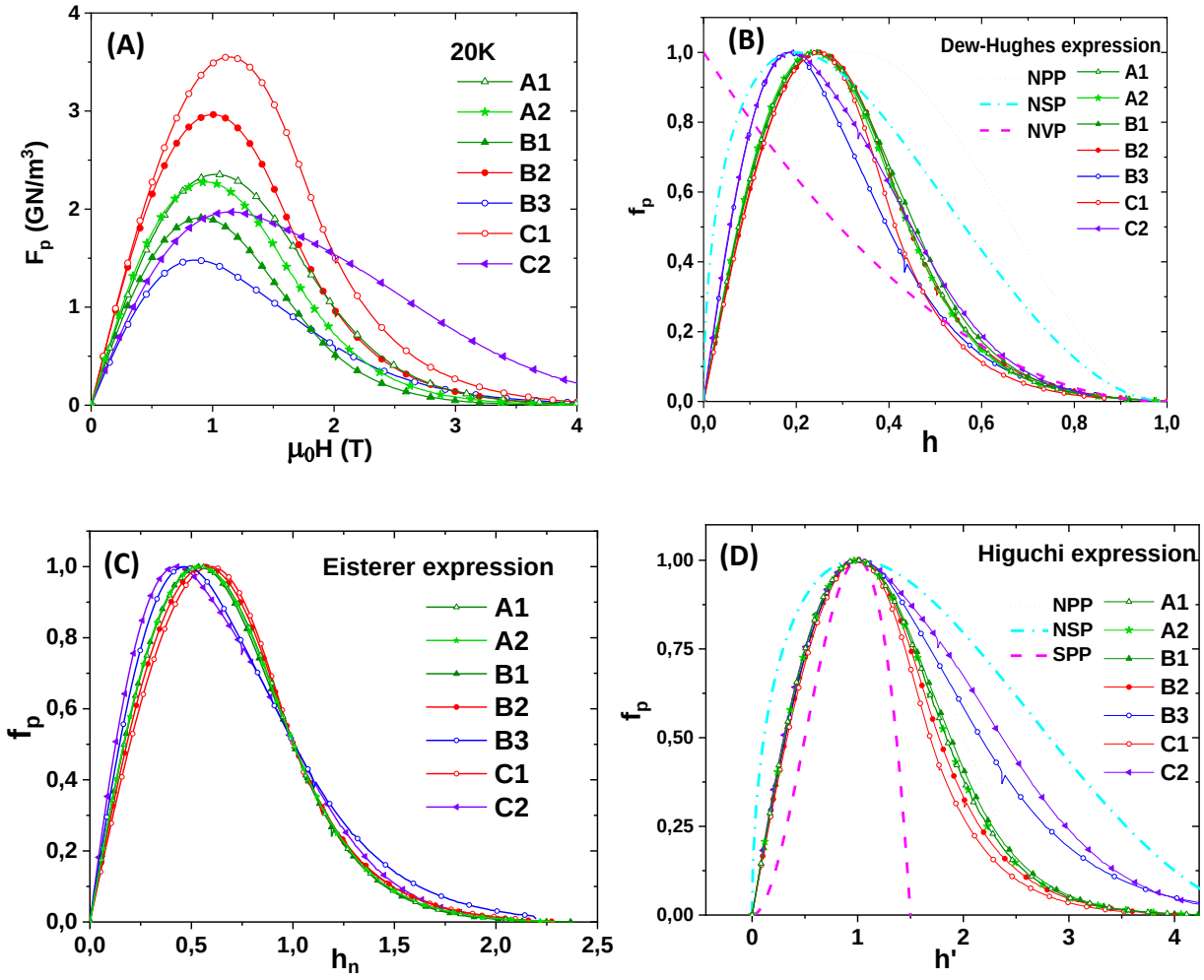

Fig.3-23: (A) the magnetic field dependence of the volume-pinning force density F_p. (B) scaling behavior of normalized pinning force density f_p using Dew-Hughes model. The orange dot-line represents the non-superconducting point pinning NPP; the cyan dash-dot-line, non-superconducting surface pinning NSP and the magenta dash-line, non-superconducting volume pinning NVP. (C) scaling behavior of f_p using Eisterer model. (D) scaling behavior of f_p using Higuchi model. The magenta dash-line represents the superconducting point pinning SPP.

Table 3-5 h_{peak}, p, q and $h_{n,peak}$ estimated of each bulk

Sample	A1	A2	B1	B2	B3	C1	C2
h_{peak}	0.24	0.24	0.24	0.25	0.18	0.25	0.19
p	1.4	1.4	1.43	1.54	1.2	1.7	1.1
q	4.9	4.9	4.72	5.1	5.4	5.9	4.2
$h_{n,peak}$	0.54	0.55	0.54	0.57	0.46	0.59	0.43

3.5 Conclusion

We have reported in table 3-6 the J_c obtained by the investigated bulk correlated to their density and crystallite size. Small grains, porosities, impurities as well as large quantities of grain boundaries could enhance flux pinning when a field is applied (see B3, C1 and C2). However, a high amount of secondary phases and a low density are harmful to J_c at low magnetic field and a high packing factor is required for the application. As a consequence, in the next chapter, a detailed study of the process conditions will be carried out with high-quality powders to improve the performances according to i) the densification of the samples and ii) the control the grain growth.

Table 3-6 Density, crystallite size estimated by XRD and J_c measured at 20 K for 0, 2 and 4 T

Precursors	Sample	Density	crystallite size (nm)	J_{c_0T} (A/cm^2)	J_{c_2T} (A/cm^2)	J_{c_4T} (A/cm^2)
Ex-situ lot1	A1	98%	93	$3.91\ 10^5$	$5.04\ 10^4$	298
Ex-situ lot2	A2	98%	80	$4.13\ 10^5$	$3.63\ 10^4$	95
Ex-situ lot1	B1	99%	160	$3.62\ 10^5$	$2.63\ 10^4$	22
In-situ Mg+2B	B2	96%	146	$4.92\ 10^5$	$4.93\ 10^4$	136
In-situ Mg+MgB_4	B3	92%	127	$2.95\ 10^5$	$3.07\ 10^4$	603
In-situ Mg+2B	C1	95%	135	$4.99\ 10^5$	$7.67\ 10^4$	822
In-situ Mg+2B/C	C2	83%	73	$3.13\ 10^5$	$7.71\ 10^4$	5658

Chapter 4 Optimization of sintering conditions

In chapter 3, we have studied the effect of different precursors on the superconductivity of MgB_2 bulks. Dense samples have exhibited a significant J_c in self-field, the best results being obtained with the in-situ Mg+2B samples. While the ex-situ bulks were the densest samples, their grain connectivity was weak because of the large MgO precipitates located at the grain boundaries. The samples prepared with the $Mg+MgB_4$ and Mg+2B/C powders have needed more energy to densify. Nevertheless, they have shown a significant J_c at high field, especially sample C2 which was fabricated with carbon-coated boron powder and had a large quantity of pinning centers.

The principal objective of this chapter is to fabricate dense samples with a controlled microstructure.

4.1 Characterizations of samples prepared at different pressures using graphite molds.

4.1.1 Sample preparation

In this section, we report the fabrication and we study the properties of samples fabricated with two precursors: lot1 ex-situ powder and Mg+2B in-situ mixture in order to investigate the effect of the sintering pressure on the performances of the samples. The results reported in chapter 3 show that a good crystallinity requires a high sintering temperature. Hence, two batches of samples fabricated with the two selected precursors were prepared in graphite molds applying various pressures at the different steps of the process, according to the following protocol:

i) 500 °C + 16/60/85/100 MPa / 15 minutes (compaction + pre-synthesis)

ii) 650 °C + 30/80/105/120 MPa / 20 minutes (synthesis)

iii) 950 °C + 50/100/125/140 MPa / 30 minutes (sintering)

iv) 1000 °C + 50/100/125/140 MPa / 5 minutes (densification)

The highest pressure that can be applied to a graphite die is 140 Mpa. Four different sintering pressures: 50, 100, 125 and 140 MPa have been applied to fabricate the bulks. As expected, the density of the bulks increases with the applied pressure (Fig.4-1). Both ex-situ and in-situ samples attain a packing ratio around 98% at 140 MPa. We mention also that the in-situ samples exhibit a much higher density than the ex-situ ones at low pressure (50 MPa). This characteristic can be attributed to the Mg diffusion occurring during reactive sintering, which helps to improve the grain connectivity and consequently the sample density.

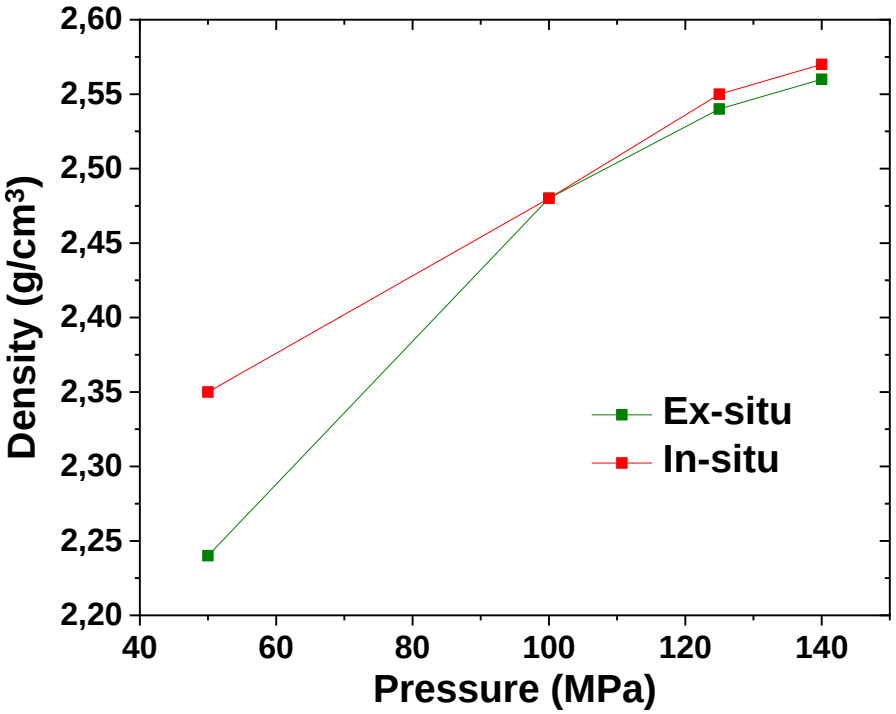

Fig.4-1 Density of sintered bulks as a function of sintering pressure

4.1.2 Structural and microstructure characterizations

The results of the XRD refinement of each sample are reported in table 4-1. Compared to the theoretical values a = 3.086 Å and c = 3.524 Å [103], the a-parameter of the ex-situ samples is reduced while that of the in-situ samples doesn't significantly change when the pressure increases. To the contrary the c-parameter of both the in-situ and the ex-situ samples is an increasing function of the pressure. From the estimated composition of the samples, the oxygen content of ex-situ samples is twice that of the in-situ ones. Moreover, the quantities of MgB_4 impurities of all the samples are similar, except for the in-situ samples sintered at 100 MPa and 140 MPa. This could be due to the inhomogeneous distribution of the secondary phases, as suggested by the SEM microstructure analysis (see below). Finally, compared to the ex-situ bulks, the in-situ samples exhibit larger MgB_2 crystallites. As a conclusion, the sintering pressure has no effect on the content in secondary phases and little or no effect on the size of the crystallites of the MgB_2 phase.

Table 4-1 Lattice parameters, *c/a* ratio, amount of each phase and crystallite size of the fabricated bulks

Sample	*a* (Å)	*c* (Å)	*c/a*	MgB_2 (wt%)	MgB_4 (wt%)	MgO (wt%)	crystallite size (nm)
Ex-situ 50MPa	3.0854	3.5257	1.143	79.88	11.63	8.49	114
Ex-situ 100MPa	3.0839	3.5269	1.1436	79.16	12.1	8.74	106
Ex-situ 125MPa	3.0838	3.5274	1.1438	79.69	11.57	8.74	105
Ex-situ 140MPa	3.084	3.5277	1.1439	79.32	12.08	8.6	94
In-situ 50MPa	3.0855	3.5263	1.1429	84.93	10.57	4.5	145
In-situ 100MPa	3.0863	3.5274	1.1429	89.17	6.66	4.16	134
In-situ 125MPa	3.8051	3.5281	1.1436	83.69	11.87	4.44	133
In-situ 140MPa	3.0854	3.5284	1.1436	90.29	5.72	3.99	137

The SEM micrographs of the ex-situ samples prepared at different pressure are shown in Fig.4-2. The distribution of the phases present in the samples was examined with back-scattered electrons (see Fig.4-2(A) and (B)) and the topographic view of the MgB_2 grains was obtained with secondary electrons (see Fig.4-2(C)-(F)). Fig.4-2(A) shows that the secondary phases (MgO and MgB_4) are unevenly distributed in the MgB_2 phase. Some layered structures can also be founded in the sample sintered at 140 MPa (Fig.4-2(B)). Figs.4-2(C)-(F), show that the MgB_2 grains exhibit a high packing ratio, while numerous and large MgO grains (as compared to those in the in-situ samples-see Figs.4-3) are located at their grain boundaries, except in the case of the sample sintered at 50 MPa. There is no significant variation in the MgB_2 grain size (ranging around 1000 nm), which is consistent with the XRD analysis.

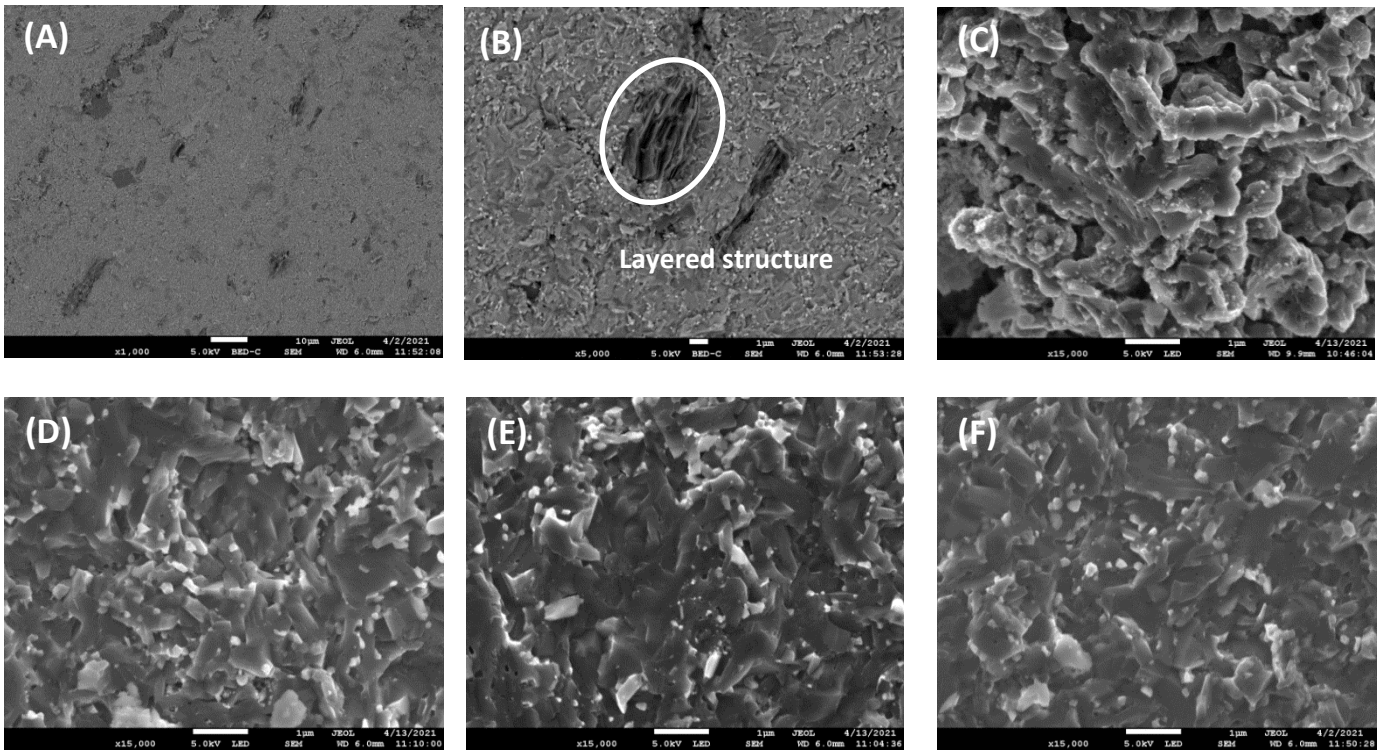

Fig.4-2: (A) SEM micrographs detected by back-scattered electrons of ex-situ sample sintered at 140 MPa and (B) the local magnification. (C)-(F) are the topographic view of MgB_2 grains detected by the secondary electrons in ex-situ samples sintered under 50-140 MPa, respectively

Fig.4-3 shows the microstructure of the in-situ samples. The images (A) and (B) show the chemical composition distribution in the bulk sintered at 140 MPa. Aggregations of ultra-tiny MgO particles can be seen as white spots and pores due to the evaporation of Mg during sintering are visible in dark grey regions. MgO particles with an almost uniform size are present inside the MgB_2 grains or at their grain boundaries. Compared to the ex-situ samples, the MgO precipitates are smaller, which increase the intergrain contact area. Figs.4-3 (C)-(F) show the MgB_2 grains topography of the bulks sintered at different pressures, the size of which is similar to that of the ex-situ bulks. The main difference between the ex-situ and in-situ samples is the distributions of the MgO impurities and their size which are very different. This dramatically affects the grain connectivity as well as the critical current density.

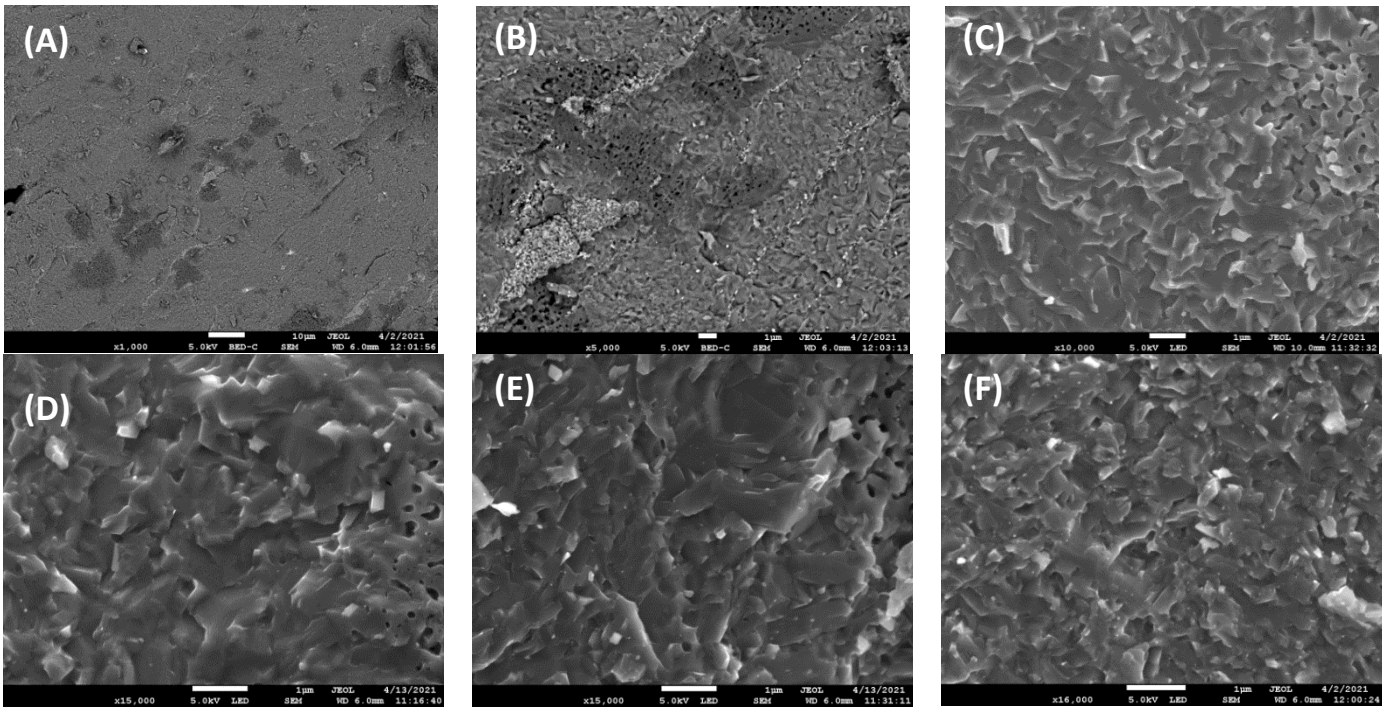

Fig.4-3: (A) SEM micrographs detected by back-scattered electrons of in-situ sample sintered at 140 MPa and (B) the local magnification. (C)-(F) are the topographic view of MgB_2 grains detected by the secondary electrons in in-situ samples sintered under 50-140 MPa, respectively

4.1.3 Superconducting properties

Resistivity measurements were carried out from 0 to 9 T on long samples with dimensions approximately equal to 1.5 x 1.5 x 10 mm^3 cut from the fabricated bulks to determine their critical temperature, irreversible field, H_{irr}, and second critical field, H_{c2}, as well their connectivity. The results reported in Tables 4-1 and 4-2 confirm that the in-situ samples have a higher purity and a stronger connectivity than the ex-situ ones, if they are sintered at a pressure below 125 MPa. The irreversible critical field and upper critical field of the samples have been determined with the technique based on the 10% and 90% normal-state resistivity ρ_{40K} at 40 K [88,94]. Slight differences H_{irr} and H_{c2} can be observed between the ex-situ and the in-situ bulks. In addition, the sintering pressure and the packing ratio don't significantly affect the resistivity of the samples.

Table 4-2 Offset critical temperature, measured resistivity values, residual resistivity ratios (*RRR*), connectivity (*K*), irreversibility magnetic field, H_{irr} and the upper critical magnetic field, H_{c2}

Sample	T_c (K)	ρ_{300K} (μΩcm)	ρ_{40K} (μΩcm)	*RRR*	*K*	H_{irr} at 20 K (T)	H_{c2} at 20 K (T)
Ex-situ 50MPa	37.6	54.7	16.7	3.27	0.166	6.2	8.6
Ex-situ 100MPa	37.6	45.9	13.4	3.42	0.194	6.3	8.6
Ex-situ 125MPa	37.6	27.3	7.9	3.46	0.326	6.4	8.7
Ex-situ 140MPa	37.6	34.5	10.1	3.42	0.259	6.3	8.7
In-situ 50MPa	38.6	18.4	3	6.15	0.41	6.2	8.4
In-situ 100MPa	38.6	16.5	2.9	5.65	0.466	6.6	8.2
In-situ 125MPa	38.6	21.8	4	5.42	0.356	6.7	8.3
In-situ 140MPa	38.6	25.5	4	6.41	0.248	6.7	8.4

Small specimens with dimensions of approximately 1.5 x 1.5 x 1.8 mm^3 were cut from the sintered bulks in order to verify their critical temperature, T_c and to record their magnetization hysteresis loops at 20 K in the 0-4 T range with the SQUID magnetometer. The magnetic moments measured as a function of the temperature are shown in Fig.4-4. The $T_{c,\ onset}$ of the ex-situ samples is 38.25 K and is lower than that of the in-situ ones which is equal to 39.25 K. The results suggest that all the samples have a good crystallinity and show that the SPS pressure has no impact on their critical temperature.

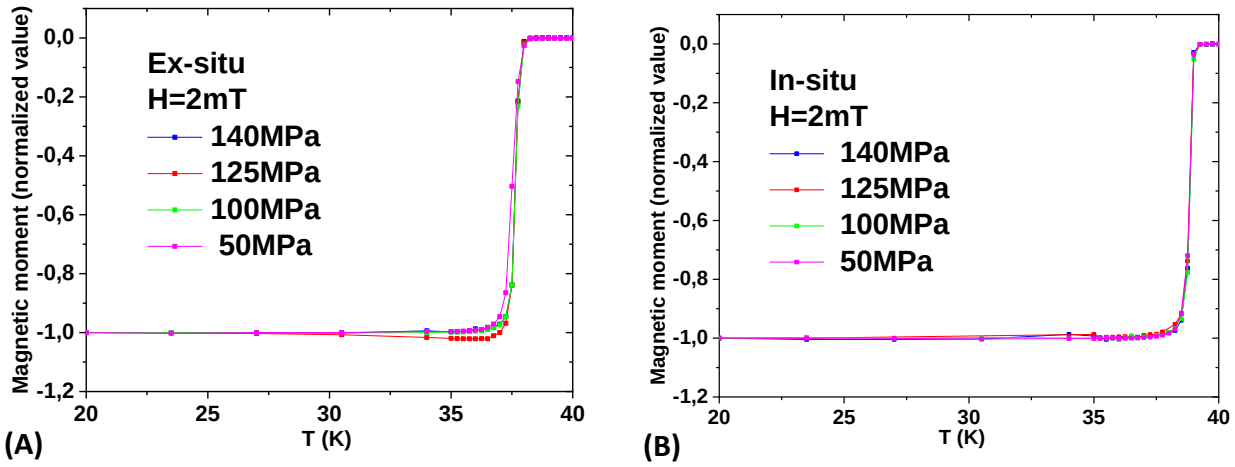

Fig.4-4: Normalized magnetic moment as a function of the temperature for (A) ex-situ and (B) in-situ bulks

The critical current densities of the bulks as a function of the applied field was estimated from *M-H* loops recorded at 20 K using the extended Bean critical state model for rectangular samples [93]. They are reported in Fig.4-5. The in-situ samples exhibit a higher J_c than the ex-situ ones both at low and high fields, confirming the results reported in chapter 3. There is no significant pressure effect on the very dense bulks (d_{sample}>95%) sintered between 100 and 140 MPa. The densities of the samples sintered at 50 MPa are less than 90%, which is the reason why their critical current density is low. From these results, we can conclude that the increase of the SPS sintering pressure results in an increase of the packing ratio of the samples as well as an increase of the critical current density if the samples density is below 95%, while J_c is constant for samples with a density greater than 95%. Consequently, reducing the sintering temperature to limit the grain growth while increasing the applied pressure to keep a high packing ratio can be another solution for preparing highly-dense samples and enhancing their superconducting properties. This is investigated in the next section.

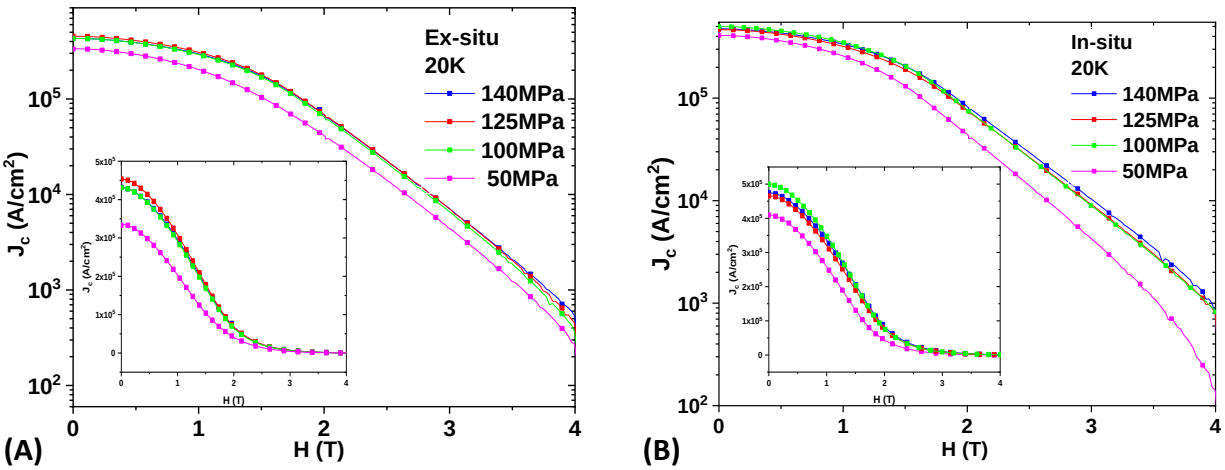

Fig.4-5: Magnetic field dependence of the critical current density J_c at 20 K for (A) ex-situ and (B) in-situ bulks. The inset shows the same curves on a linear scale.

4.2 Properties of the samples prepared at high pressure and low temperature using specific tungsten carbide mold

The results obtained by varying the sintering pressure have revealed that the pressure could enhance the bulks packing ratio but did not significantly affect the content of secondary phases and the crystallite size. The critical current density J_c decreases only when the density of samples is below 90%. From another point of view, in order to increase the critical current density, it is possible to enhance the grain connectivity and control the growth of grains by increasing the pressure and decreasing the temperature applied during Spark Plasma Sintering. Hence, in this part, we have used specific carbide tungsten (WC) dies, which allow to apply sintering pressures up to 1 GPa.

4.2.1 Sample preparation

The starting powders used to prepare the samples were the mixtures Mg+2B and Mg+2B/C. A mass of 1.5 g of powder was weighted and loaded into 20 mm diameter tungsten carbide

(WC) molds. According to the technique used for the graphite molds, graphite foils were wrapped alongside the inner wall of the WC mold and inserted between the powder and the two punches to facilitate demolding. The samples were sintered according to the following protocol:

i) 500 °C + 260 MPa / 15 minutes (Powder compaction)

ii) 650 °C + 280 MPa / 20 minutes (Synthesis)

iii) 650/700/750/800 °C + 300 MPa / 30 minutes (Sintering+densification)

As mentioned above, the samples were sintered at temperatures ranging between 650 and 800°C. The sample sintered at 750°C using the Mg+2B mixture was named W1 and the one using Mg+2B/C, W2. As explained in chapter 3, the introduction of different steps in the process aimed at avoiding magnesium evaporation. The heating rate was 100°C/min and the cooling time was about 20 minutes. The total processing duration was approximately 100 minutes. The temperature was monitored with a thermocouple instead of a pyrometer when sintering was carried out in a graphite mold. Fig.4-6(A) shows the displacement of the piston for W1 and W2 during the different steps of the process as a function of time and of the temperature. We emphazise that the mixture containing carbon-coated boron (W2) has reacted violently during the first step and has slowly shrunk during the subsequent ones. The powder containing nano amorphous boron (W1) was compressed at each step and tended toward stability at the end. After processing, the density of W1 and W2 was 2.46 g/cm^3 and 2.37 g/cm^3, which corresponds to 94% and 90% of the theoretical value, respectively. Compared to samples C1 and C2 which were sintered in graphite molds at 950°C and 100 MPa, the density has decreased 1% for sample W1 and increased 7% for sample W2. The density of the other bulks prepared using the Mg+2B mixture is shown in Fig.4-6(B) as a function of the sintering temperature. The density raises with increasing sintering temperature to reach 95% at 800°C. Consistently with the density of W2 shown in Fig.4-6(B), the packing ratio of the bulks fabricated with the Mg+2B/C mixture was lower than the packing ratio of those fabricated at the same temperature with the Mg+2B mixture.

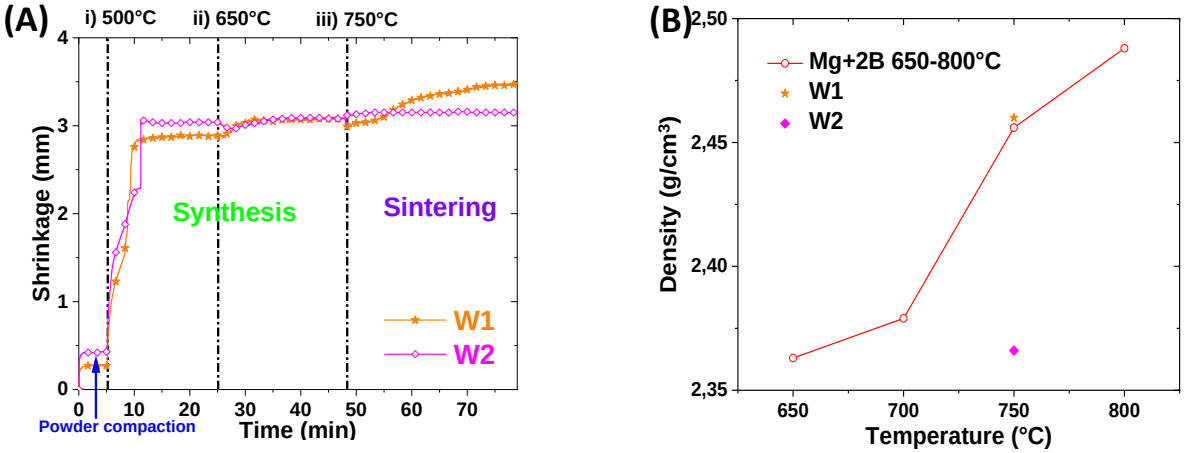

Fig.4-6: (A) Displacement of piston vs. sintering time curves for W1 and W2 bulks. (B) The density of sintered bulks as a function of sintering temperature

4.2.2 Structure and microstructure analyses

Table 4-3 summarizes the XRD refinement results of the four samples prepared with the Mg+2B mixture at the different sintering temperatures. Comparing the lattice parameters to those reported by Buzea C. [103] (a = 3.086 Å and c = 3.524 Å), the results in table 4-3 confirm those obtained with the samples sintered in graphite molds: the c-parameter expand when increasing the SPS sintering pressure. Otherwise, the low-temperature process effectively inhibits the emergence of MgB_4, while the MgO content is around 4-5 wt%, which is comparable to the bulks sintered at a higher temperature in graphite molds The estimated crystallite size ranging between 58 nm and 88 nm is much smaller than that of the samples fabricated with the graphite molds (133-145 nm), indicating that SPS allows the preparation of highly-dense samples, while controlling the grain growth.

Table 4-3 Lattice parameters, *c/a* ratio, amount of each phase and crystallite size of the fabricated bulks

Reference	*a* (Å)	*c* (Å)	*c/a*	MgB_2 (wt%)	MgO (wt%)	crystallite size (nm)
Mg+2B 650°C	3.0876	3.5269	1.1423	96.08	3.92	58
Mg+2B 700°C	3.0871	3.5286	1.143	94.96	5.04	61
Mg+2B 750°C	3.0862	3.5288	1.1434	95.66	4.34	88
Mg+2B 800°C	3.0864	3.5272	1.1428	95.47	4.53	84

The XRD of samples W1 and W2 reported in Fig.4-7 shows that the major peaks are due to the MgB_2 phase and that traces of MgO are present. Small peaks of carbon due to the carbon foil [126] are also observed in W1. Table 4-4 shows a comparison of the results obtained by refinement of the XRD of W1 and W2 to the same data obtained for C1 and C2 which were sintered in graphite molds using the same precursors.

According to the expression proposed by M. Avdeev et al. [127], the carbon substitution level, x in $Mg(B_{1-x}C_x)_2$, can be estimated with the expression:

$$x = 7.5 \cdot \Delta(c/a) \quad \text{[Eq.4.1]}$$

where Δ(c/a) is the difference between the *c/a* ratio of the $Mg(B_{1-x}C_x)_2$ compound and that of the undoped sample. The quatity $2x$ is equal to 0.027 and 0.0315 for the bulk prepared with the Mg+2B/C powder and sintered in the WC mold (W2) and in the graphite mold (C2), respectively. The obtained results are comparable to those calculated by Dr. Arvapalli S.S. [62], using the same precursor ($2x$=0.036). A high amount of MgO impurities is observed in the bulk sintered with the Mg+2B/C mixture (W2 and C2). Compared to C1 and C2, the MgO content of W1 and W2 is slightly higher, and there is no MgB_4 phase as a result of the low sintering temperature of these samples. The MgB_2 crystallite size of W1 and W2 as

estimated from refinement was 59 and 44 nm, demonstrating a significant microstructure control.

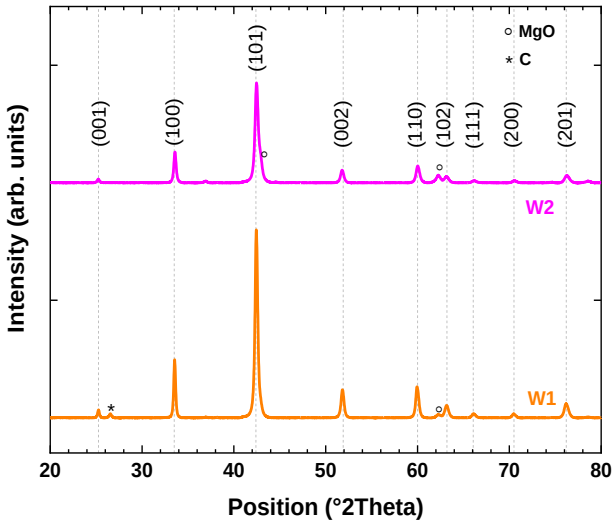

Fig.4-7: X-Ray Diagram of samples W1 and W2.

Table 4-4 Lattice parameters, *c/a* ratio, amount of each phase and crystallite size of the fabricated bulks

Reference	*a* (Å)	*c* (Å)	*c/a*	MgB_2 (wt%)	MgO (wt%)	MgB_4 (wt%)	crystallite size (nm)
W1	3.0854	3.5286	1.1436	95.39	4.61	-	59
W2	3.0827	3.531	1.1454	82.84	17.16	-	44
C1	3.0863	3.5273	1.1429	89.17	4.16	6.66	134
C2	3.0822	3.5291	1.145	66.93	15.99	17.08	73

The microstructures of the fractured surface of W1 and W2 are shown in Fig.4-8. The distribution of the MgO phase in the two bulks is similar, which means that nano MgO particles aggregated as plates or strips form and are scattered in the MgB2 matrix. We underscore the presence of compact MgB_2 nano-grains and the high number of grain boundaries seen in Fig.4-8(C) and (D). Highly dense bulks with numerous pinning centers should enhance the critical current density in both low and high magnetic fields, which will be further verified by the determination of J_c.

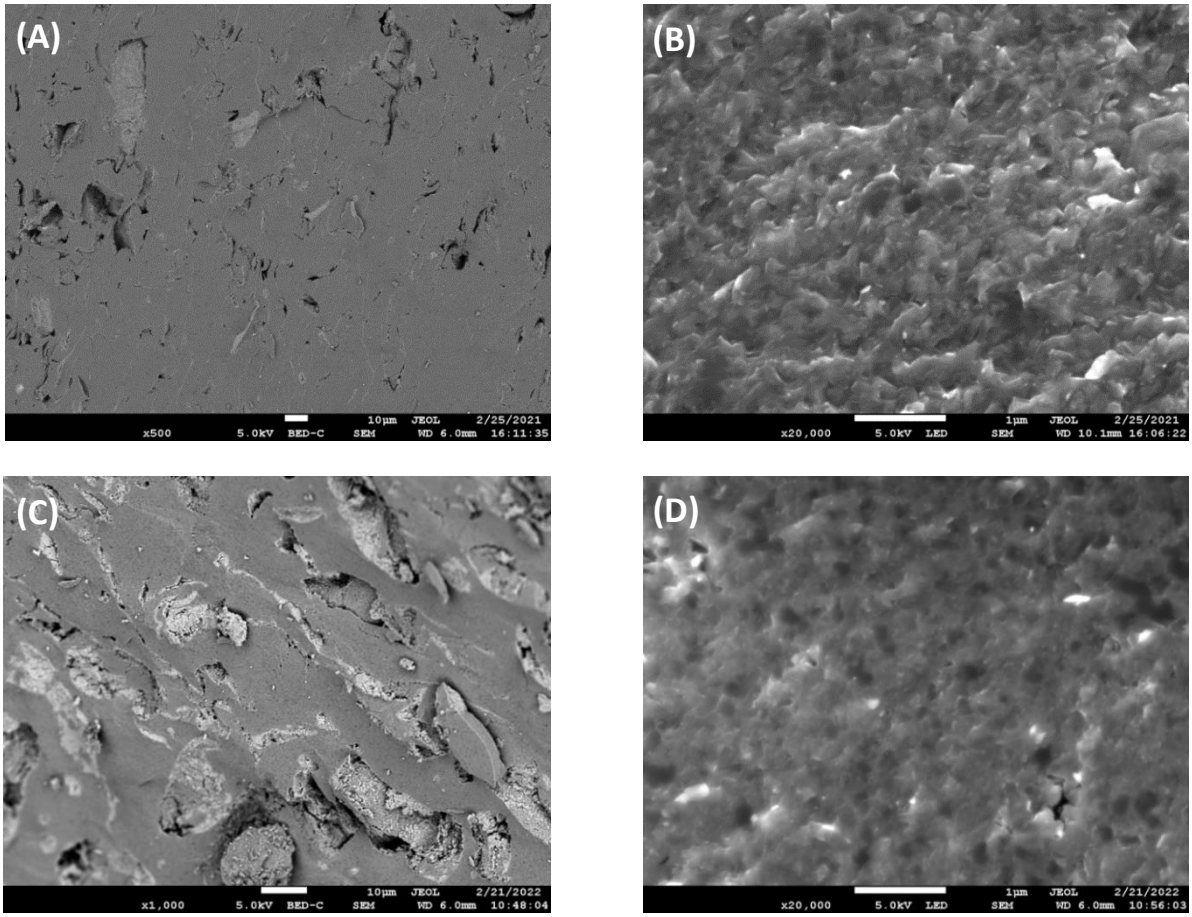

Fig.4-8: Chemical microstructure of (A) W1 and (C) W2 samples; High magnification SEM image of nano MgB_2 grains in (B) W1 and (D) W2 bulks.

An EDS analysis has been carried out on W1 sample (Figs.4-9). Along with the MgO regions, the boron enriched areas are visible in dark grey zones, which might have a flux pinning enhancing effect. These boron-rich areas are supposed to consist in amorphous boron unreacted at the low sintering temperatureapplied.

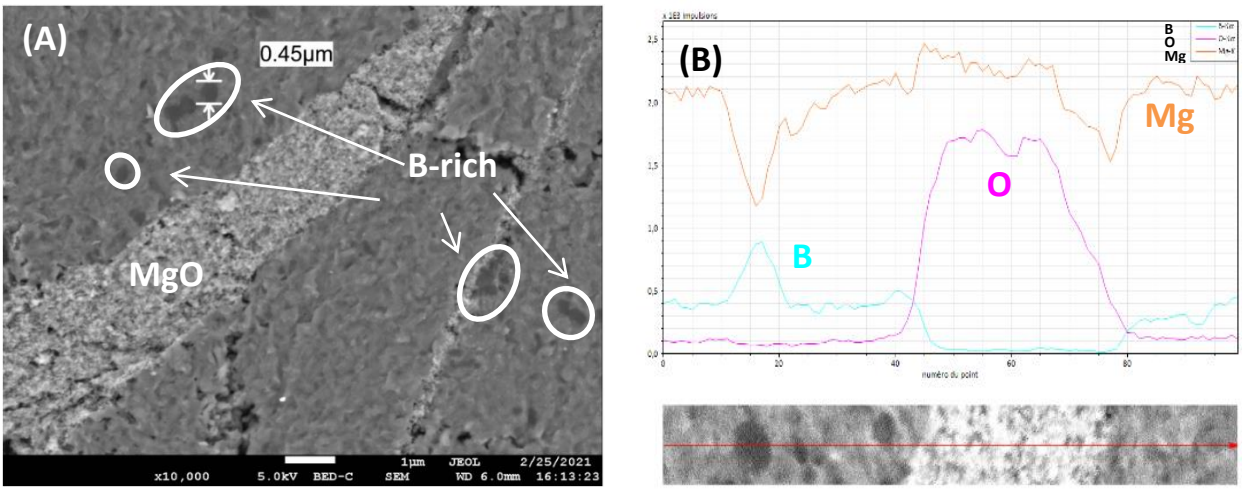

Fig.4-9: (A) SEM micrograph of sample W1 showing the unreacted boron and MgO regions in the MgB_2 matrix. (B) EDS red line region scan curves of B (cyan line), O (magenta line) and Mg (orange line).

4.2.3 Superconducting properties

The in-field resistivity of W1 and W2 was measured by the DC 4-probes method up to 14 T. Fig.4-10(A) shows firstly resistivity ρ as a function of the temperature in self-field. The superconducting transition region is zoomed in the inset. The normal-state resistivity of W2 is higher than that of W1. This is probably due to the high quantity of oxide phase and low packing ratio of W2. The residual resistivity ratio (*RRR*) and the electrical connectivity *K* of the samples are reported in table 4-5. The results suggest that W2 has a lower purity and a weaker intergrain coupling than W1, resulting in a reduction of the critical temperature. Furthermore, compared to the in-situ Mg+2B samples sintered in graphite dies, W1 shows a high normal-state resistivity, which might be linked either to the presence of the amorphous boron phase or to a high quantity of grain boundaries. The upper critical magnetic field, H_{c2} and the irreversibility magnetic field, H_{irr} were determined with the technique based on the 10% and 90% normal-state resistivity at 40K [88,94]. From measurements of the in-field resistivity carried out between 6 K and 40 K , their temperature dependence could be determined and is plotted in Fig.4-10(B). The H_{c2} and H_{irr} at 20 K are 9.7 T and 7.9 T, respectively, for W1 and 11.9 T and 9.7 T for W2. These fields are higher than those measured in prior research and are comparable to some values reported for other MgB_2 bulks [124,128]. Although the bulks sintered in WC molds show a lower critical temperature and a higher electrical resistivity than those sintered in graphite dies, their H_{irr} and H_{c2} were significantly enhanced. This is also the case of their critical current density, J_c, as shown by the following results.

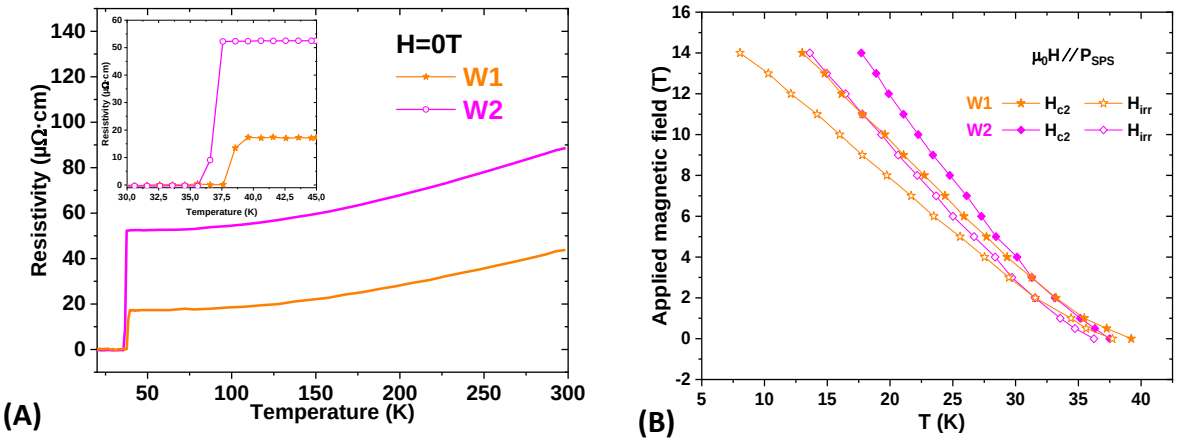

Fig.4-10: (A) Temperature dependence of the resistivity at 0 T with a 5 mA direct current. The inset shows the magnified superconducting transition region. (B) Temperature dependence of H_{c2} and H_{irr} for W1 and W2 samples.

Table 4-5 Measured resistivity values, residual resistivity ratios (*RRR*), connectivity (*K*), irreversibility magnetic field, H_{irr} and the upper critical magnetic field, H_{c2}

Sample	T_c (K)	ρ_{300K} (μΩcm)	ρ_{40K} (μΩcm)	*RRR*	*K*	H_{irr} at 20 K (T)	H_{c2} at 20 K (T)
W1	37.6	43.8	17.09	2.56	0.237	7.9	9.7
W2	35.6	88.6	52.53	1.69	0.175	9.5	11.9

Small specimens with dimensions around 1.5 x 1.5 x 1.8 mm^3 were cut from MgB_2 bulks made with the Mg+2B powder in WC molds and sintered at different temperatures in order to measure their T_c and J_c. The normalized magnetic moment of the samples as a function of the temperature is plotted in Fig.4-11(A). The transition temperature increases as the sintering temperature increases, indicating an improvement of the crystallinity. High J_c ranging from 6.10^5 to 7.10^5 A/cm^2 were were determined in self-field at 20 K (Fig.4-11(B)). Remarkably, under a 4 T applied field, the critical current density of the samples sintered between 650 and 750°C was above 10^4 A/cm^2. Compared to the bulks sintered in graphite molds, the bulks sintered in WC molds show a significant improvement of their critical current density at both low and high fields. This can be attributed to the strong densification of the nano grains and the suppression of the MgB_4 phase, suggesting that it is possible to enhance the grain connectivity by increasing the pressure and decreasing the temperature applied during Spark Plasma Sintering. Furthermore, as compared to the best J_c of no-doped in-situ sintered MgB_2 bulk reported by other authors and summarized in table 1-2, there is a significant improvement of the critical current density at both low and high field. The only exceptions are the samples prepared by high pressure processing (HP) by Prikhna et al. [66,76]. The reported high J_c values result from a smaller grain size and a higher density than for our samples. All these results confirm that it is possible to enhance the grain connectivity by increasing the pressure and decreasing the temperature applied during sintering. Comparing SPS and HP processing, we emphazise that the required sintering pressure and temperature are far greater for HP than for SPS. In addition, the SPS processing time is generally shorter than that required by the other techniques.

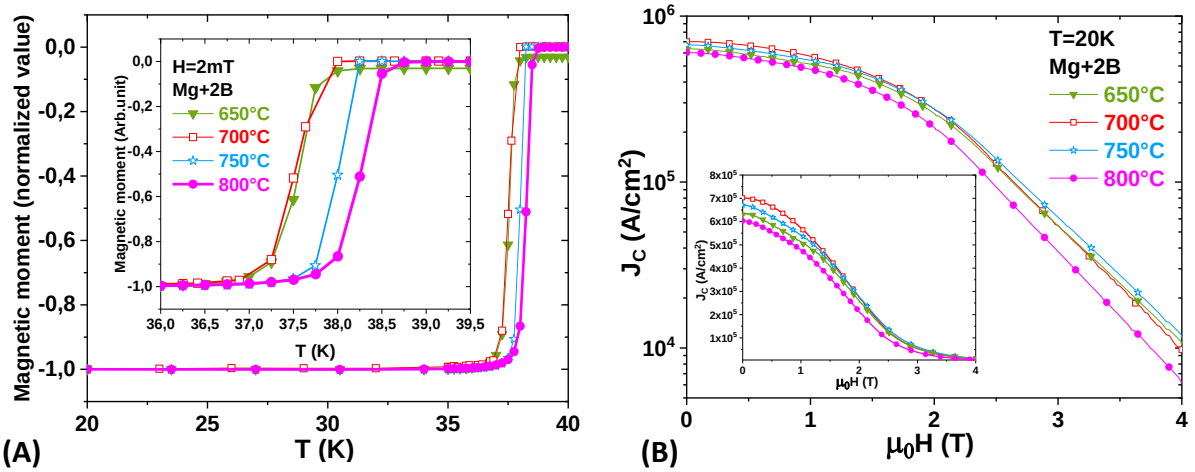

Fig.4-11: (A) Normalized magnetic moment vs. temperature for the samples processed at various temperatures. (B) Magnetic field dependence of the critical current density J_c at 20K for the samples processed at various temperatures. The inset shows the same curves on a linear scale.

The superconducting properties of samples W1 and W2, have been especially investigated. Small specimens with dimensions 1.51 x 1.54 x 1.62 and 1.52 x 1.54 x 1.89 mm^3 were cut from the bulks W1 and W2, respectively. In order to better compare the results to those of samples sintered in a graphite mold, the measurements carried out on bulks C1 and C2, which were sintered at 950°C and 100 MPa, have been reported in the same pictures. As shown in

Fig.4-12(A), all the samples exhibit a narrow transition width, while the onset and offset of the superconducting transition decrease with decreasing sintering temperature. Sample W2 which was sintered with the mixture Mg+2B/C has the lowest $T_{c,\,onset}$ which is equal to 36.75 K.

Contrary to the normal–state resistivity and critical temperature, extreme enhancement of J_c is observed with the samples sintered at low temperature and high pressure (Fig.4-12(B)), consistently with their improved H_{irr} and H_{c2}. We first compare the results of W1 and W2 samples, We remind that the grain connectivity or packing ratio influences J_c in self-field [108] while the grain boundaries dominate the pinning behavior at high magnetic field [129]. At 20 K, J_c=6.75 10^5 A/cm^2 and J_c=5.4 10^5 A/cm^2 for W1 and W2, respectively, were measured in self-field. The lower J_c value in W2 can be explained by its higher content in MgO and its lower density resulting in a weaker grain connectivity. The critical current density of W2 exceeds that of W1 bulk above 2.5 T and is equal to 10^4 A/cm^2 at 5 T, indicating that a larger number of pinning centers exist in W2. Furthermore, comparing W1 and W2 to C1 and C2, respectively, in self-field J_c increases by 30% for W1 and by 55% for W2. The significant enhancement of the J_c of W2 with respect to that of C2 can be related to the absence of MgB_4 and to its larger packing ratio. Remarkably, at 4 T, the J_c of W1 is 16 times that of C1 and the J_c of W2 is more than 5 times that of C2.

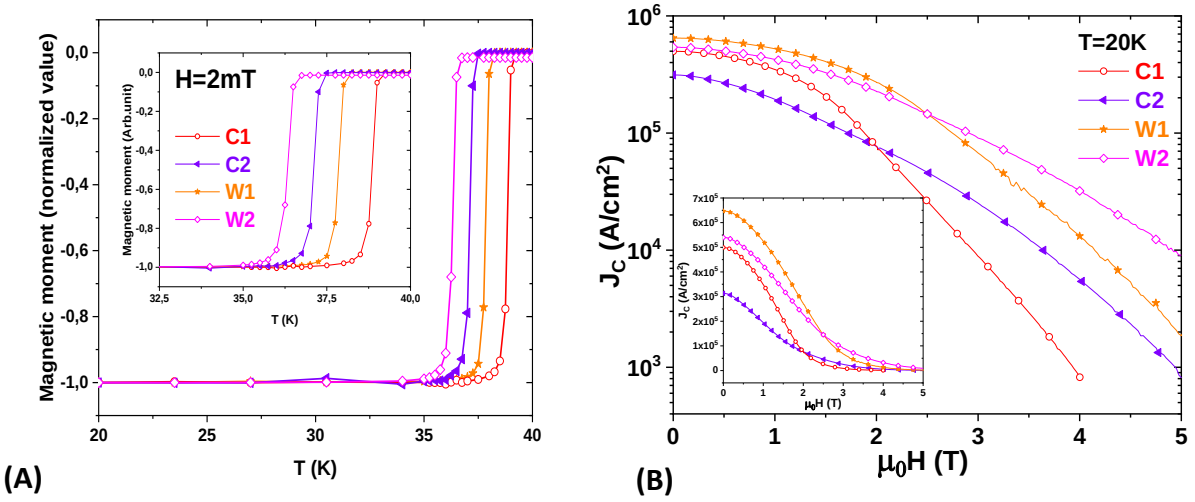

Fig.4-12: (A) Normalized magnetic moment of samples as a function of the temperature. (B) Magnetic field dependence of the critical current density J_c of samples at 20 K. The inset shows the same curves on a linear scale.

The pinning mechanism of the four bulks has been firstly investigated at 20 K using the models described in the previous sections. The magnetic field dependence of the volume-pinning forces F_p $(=J_c*\mu_0 H)$ is plotted in Fig.4-13(A). Sample W1 shows the highest maximum pinning force $F_{p,max}$=6.12 GN/m^{-3} at 1.56 T. This is 1.7 times larger than C1 ($F_{p,max}$=3.55 GN/m^{-3} at 1.16 T) and 1.2 times larger than W2 ($F_{p,max}$=4.93 GN/m^{-3} at 1.54 T). At high field, the samples prepared with the precursor containing carbon-coated boron exhibit a higher pinning force than those prepared with amorphous boron. Fig.4-13(B) and table 4-6 show the normalized flux pinning force densities of the samples and the best reproduction of

these quantities with the Dew-Hughes scaling functions. For the reasons exposed in the previous sections, it is difficult to use these results to deduce the pinning behavior of the samples. As done in chapter 3, two other approaches have been tested to further understand the pinning mechanism of the samples. In the Eisterer's model (Fig.4-13(C)) the normalized pinning force f_p is plotted as a function of $h_n = \frac{H}{H_n}$ where H_n is the field above the peak field for which F_p drops to 50% of its maximum. The results suggest that C1 and W1, which were prepared with the same precursor (Mg+2B), have the same dominant pinning mechanisms at 20 K. Pinning in these samples can't be due to non-superconducting surface pinning (NSP) or non-superconducting point pinning (NPP), because $h_{n,peak}$ is too high with respect to the expected values (see Table 4-6). The Higuchi method in which f_p is plotted as a function of $h' = \frac{H}{H_{max}}$ (see section 3.4) confirm that C1 and W1 have the same dominant pinning mechanism. Fig.4-13(D) suggests in addition that for all the samples and $H<H_{max}$ ($h'<1$), the main pinning mechanism is normal point pinning (NPP), but this conclusion is in contradiction to the results obtained with the Eisterer method.

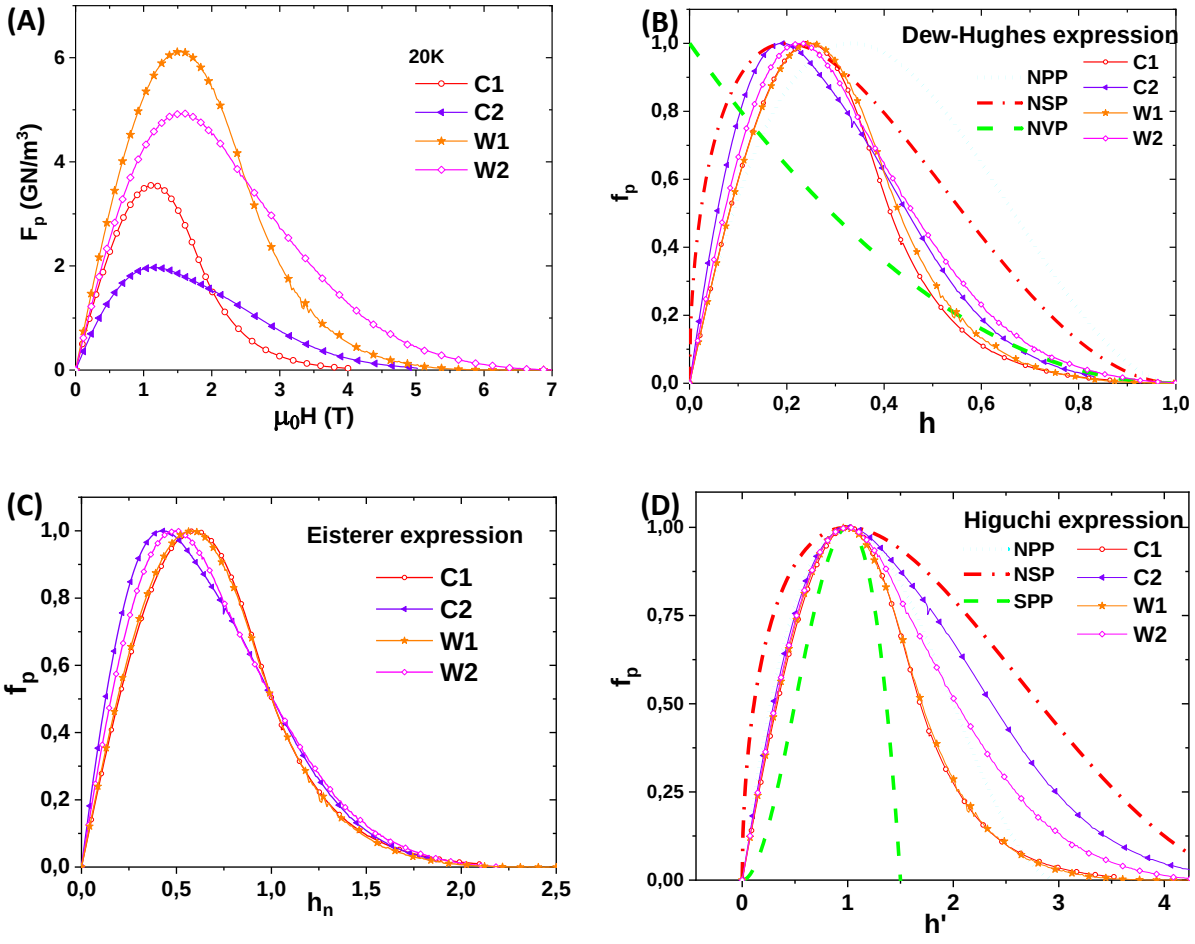

Fig.4-13: (A) the magnetic field dependence of the volume-pinning force density F_p. (B) scaling behavior of normalized pinning force density f_p using Dew-Hughes model. The cyan dot-line represents the non-superconducting point pinning NPP; the red dash-dot-line, non-superconducting surface pinning NSP and the green dash-line, non-superconducting volume pinning NVP. (C) scaling behavior of f_p using Eisterer model. (D) scaling behavior of f_p using Higuchi model. The green dash-line represents the superconducting point pinning

Table 4-6 h_{peak}, p, q and $h_{n,peak}$ estimated of each bulk

Sample	C1	C2	W1	W2	NSP	NPP
h_{peak}	0.25	0.19	0.25	0.23	0.2	0.33
p	1.7	1.1	1.6	1.2	1/2	1
q	5.9	4.2	5.4	4.3	2	2
$h_{n,peak}$	0.59	0.43	0.59	0.50	0.34	0.47

Fig.4-14 shows the dependence of the critical current density on the applied magnetic field at various temperatures for W1 and W2. At 10 K, J_c for sample W1 is equal to 9.1 10^5 A/cm^2 and 1.8 10^4 A/cm^2 at 0 and 6 T, respectively. We underscore however that sample W2 presents a J_c value equal to 1.76 10^4 A/cm^2 at 15 K and 6 T. According to Fig.1-11 illustrating the J_c required for different applications, the results obtained with samples W1 and W2 show that MgB_2 bulks could be used in generators and motors. Otherwise, J_c values around 4 10^5 A/cm^2 and 2 10^5 A/cm^2 were measured in self-field for these two samples at 25 K and 30 K, respectively, i.e. in a range of temperatures compatible with the use of liquid hydrogen or liquid neon as cooling fluids. We emphasize that the reproducibility of the critical current density measured at 20 K on sample W1 has been verified, as can be seen in Fig.4-14(A) that reports $J_c(\mu_0 H)$ for an additional sample fabricated in the same conditions as W1.

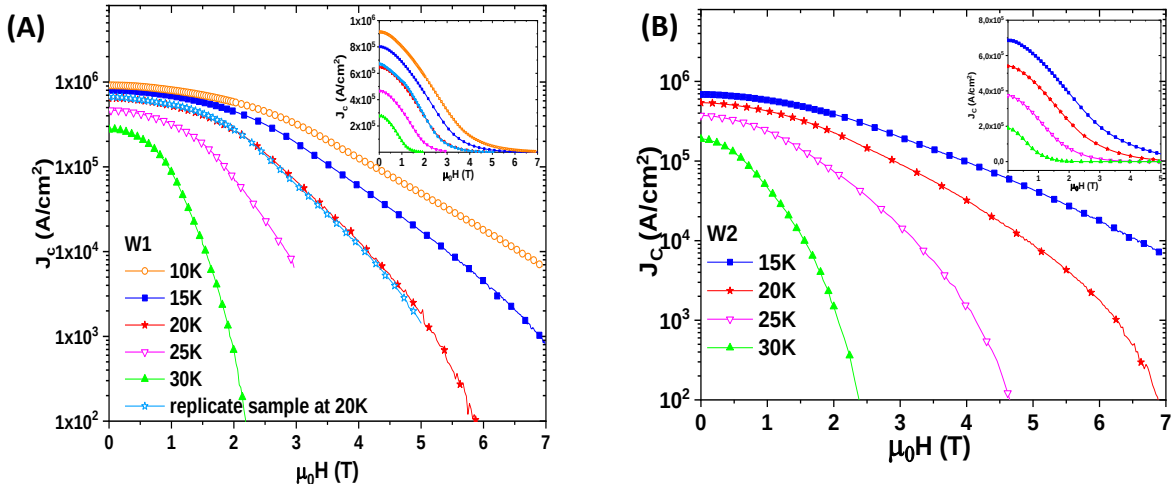

Fig.4-14: Magnetic field dependence of the critical current density J_c at various temperatures for (A) W1 and (B) W2 samples. The inset shows the same curves on a linear scale. Fig.4-13(A) also shows $J_c(\mu_0 H)$ for a replicate sample at 20 K.

We have also investigated the pinning mechanism of W1 and W2 at other temperatures using the Eisterer and Higuchi expressions (Fig.4-15(A and B)). The curves plotted using the Eisterer scaling function reveal that the dominant pinning centers in W1 and W2 are quite different, while there is no significant dependence on the temperature. No significant conclusions could be drawn from the Higuchi model (Fig.4-15(B).

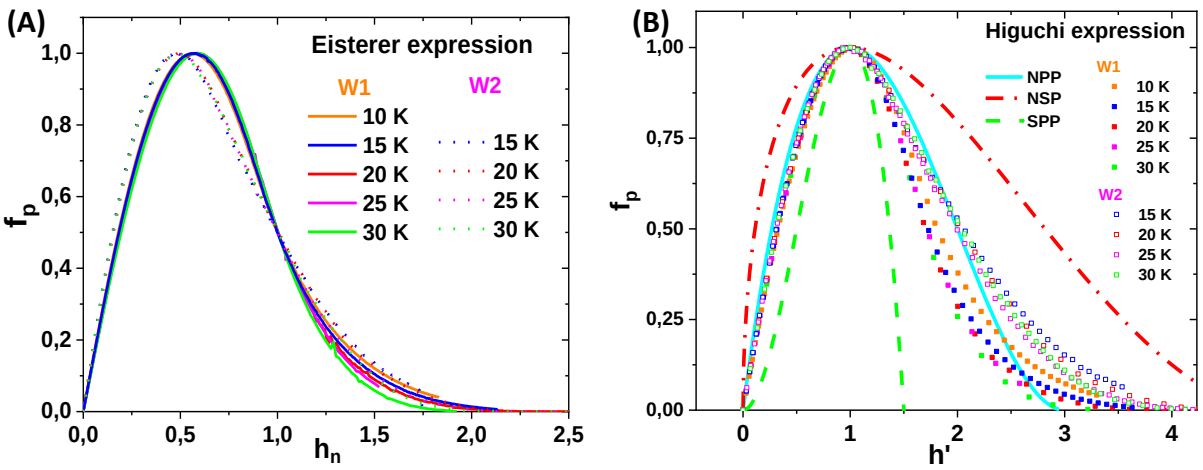

Fig.4-15: (A) Scaling behavior of normalized pinning force density f_p using Eisterer model for W1 and W2 samples at different temperatures. Lines represent the results of W1 samples and dot-lines represent those of W2. (B) scaling behavior of f_p using Higuchi model. The cyan line represents the non-superconducting point pinning NPP; the red dash-dot-line, non-superconducting surface pinning NSP and the green dash-line, superconducting point pinning SPP. Solid symbols: f_p vs. h' from 10-30 K for W1; open symbols: f_p vs. h' from 15-30 K for W2

4.3 Conclusions

In this chapter, we have investigated the effect of the SPS process conditions on the superconducting properties of the fabricated MgB_2 bulks. Firstly we have applied various sintering pressures (50-140 MPa) to prepare MgB_2 bulks with lot1 ex-situ and Mg+2B precursors at high temperature (950°C). MgB_2 samples were subsequently processed at 750°C under 300 MPa using specific tungsten carbide (WC) molds with Mg+2B and Mg+2B/C precursors. A remarkable increase in critical current density was observed with this technique, which can be attributed to the formation of nano-grains on the one hand and an enhancement of vortex pinning resulting from the presence of a large quantity of grain boundaries on the other hand. With respect to conventional graphite molds [68,69], WC molds sustain a larger pressure allowing a lower processing temperature and a better control of the grains size. The performances could probably be improved by the optimization of the applied pressure, sintering time and precursor doping. This will be the objectives of our future studies. Finally, we emphasize that we have prepared MgB_2 bulks in WC molds with the ex-situ and $Mg+MgB_4$ powders. The density of the obtained samples was low (<80%), even if they were sintered at 800°C. According to their DSC curves, we suppose that these two precursors require more heat for sintering and densifying than the in-situ powders we had previously used.

Chapter 5 Effect of chemical doping on highly dense MgB_2 bulks

The contaminant phase MgB_4 has been often observed after SPS sintering of MgB_2 bulks at a high temperature. Its presence has been attributed to the evaporation of magnesium, which was considered as harmful for the packing density, as well as the critical current density, J_c, under low magnetic field. This can be avoided by appropriate Mg addition and some studies have also shown that the J_c can be enhanced by excess Mg [130,131].

Furthermore, according to the prior research, chemical doping is one of the most efficient ways to improve the superconducting performances of MgB_2 materials, especially the carbon (C), titanium (Ti) and/or nano particles of silicone carbide (SiC) [35,56–58]. They play the role of pinning centers and allowing to improve the irreversibility magnetic field (H_{irr}), upper critical magnetic field (H_{c2}) and also enhancement of the critical current density (J_c) values under high magnetic fields.

As a consequence, this chapter discusses, on the one hand, the effect of excess Mg on the superconducting properties of the MgB_2 bulks, especially the critical current density. On the other hand, the effect of SiC dopants on the superconducting performances.

5.1 Mg addition

5.1.1 Sample preparation

The work has been carried out with two precursors: i) the ex-situ commercial powder MgB_2 (lot1) and ii) the mixture of magnesium and nano boron powder (Mg + 2B) for an "in-situ" reactive synthesis. Mg has been added to 1.5 g MgB_2 powder in the proportions of 0.5 wt%, 1 wt%, 3 wt% and 15 wt%. Three batches of samples with magnesium additions have been prepared: the first (batch 1) and the second one (batch 2) containing the commercial and the mixed powders, respectively, have been processed according to the conditions described in section 3.2.2, i.e. they have been sintered at 950°C and 100 MPa in 20 mm diameter graphite die without BN coating in the graphite foils. The third one consisting of Mg+2B powder with 0% and 1wt% Mg addition, respectively, was processed in WC molds in the same conditions as sample W1 (see section 4.2.1).

5.1.2 Structural, microstructural and superconducting properties

The density measured by the Archimede method and the XRD refinement results of each batch of samples are shown in table 5-1. We noted that the density of MgB_2 bulks could be improved to 99% by 3 wt% Mg adding for group 1 and 2 samples. While the c-parameter of the samples of these groups doped at 0.5%, 1% and 3% Mg is larger than the theoretical value (c = 3.524 Å [103]), that of the samples doped with 15% Mg is equal to the theoretical

one. Similar results were reported elsewhere [132,133]. The authors have supposed that they could be related to the lattice strains and the reduction of Mg-depleted phases. Based on the MgB_4 content and a rough calculation of the microstrains with the Maud software of the refinement [102], we have firstly concluded that Mg addition can inhibit the emergence of MgB_4. In addition, it can increase the MgB_2 content as well as the packing factor of the bulks sintered at high temperatures. Otherwise, the results suggest that if the MgB_4 phase is absent, excess Mg might reduce the microstrains during high-pressure sintering, resulting in the inhibition of *c*-parameter expansion. The amount of MgO shows no significant change due to the magnesium addition. A small amount of unreacted Mg has remained in the two samples with 15 wt% Mg and these two samples show a larger crystallite size than the other ones.

Table 5-1 : Density, lattice parameters, microstrain, amount of each phase and crystallite size of the fabricated bulks

starting powder	$d_{Archimedes}$ (g/cm^3)	Density (%)	a (Å)	c (Å)	Microstrain (%)	MgB_2 (wt%)	MgB_4 (wt%)	MgO (wt%)	Mg (wt%)	crystallite size (nm)
Batch 1 Ex-situ MgB_2 powder – Graphite mold										
0 %wt Mg	2.51	96	3.0843	3.5277	0.13	78.62	13.17	8.21	-	109
0.5 %wt Mg	2.51	96	3.0843	3.5276	0.133	81.26	10.77	7.98	-	105
1 %wt Mg	2.56	98	3.0844	3.5271	0.138	82.06	10.41	7.53	-	110
3 %wt Mg	2.6	99	3.0843	3.5272	0.133	88.83	3.73	7.44	-	105
15 %wt Mg	2.62	99	3.0841	3.5240	0.1	89.96	-	8.12	1.92	132
Batch 2 In-situ Mg+2B powder – Graphite mold										
0 %wt Mg	2.48	95	3.0854	3.5278	0.123	91.02	4.78	4.2	-	135
0.5 %wt Mg	2.55	97	3.0851	3.5273	0.122	91.3	4.44	4.26	-	125
1 %wt Mg	2.57	98	3.0852	3.5275	0.136	93.44	2.13	4.43	-	124
3 %wt Mg	2.61	99	3.0849	3.5273	0.116	93.55	1.16	5.28	-	124
15 %wt Mg	2.62	99	3.0859	3.5237	0.067	93.66	-	5.56	0.78	193
Batch 3 In-situ Mg+2B powder – WC mold										
0 %wt Mg	2.46	94	3.0854	3.5286	0.16	95.39	-	5.63	-	59-88
1 %wt Mg	2.52	96	3.0867	3.5262	0.136	95.49	-	4.51	-	76

Resistivity measurements have been carried out from 0 to 9 T on parallelepipedic samples cut from the samples of batch 1 and batch 2 with dimensions approximately equal to 1.5 x 1.5 x 10 mm^3. As shown in table 5-2, both samples with 15 wt% Mg show a slightly lower T_c than the other ones. The residual resistivity ratios (*RRR)* and connectivity (*K)* of the 15 wt% Mg excess samples are higher than the other Mg content added ones. This might indicate a higher crystallinity and intergrain coupling due to the unreacted Mg in the bulks [134,135]. The purity of the 1 to 3 wt% Mg excess ex-situ samples has slightly improved with Mg addition, but there is no significant improvement of the grain connectivity. On the contrary, the connectivity of the in-situ samples can be improved with 1 to 3 wt% excess Mg addition while there is no obvious variation in their *RRR* values. The irreversibility magnetic field, H_{irr} and upper critical magnetic field, H_{c2} of the samples were determined with the 10% and 90% normal-state resistivity at 40K (ρ_{40K}) and are plotted in Fig.5-1 as a function of the

temperature. We emphasize that although the 15 wt% Mg excess samples present a higher purity and grain connectivity than the other ones, they present the worst T_c, H_{irr} and H_{c2} of their respective batch.

Table 5-2 Offset critical temperature, measured resistivity values, residual resistivity ratios (RRR), connectivity (K), irreversibility magnetic field, H_{irr} and the upper critical magnetic field, H_{c2}

Sample	T_c (K)	ρ_{300K} (μΩcm)	ρ_{40K} (μΩcm)	RRR	K	H_{irr} at 20 K (T)	H_{c2} at 20 K (T)
Ex-situ 0 wt% Mg	37.6	34.3	10.5	3.27	0.266	6.3	8.4
Ex-situ 1 wt% Mg	37.6	31.8	9.2	3.46	0.279	6.4	8.6
Ex-situ 3 wt% Mg	37.6	32.4	8.9	3.63	0.269	6.4	8.6
Ex-situ 15 wt% Mg	36.6	17.2	4.5	3.78	0.500	5.8	8.1
In-situ 0 wt% Mg	38.6	36.6	5.9	6.2	0.206	6.5	8.3
In-situ 1 wt% Mg	38.6	19.0	3.6	5.30	0.409	6.7	8.4
In-situ 3 wt% Mg	38.6	18.2	3.4	5.32	0.428	6.6	8.3
In-situ 15 wt% Mg	37.6	13.8	2.0	6.77	0.536	5.9	7.9

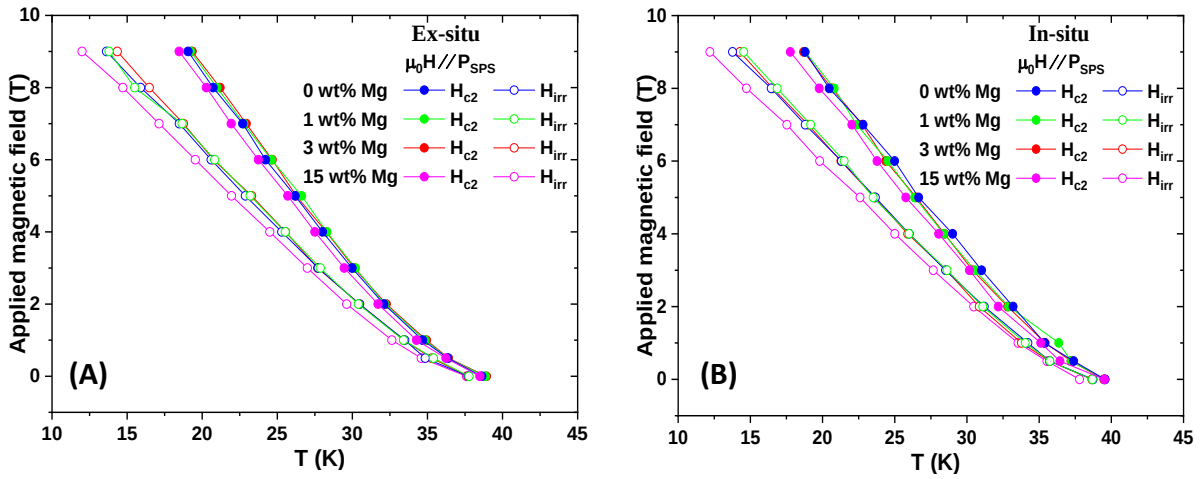

Fig.5-1:Temperature dependence of H_{c2} and H_{irr} for the (A) Ex-situ and (B) In-situ samples prepared by using graphite mold. H_{c2} and H_{irr} were determined from 90% and 10% of ρ_{40K}.

Specimens with dimensions of approximately 1.5 x 1.5 x 1.8 mm^3 were cut from the sintered bulks in order to verify their critical temperature, T_c and to estimate their critical current density, J_c with the SQUID magnetometer. We have firstly investigated the effect of Mg additions on the ex-situ samples of batch 1. Fig.5-2(A) shows their normalized magnetic moment curves as functions of the temperature. A low transition width (ΔT < 1 K) at the onset of the superconducting transition, $T_{c,\,onset}$ = 38 K, is observed for all the samples except the one with 15 % wt Mg addition. The T_c of this sample is the lowest of its batch, as previously shown by the resistivity measurements. This behavior was also reported by Hinks

D.G. et al.[132] using samples with unreacted Mg, in agreement with our results. Fig.5-2(B) shows the magnetic field dependence of the critical current density J_c at 20 K. The Mg addition has little effect on J_c. However, J_c for the 1 wt% Mg addition sample is slightly higher than the other ones in self-field and J_c for the 15 wt% Mg addition bulk decreases faster than the other ones under an applied field.

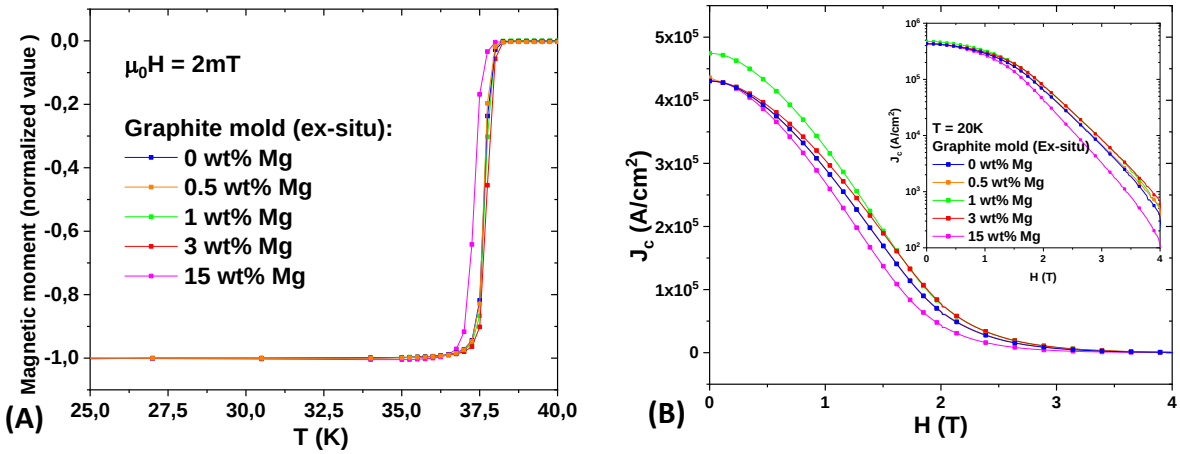

Fig.5-2: (A) Temperature dependence of the normalized magnetic moment of the samples of batch 1. (B) Magnetic field dependence of the critical current density J_c at 20 K of the samples of batch 1. The inset shows the same curves on a logarithmic scale.

Then, we have measured the T_c and J_c of the in-situ samples which have been sintered at high temperatures (batch 2). As for our previous results, the 15 wt% Mg excess sample shows a lower T_c value than the others (Fig.5-3(A)). Fig.5-3(B) shows J_c measured at 20 K. Unlike the ex-situ samples, a strong influence of Mg addition on J_c is observed below 2 T. Compared to the pristine sample, there is respectively about 4%, 29% and 19% improvement of J_c in self-field for the samples with 0.5 wt%, 1 wt% and 3 wt% Mg addition. The improvement of J_c could be related to the reduction of the MgB_4 content and the improvement of the grain connectivity. However, the remaining Mg and low microstrain in the 15 wt% excess Mg sample could be harmful to J_c. In addition, the effect of Mg addition is not beneficial at high fields (>3 T). Comparing these results to those obtained with the ex-situ samples, we conclude that Mg addition helps to improve the grain connectivity during the in-situ SPS process, resulting in an enhancement of J_c at weak magnetic fields. However, excessive Mg addition can affect the lattice structure and the microstrains in the MgB_2 phase, thus decreasing J_c.

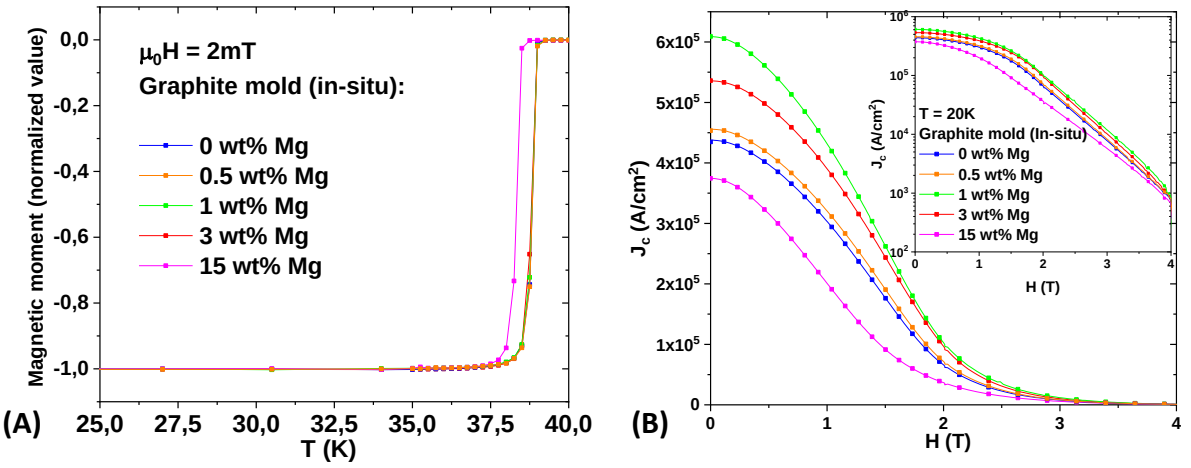

Fig.5-3: (A) Temperature dependence of the normalized magnetic moment of the batch 2 samples. (B) Magnetic field dependence of the critical current density J_c at 20 K of the batch 2 samples. The inset shows the same curves on a logarithmic scale.

To verify our hypotheses, we have fabricated the samples of batch 3, which were sintered at low temperature with the in-situ Mg+2B powder. Fig.5-4 shows the superconducting properties of the pristine sample and of the sample with 1 wt% Mg added. The onset of the superconducting transition, $T_{c,onset}$ of the 1 wt% Mg added sample is slightly higher than that of the pristine one (Fig.5-4(A)). This might be linked to the reaction between excess Mg and unreacted boron during the low-temperature sintering of the sample, which has been mentioned in section 4.2.2. The critical current density, J_c of the 1 wt% Mg added sample is lower than that of the reference sample (Fig.5-4(B)). There is no MgB_4 in the pristine sample and no remaining Mg in the 1 wt% Mg added sample. Consequently, the decrease of the J_c value could be correlated to the lattice structure of the 1 wt% Mg added sample and to microstains.

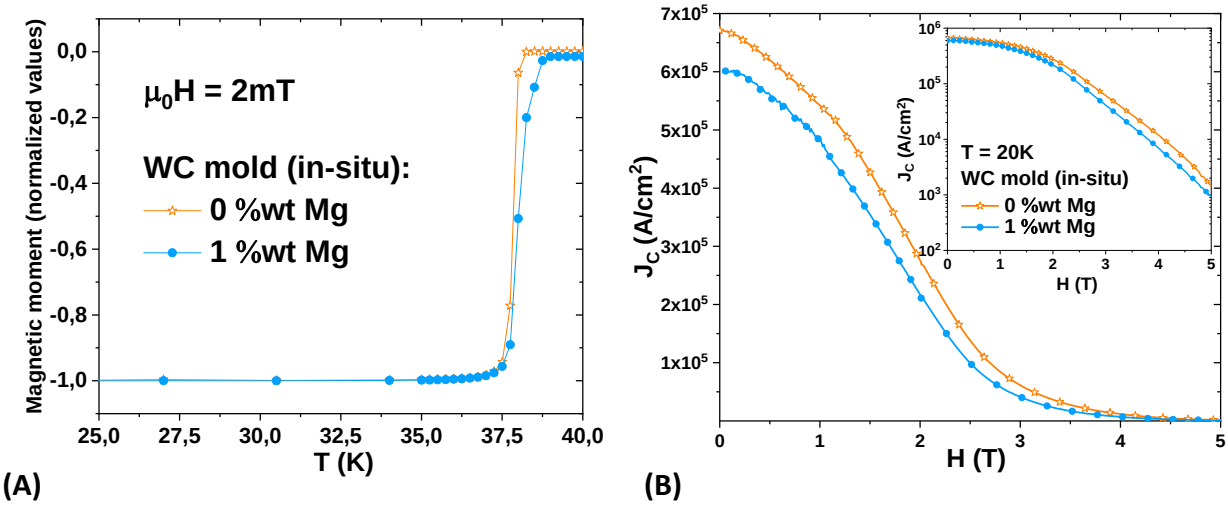

Fig.5-4: (A) Temperature dependence of the normalized magnetic moment of the samples of batch 3; (B) Magnetic field dependence of the critical current density J_c at 20 K of the samples of batch 3. The inset shows the same curves on a logarithmic scale.

5.2 SiC doping effect

It is well-known that to obtain significant irreversibility (H_{irr}) and upper critical (H_{c2}) magnetic fields as well as high critical current densities (J_c), one of the most effective candidates for doping MgB_2 is nano-SiC [35,136–139], which can play the role of a source for C substitution. In this section, we have focused on the effect of SiC doping on in-situ MgB_2 samples sintered by SPS. Two different SiC powders have been used for this study:

i) α-SiC (hexagonal phase, purity ≥97.5%, 37µm, provided by Sigma-Aldrich, USA), named micro-SiC in what follows.

ii) β-SiC (cubic phase, 45-55nm, provided by Alfa Aesar, USA), called nano-SiC thereafter.

5.1.2 Sample preparation

Two batches of SiC-doped MgB_2 samples have been prepared. The samples of batch 1 were fabricated using the same SPS process as samples W1 and W2, i.e., they have been sintered at 750°C and 300 MPa in WC molds. They consisted of i) an un-doped sample; ii) three samples doped with different nano-SiC amounts (5, 10 and 15 wt%) and iii) a sample doped with 10 wt% micro-SiC. The other batch consisted of i) an un-doped sample and ii) a 10 wt% nano-SiC doped sample. These samples were fabricated in the same conditions as samples C1 and C2, i.e., a processing at 950°C and 100 MPa using graphite molds.

5.1.2 Structure and morphological properties

The density determined by the Archimedes method and the XRD refinement results of each sample are reported in table 5-3. Compared to the undoped samples sintered in WC molds, the density of the nano-SiC doped samples is slightly lower, and there is no significant variation for the micro-SiC doped sample. The nano-SiC doped sample prepared in the graphite mold shows a dramatic density drop. This can be linked with the pores formed by the evaporation of Mg, which results in the formation of a large quantity of MgB_4. We also observe that the MgB_4 phase is present in the 15 wt% nano-SiC doped sample prepared at low temperature. According to the exothermal reaction between Mg and nano-SiC [136]:

$$2Mg+SiC \longrightarrow Mg_2Si+C$$

and due to the heating source of the SPS, we have supposed that when the current has passed through the Mg and SiC grains, the local temperature has reached that required for the formation of MgB_4.

As mentioned in section 4.2.2, the carbon substitution level, 2x in $Mg(B_{1-x}C_x)_2$, can be estimated with the expression proposed by M. Avdeev et al. [127] and the quantity 2x of each doped sample is shown in table 5-3. The C substitution increases with the amount of nano-SiC. The samples prepared in graphite mold seem to have more C atoms substituted at the boron sites. We also observe that the micro-SiC has not reacted with Mg, resulting in no C

atom substitution in this sample. Remaining SiC is present in each doped sample. There is no obvious effect of SiC doping on the MgO content or estimated crystallite size.

Table 5-3 Density, lattice parameters, amount of each phase and crystallite size of the fabricated bulks

starting powder	$d_{Archimedes}$ (g/cm^3)	Density (%)	a (Å)	c (Å)	c/a	2x in $Mg(B_{1-x}C_x)_2$	MgB_2 (wt%)	MgB_4 (wt%)	MgO (wt%)	Mg_2Si (wt%)	SiC (wt%)	crystallite size (nm)
Batch 1 In-situ Mg+2B powder – WC mold												
0 %wt SiC	2.46	94	3.0854	3.5286	1.1436	-	95.39	-	5.63	-	-	59-88
5 %wt nano-SiC	2.42	92	3.0848	3.5298	1.1443	0.0105	95.21	-	2.81	0.65	1.33 (α)	73
10 %wt nano-SiC	2.36	90	3.0839	3.5314	1.1451	0.0225	85.49	-	6.96	2.24	5.31 (α)	68
15 %wt nano-SiC	2.4	92	3.0813	3.5329	1.1466	0.045	71.23	8.61	7.5	3.5	9.2 (α)	83
10 %wt micro-SiC	2.45	94	3.0861	3.5294	1.1436	0	88.14	-	3.54	-	8.32 (β)	71
Batch 2 In-situ Mg+2B powder – Graphite mold												
0 %wt SiC	2.48	95	3.0863	3.5274	1.1429	-	89.17	6.66	4.16	-	-	134
10 %wt nano-SiC	2.25	86	3.0794	3.5294	1.1461	0.048	66.26	17.91	6.55	5.09	4.19 (α)	133

The microstructures of the fracture surface of the bulks prepared in WC molds doped with 10 wt% micro- and nano-SiC and 15 wt% nano-SiC are shown in Fig.5-5. Their chemical compositions have been determined with back-scattered electrons (see Fig.5-5(A-C)), while the topographic view of the MgB_2 grains was observed with secondary electrons (see Fig.5-5(D-E)). The white regions in the 10 wt% micro-SiC doped sample (Fig.5-5(A)) are micro-SiC grains, which have not reacted with Mg during SPS sintering, in agreement with the XRD refinement results. The white regions in the sample with 10 wt% added nano-SiC (Fig.5-5(B)) correspond to the Mg_2Si phase as confirmed by EDS analysis (see below). The 15 wt% nano-SiC added sample shows an inhomogeneous microstructure with unidentifiable phases. According to the morphology of the MgB_2 grains in these three samples (Fig.5-5(D)-(F)) and EDS analysis, the small tiny white particles present at the grain boundaries of the samples might consist either of carbon or of Mg_2Si. These compounds could be harmful to the grain connectivity.

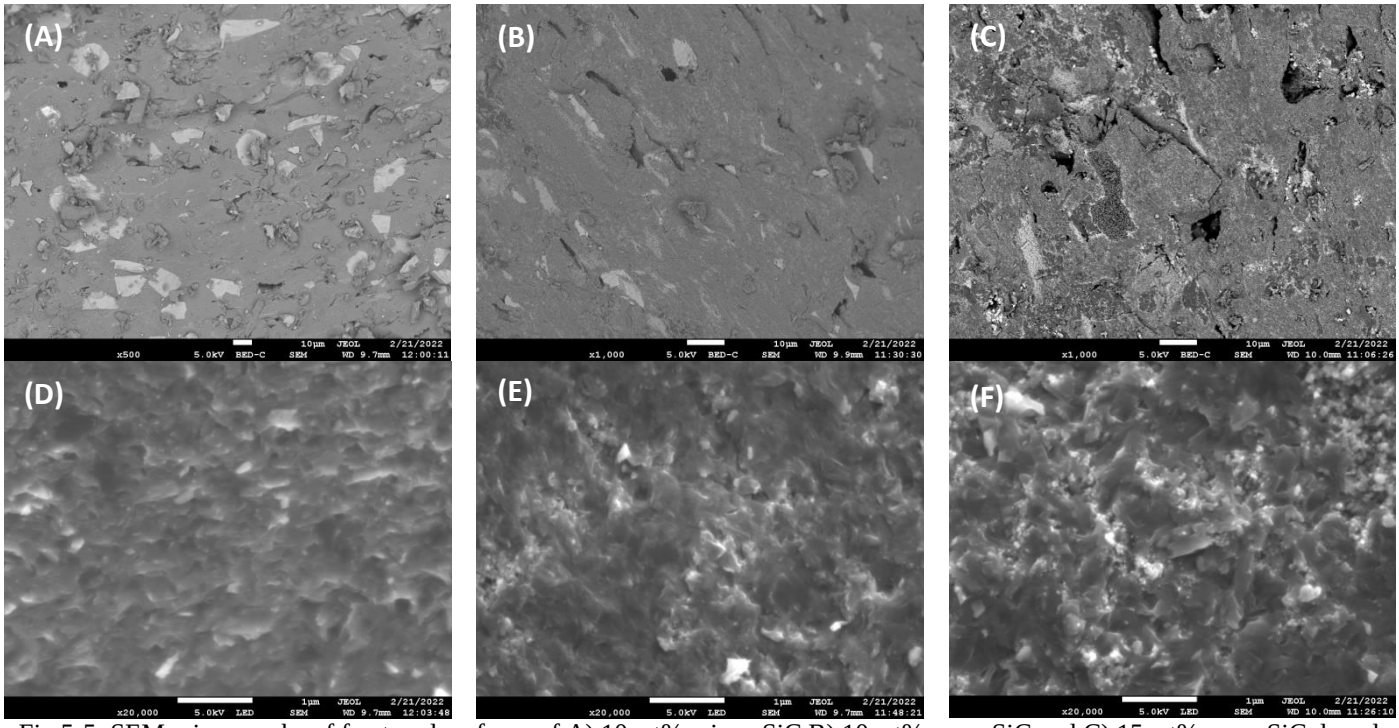

Fig.5-5: SEM micrographs of fractured surfaces of A) 10 wt% micro-SiC B) 10 wt% nano-SiC and C) 15 wt% nano-SiC doped samples sintered in WC mold and magnification of MgB_2 grains in the 10 wt% micro-SiC (D), 10 wt% nano-SiC (E) and 15 wt% nano-SiC (F) doped samples.

Fig.5-6(A) and table 5-4 show the EDS analysis of the 10 wt% nano-SiC doped sample. The white zone 1 corresponds to the Mg_2Si contaminant and the presence of Si and C elements can be observed in the MgB_2 phase (zone2). Otherwise, we have tried to identify the phases present in the 15 wt% nano-SiC added sample. Four regions were selected (see Fig.5-6(B)) for this purpose. The mass percentages of each element are shown in table 5-5. The only clear compositions are the mixed phases MgB_2 and Mg_2Si present in zone 3 and MgO present in zone 4. An EDS analysis on a polished surface would be necessary to further identify the components present in this sample.

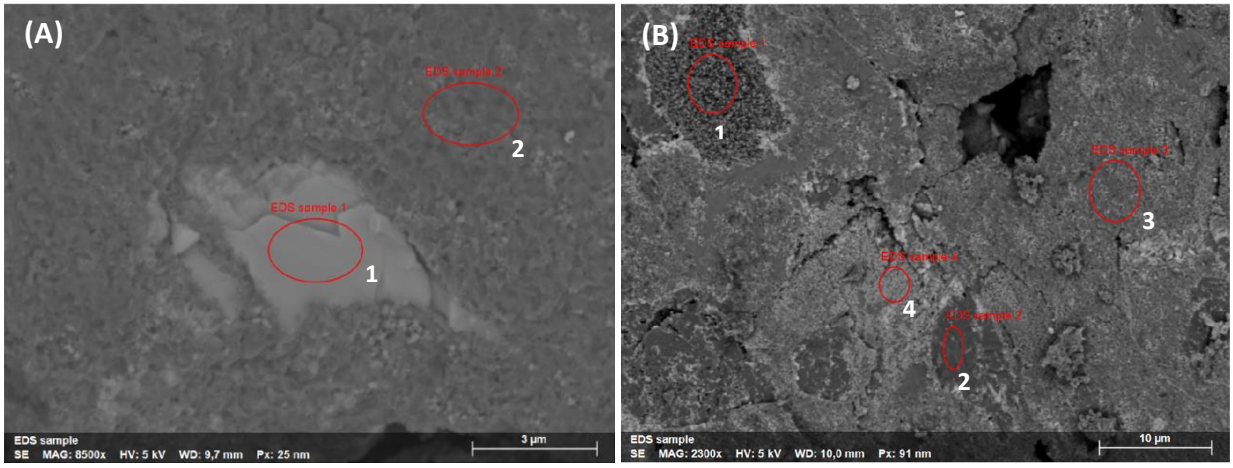

Fig.5-6: EDS analysis of the A) 10 wt% and B) 15 wt% nano-SiC doped samples sintered in WC molds

Table 5-4 mass percentages of elements in selected zones of Fig.5-6(A) estimated by EDS analysis.

Element	Mg	B	O	Si	C
wt % (Zone1)	45.7	1.7	1.8	50.1	0.7
wt % (Zone2)	46.1	40.2	3.4	8.4	1.9

Table 5-5 mass percentages of elements in selected zones of Fig.5-6(B) estimated by EDS analysis.

Element	Mg	B	O	Si	C
wt % (Zone1)	29.8	6.7	17	1.5	0.6
wt % (Zone2)	45.2	31.2	14.4	8.7	1
wt % (Zone3)	54.1	19.2	3.7	21.1	1.9
wt % (Zone4)	58.4	1.9	36.2	3	0.5

5.1.3 Superconducting properties

The resistivity of 10 wt% nano doped samples prepared in different molds was carried out on rectangle bars with dimensions approximately equal to 1.5*1.5*10 mm^3 by the DC 4-probes method up to 14 T. The detailed results are shown in table 5-6 and compared to the characteristics of undoped samples. Both doped samples show lower *RRR* and *K* values than the undoped ones, which indicates a reduction of their purity and grain connectivity. This is especially the case of the sample sintered at high temperature with the graphite mold and is probably linked to the significant decrease in T_c of this sample. Fields H_{irr} and H_{c2} determined by the 10% and 90% normal-state resistivity at 40 K [88,94], are plotted in Fig.5-7 as function~~s~~ of the temperature. Contrary to the purity and the connectivity, a significant increase of these fields below about 30 K can be observed in both nano-SiC doped samples.

Table 5-6 Offset critical temperature, measured resistivity values, residual resistivity ratios (RRR), connectivity (K), irreversibility magnetic field, H_{irr} and the upper critical magnetic field, H_{c2}

Sample	T_c (K)	ρ_{300K} (μΩcm)	ρ_{40K} (μΩcm)	RRR	K	H_{irr} at 20 K (T)	H_{c2} at 20 K (T)
WC mold 0 wt% nano-SiC	37.6	43.8	17.09	2.56	0.237	7.9	9.7
WC mold 10 wt% nano-SiC	37.6	67.1	33.1	2.03	0.186	9.3	12.2
Graphite mold 0 wt% nano-SiC	38.6	16.5	2.9	5.65	0.466	6.6	8.2
Graphite mold 10 wt% nano-SiC	35.6	120.2	59.5	2.02	0.104	8.3	11.8

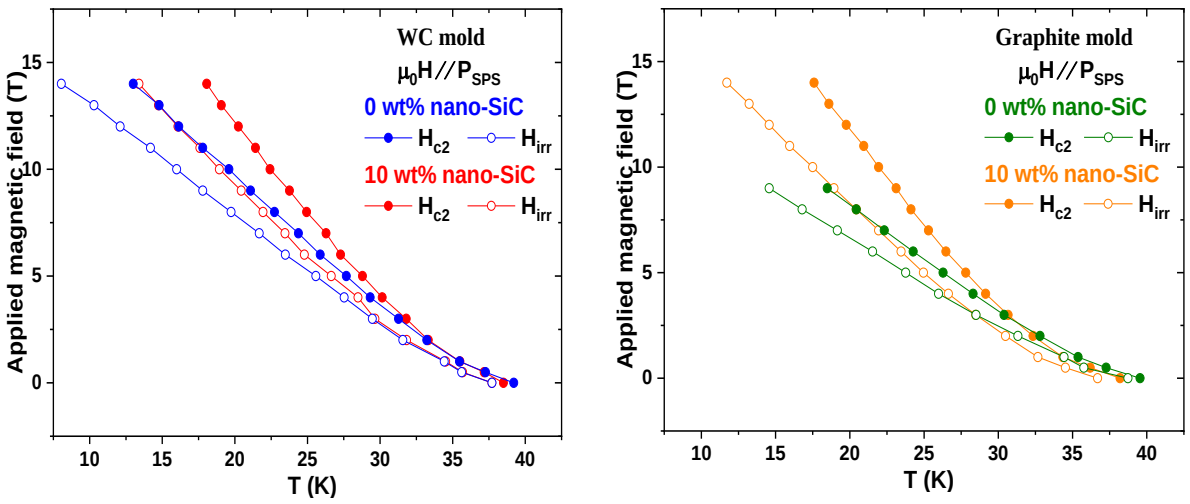

Fig.5-7: Temperature dependence of H_{c2} and H_{irr} for the samples prepared in (A) WC mold and (B) Tc graphite mold. H_{c2} and H_{irr} were determined from 90% and 10% of ρ_{40K}.

Magnetic moment measurement have been carried out on these samples with the SQUID magnetometer. Small specimens with dimensions around 1.5*1.5*1.8 mm^3 were cut from the sintered bulks. Fig.5-8(A) shows their normalized magnetic moment as functions of the temperature. The transition temperature of the nano-SiC doped sample prepared in a WC mold is slightly lower than that of the undoped sample. The doped sample prepared at high temperature in a graphite mold shows a dramatic drop in T_c, as shown by the resistivity measurement. The J_c of each sample versus applied field is plotted in Fig.5-8(B). SiC doping is harmful to J_c in weak field as a consequence of the weak intergrain coupling and low purity of the samples. However, the doped samples have a higher J_c than the undoped ones above 3 T, suggesting the presence of a large number of pinning centers. In addition, the samples prepared in the WC molds always show higher performances than those prepared in graphite molds as a probable result of their smaller MgB_2 grains and of the absence of the MgB_4 phase.

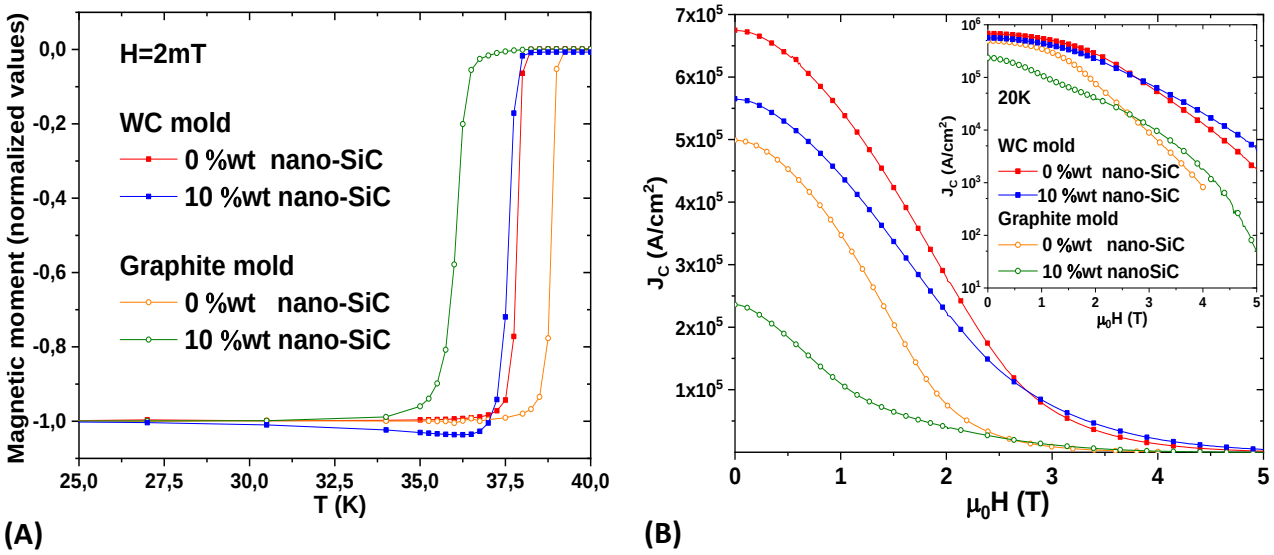

Fig.5-8: (A) Normalized magnetic moment as a function of the temperature for the 0 and 10 wt% nano-SiC doped samples sintered in different molds. (B) Magnetic field dependence of the critical current density J_c at 20 K. The inset shows the same curves on a logarithmic scale.

Then we have investigated the effects of 10 wt% micro- and nano-SiC doping on the superconducting properties of the samples prepared in WC molds. As shown in Fig.5-9(A), there is no change in T_c for the micro-SiC doped sample, while its J_c is lower than that the undoped sample at both low and high fields (Fig.5-9(B)). As a consequence, unreacted micro-SiC grains can't be the pinning centers in MgB_2 bulks.

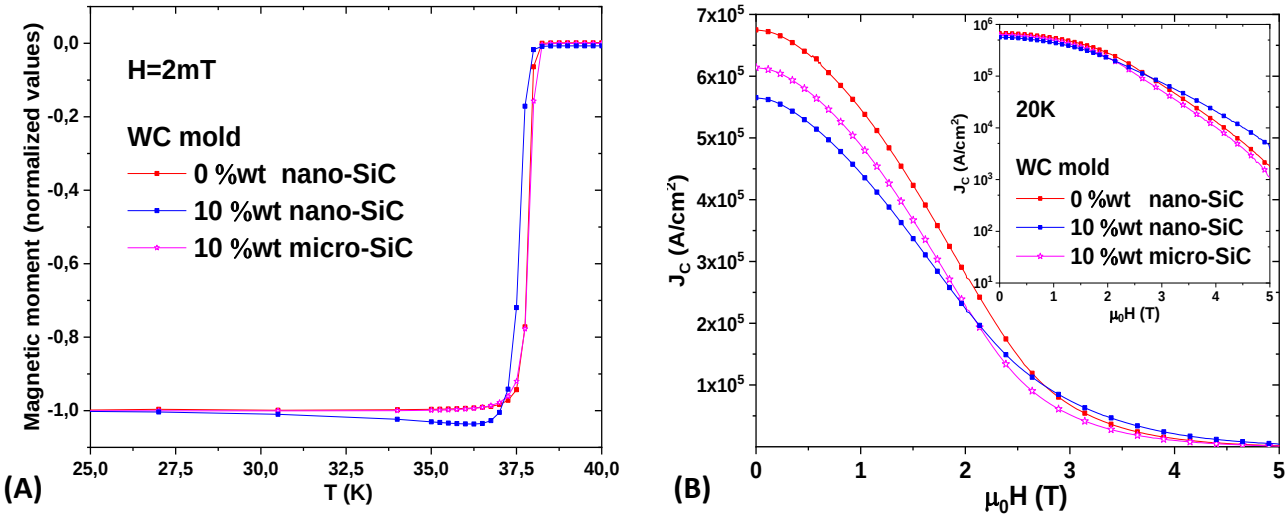

Fig.5-9: (A) Normalized magnetic moment as a function of the temperature for the 0 and 10 wt% micro- and nano-SiC doped samples sintered in WC molds. (B) Magnetic field dependence of the critical current density J_c at 20 K. The inset shows the same curves on a logarithmic scale.

Fig.5-10 shows the superconducting performances of samples fabricated in WC molds and doped with various amounts of nano-SiC. The 15 wt% doped sample shows a lower $T_{c,\,onset}$ = 37.25 K than the others (Fig.5-10(A)) due to its higher content in secondary phases as shown in table 5-3. In addition, its J_c is much lower than the others below 3 T (Fig.5-10(B)). The best J_c at high field is that of the 10 wt% doped sample with J_c = 4574 A/cm^2 at 5 T and 20 K. However, SiC doping results in a smaller improvement of J_c at high field than the use of carbon-coated boron powder, as can be seen by comparison with sample W2 (J_c = 10^4 A/cm^2 at 5 T and 20 K).

However, Prikhna et al. [35] have reported that they have obtained high J_c at both low and high fields with 10 wt% nano-SiC doped samples prepared at high temperature and high pressure (1050°C and 2 GPa). The high density and strong grain connectivity of their samples can be related to the absence of Mg_2Si impurities. According to the Gibbs energy of the reaction between SiC and Mg [140], the higher the sintering temperature, the more inhibited is the reaction. In our case, the heat generated by this reaction might cause local overheating and evaporates Mg. As a consequence, to further improve the performances of SiC doping samples, other sintering conditions need to be investigated.

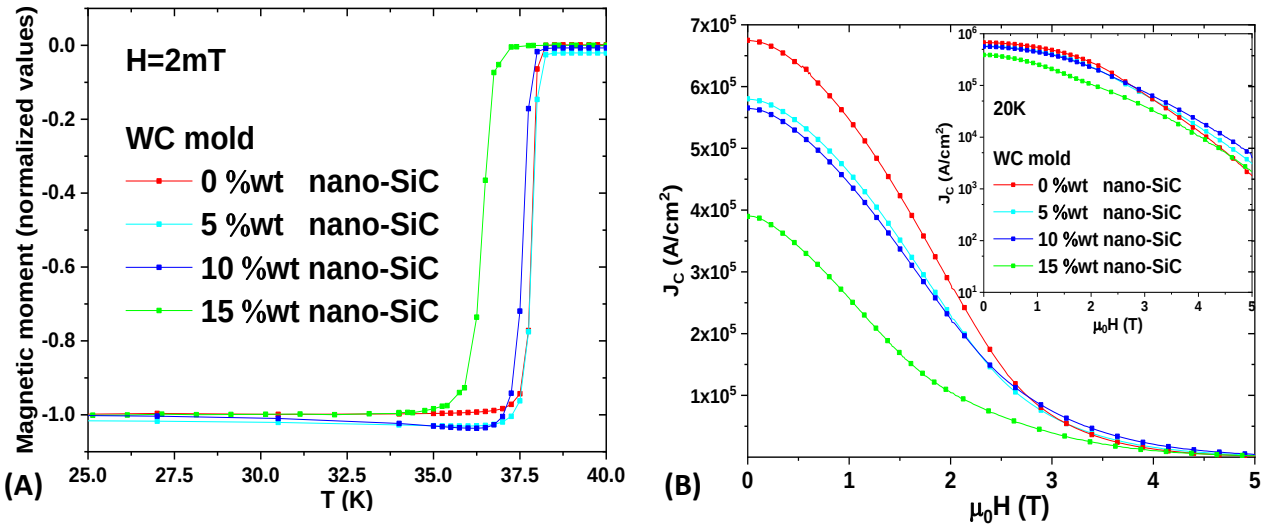

Fig.5-10: (A) Normalized magnetic moment as a function of the temperature for the different amount nano-SiC doped samples sintered in WC mold. (B) Magnetic field dependence of the critical current density J_c at 20 K. The inset shows the same curves on a logarithmic scale.

5.3 Conclusions

In this chapter, we have investigated chemical doping effects on the bulks MgB_2 sintered by SPS. A moderate Mg addition in the in-situ samples sintered at high temperatures can improve their purity (samples composition) and intergrain connectivity and consequently, the critical current density J_c at low fields. Otherwise, we have investigated the SiC doping effects on in-situ samples sintered at low and high temperatures. The nano-SiC shows a similar effect to that of the carbon-coated boron powder, basically, the J_c is weakened at low fields but increased at high fields. However, in this stage of this study, the nano-SiC doping doesn't result in an obvious improvement of the superconducting performances as compared to that of the carbon-coated boron powder.

Chapter 6 Functional properties measurements of large size bulk superconductors

In this chapter we investigate the functional properties of large size MgB_2 discs, especially the magnetic levitation force, the stability conditions of levitation as well as the magnetic field which can be trapped by these samples.

6.1 Fabrication of the samples

Two batches of MgB_2 samples were prepared with lot1 of the ex-situ powder purchased from Pavazyum company (Turkey). The first one consisted of 50 mm diameter cylindrical bulks, the thicknesses *h* of which were in the range 2-10 mm. The other one consisted of 10 mm thick bulks, with diameters, D_{SC}, ranging between 20 mm and 80 mm. The powder was weighed to make the discs with the desired diameters and thicknesses, then introduced into graphite dies. The samples were sintered at 1100 °C for 45 min while an axial pressure of 50 MPa was applied under dynamic vacuum (10^{-3} bar). The obtained samples have usually shown a relative density larger than 98%. Fig.6-1 shows a picture of the fabricated samples.

Fig.6-1: Photograph of ex-situ MgB_2 bulks with (A) various thickness and (B) various diameters.

6.2 Levitation force and guidance force measurements

Superconducting Magnetic levitation (SML) is the root of some promising applications of superconductors, especially Maglev trains and superconducting bearings. The levitation force between a permanent magnet and a superconductor can be stable and requires no energy except for the system cooling. The levitation force and its stability are closely related to the

superconducting material, the system generating the magnetic field (magnets or assembly of magnets and soft iron parts) and their geometrical dimensions. In this study, we have investigated in our lab the influence of the dimensions of the MgB_2 bulks and that of the working temperature on their levitation and lateral forces. Other measurements have been carried out at the Laboratory of Magnet Engineering and Applied Superconductivity (LIMSA) of the University of Bologna (Unibo), with a system that allows measuring forces down to a very low separation between the magnetic source and the superconductor. One of the objectives of this study was to compare the levitation and guidance forces measurements carried out at CRISMAT to those carried out at LIMSA. Otherwise, we wanted to compare our analytical model [141,142] to the numerical model used by Prof. Morandi team [143,144].

6.2.1 Effect of the sample diameter

A detailed description of the measuring system and of the experimental protocol have been presented in Chapter 2. The effect of the diameter of the MgB_2 bulks (D_{SC}) on the levitation and lateral forces was studied at 20 K with a NdFeB 70 mm diameter and 35 mm thick permanent magnet. The levitation forces of 10 mm thick MgB_2 bulks cooled down at Z_{cp} = 30 mm with D_{SC} ranging between 30 mm and 80 mm are plotted in Fig.6-2(A). The levitation force increases with the increasing diameter of the superconductor, D_{SC}. The maximum force that was obtained with the 80 mm diameter disc was equal to 200 N at Z_{min} = 12 mm. Fig.6-2(B) shows the force measured at 20 K as a function of the bulk diameter for a magnet–superconductor separation equal to 12 mm. Clearly, the levitation force is proportional to D_{SC}^3 not to D_{SC}, as indicated by the relations Eq.2.6-14 and in [83].

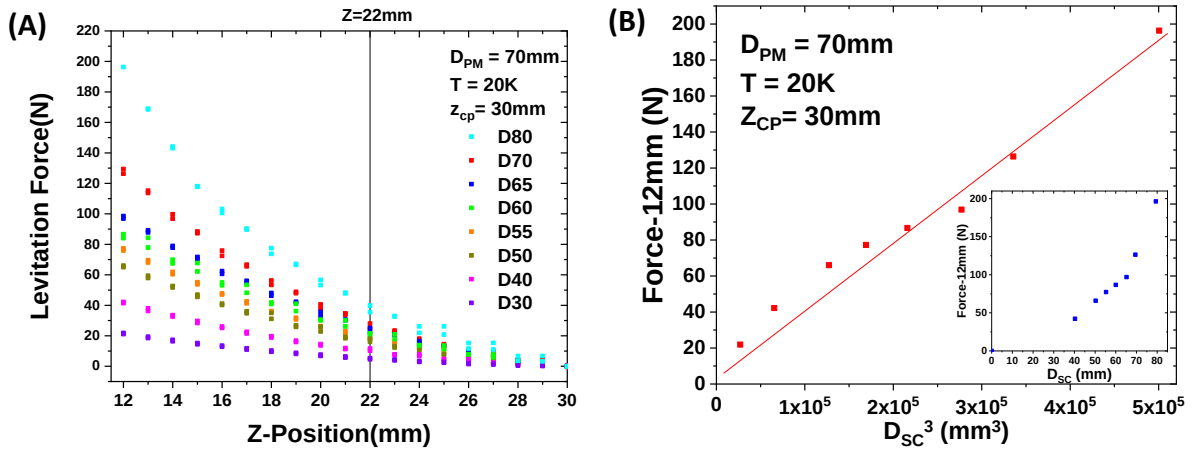

Fig.6-2: (A) Levitation force measurement carried out between a 70 mm diameter magnet and 10 mm thick MgB_2 bulks with various diameters at 20 K and Z_{cp}=30 mm. (B) Levitation force measured at Z_{min} = 12 mm as a function of D_{SC}^3. The inset shows the levitation force as a function of D_{SC}.

Stability is the most crucial characteristic of Superconducting Magnetic Levitation (SML) systems. It depends on the lateral stiffness of the considered SML system. Generally, the stiffness is determined by measuring the slope of minor loops of the lateral force F_Y, with respect to the lateral distance between the magnet and the superconductor, Y. Stability corresponds to a negative stiffness while the stiffness is positive when the system is unstable [145,146]. Fig.6-3 shows the lateral force measured at 20 K at Z = 30 mm, 22 mm and 20 mm

after cooling down the MgB_2 discs at Z_{CP} = 30 mm and Y = 0 mm. Since the lateral force cycles show no hysteresis, the slope of any minor loops is the same as that of the major one and we can assume that the lateral stiffness is equal to the slope of the *Fy(Y)* plots. At Z = 30 mm (Fig.6-3(A)), the SML system was stable for all the samples as shown by the negative slope of their lateral force. The absolute value of the sample stiffness increases as the diameter of the discs increases, (-0.46 for D_{SC} = 80 mm and -0.06 for D_{SC} = 30 mm). The measurements of *Fy(Y)* carried out at Z = 22 mm and 20 mm are reported in Fig.6-3(B) and (C), respectively. For all the samples, except the 80 mm diameter one, in the vicinity of the origin (-10 mm < Y < 10 mm), the slope of $F_Y(Y)$, i.e the stiffness, is almost equal to zero for Z = 22 mm and is positive for Z = 20 mm. As a consequence, levitation is unstable for Z < 22 mm. Similar results were obtained when measuring F_Y either at different Z_{cp} or with other NdFeB magnets, as far as the condition $D_{PM} \geq D_{SC}$ was fulfilled [129]. These results are also similar to those reported in [147]. If $D_{PM} < D_{SC}$, as in the case of the 80 mm diameter disc, the separation between the disc and the magnet below which levitation is unstable decreases, as seen in Fig.6-3(D) that shows that the system is stable down to 18 mm. As an important consequence, the maximum levitation force keeping stability at 20 K for the system consisting of a 70 mm NdFeB magnet and the 80 mm diameter MgB_2 disc cooled down at Z_{CP} = 30 mm is around 80 N, well below the 200 N measured at 12 mm.

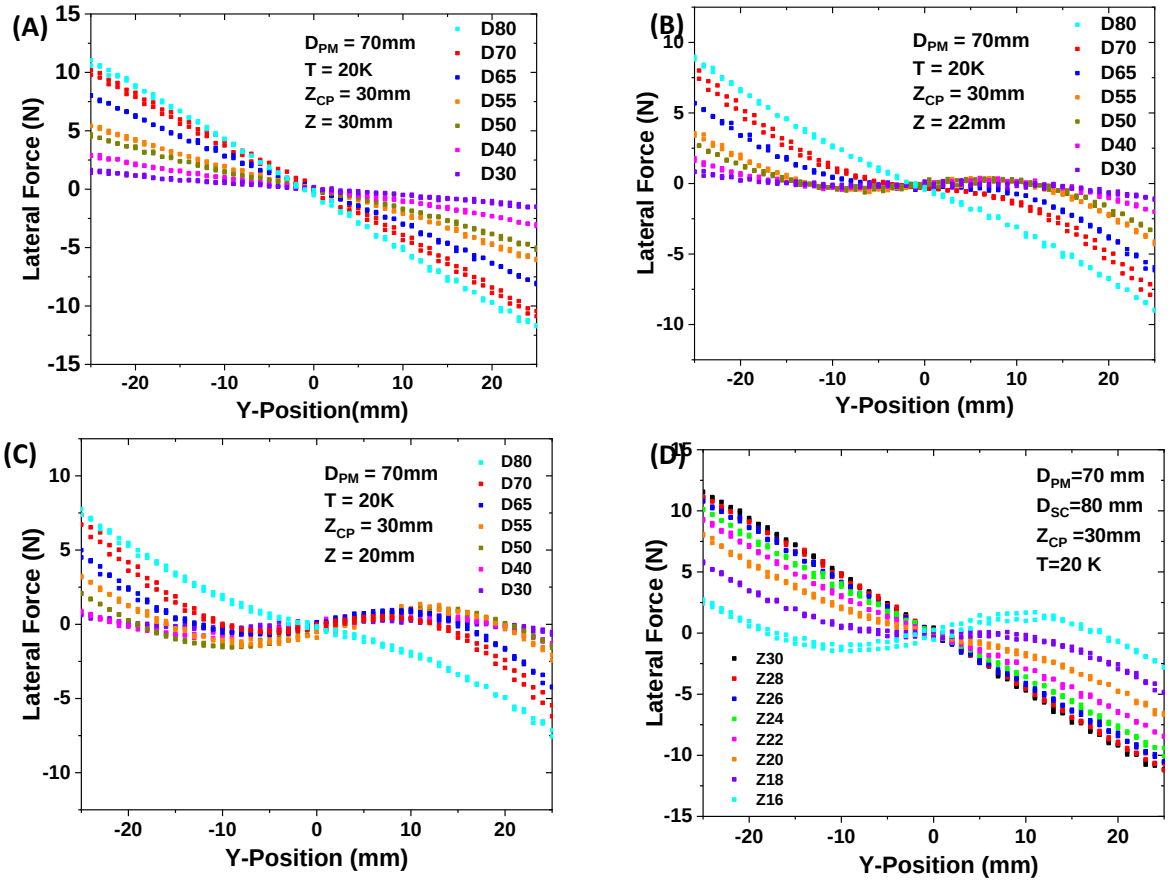

Fig.6-3: Lateral forces F_Y measured on MgB_2 discs with various diameters and the PM70 magnet at (A) Z = 30 mm, (B) Z = 22 mm and (C) Z = 20 mm after cooling down the MgB_2 discs at Z_{CP}=30 mm. (D) Lateral force F_Y measured with the 80 mm diameter MgB_2 disc at different magnet – disc separations, Z.

Conditions for the stability of a SML system consisting of a multi-seeded $YBa_2Cu_3O_{7-\delta}$ (YBCO) bulk and a Halbach guideway section were proposed by Li et al. [148]. The authors claim that stability depends on the sign of the eigenvalues of a linearized Jacobian matrix. Wang et al. have computed the guidance force of an infinitely long rectangular superconductor above a Halbach guideway, but the calculations have shown strong discrepancies with the measurements [149]. Numerical calculations on the stability of SML were also proposed in [150–152], however simple physical conditions determining the situations in which a SML system is stable or unstable have not been established yet. Our prior research [129] used extended Brandt relations (Eq.2.15-17) to calculate the lateral force and assumed that the stabilization of an SML system consisting of a superconductor bulk and a cylindrical permanent magnet depends on $B_\phi(Y,Z)$ in Eq.2.15. Stability exsits only if [129]:

$$B_\phi(0,Z) \leq \bar{B}_{PM}(0,Z_{cp}) \quad \text{[Eq.6.1]}$$

According to Eq.2.16, for a constant diameter of the magnet, one expects that $B_\phi(Y,Z)$ decreases as the superconductor diameter D_{SC} increases. It is the reason why the D80 sample exhibits a better stability than the others samples.

Force measurements on four 10 mm thick MgB_2 bulks with diameter D_{SC} equal to 50, 60, 65 and 70 mm, were carried out at LIMSA (Bologna). Fig.6-4(A) shows the resluts obtained at 20 K and Z_{cp} = 30 mm with a 70 mm diameter magnet. The maximum force is equal to 450 N and was measured at Z_{min} = 4 mm with the 70 mm diameter MgB_2 disc. Compared to the results obtained at CRISMAT (Fig.6-2(A)), larger forces are measured at LIMSA. The discrepancies might result from: i) the soft iron supports used to connect the magnet to the displacement system, that are not the same in both laboratories. These supports have an influence on the magnetic field generated by the NdFeB magnet; ii) an experimental error at CRISMAT on the cooling and the measurements positions (Z_{CP} and Z) due to the contraction of the sample holder during cooling and iii) a slight deformation of the measurement system at CRISMAT when measuring large forces. Consequently, we will focus on the results obtained at LIMSA in the following studies. Firstly, these measurements confirm the proportionality relation between D_{SC}^3 and the levitation force, as shown in Fig.6-4(B) that reports the forces measured at Z_{min} = 4 mm on the 10 mm thick samples.

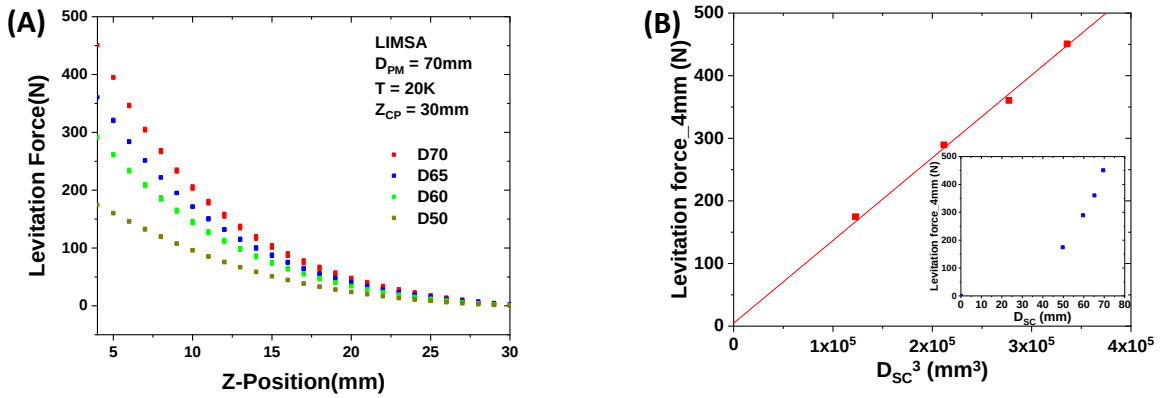

Fig.6-4: (A) Levitation forces carried out with various diameter MgB_2 bulks at LIMSA. (B) Levitation force measured at Z_{min} = 4 mm with a 70 mm diameter magnet as a function of D_{SC}^3. The inset shows the levitation force as a function of D_{SC}.

The lateral force measured at LIMSA between Y_0 and Y_{max} is plotted in Fig.6-5. At cooling height Z = 30 mm, the absolute value of $F_Y(Y)$ slope increases with increasing superconductor diameter, corresponding to the results observed with CRISMAT data (see Fig.6-3(A)). Concerning stability, the slope of the lateral force measured at Z = 20 mm is zero for all the samples, while it is positive, according to the measurements carried out at CRISMAT (except for the 80 mm diameter disc).

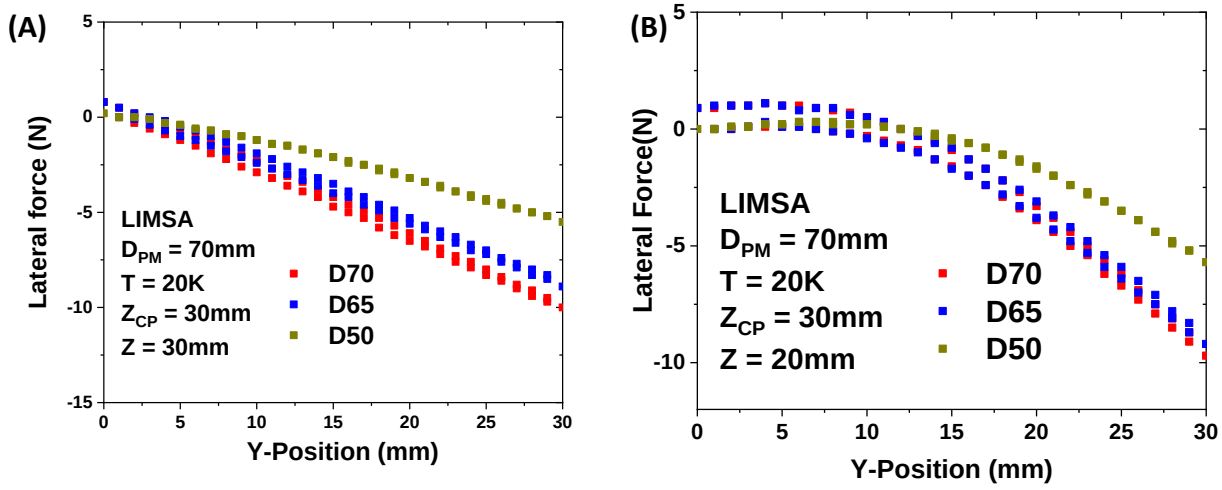

Fig.6-5: Lateral forces measured at (A) Z = 30 mm and (B) Z = 20 mm after cooling down the various diameter MgB_2 discs with various diameters at Z_{CP} = 30 mm and 20 K.

6.2.2 Effect of sample thickness

Our previous research results have shown that the currents possibly do not flow in the whole thickness of the superconductors. Thus, the thickness, h, of the samples has no significant effect on the levitation force, except if it is in the range of t, the thickness of the superconducting current layer [141]. We have investigated at LIMSA the levitation force of four 50 mm diameter discs with thicknesses respectively equal to 2, 2.9, 7.8 and 10 mm. The measurements have been carried out with the 70 mm NdFeB magnet after field cooling at 20 K and Z_{CP} = 30 mm (Fig.6-6(A)). The force cycle of the 10 mm thick disc coincides with that of the 7.5 mm thick one. The cycle of the 2 mm thick disc is slightly hysteretic. The forces measured at Z = 5 mm as a function of h are plotted in Fig.6-6(B). The difference between the forces measured on the 10 mm and the 7.5 mm discs are in the range of the errors on the measurements (5%), as could be expected from Fig.6-6(A). The forces measured on the 2.9 mm and the 2mm thick discs are lower than those measured on the thickest discs, but the the levitation forces are clearly far from beeing proportional to h, as they should be if t was equal to h. The results suggest that t for the measured discs lies above 2.9 mm.

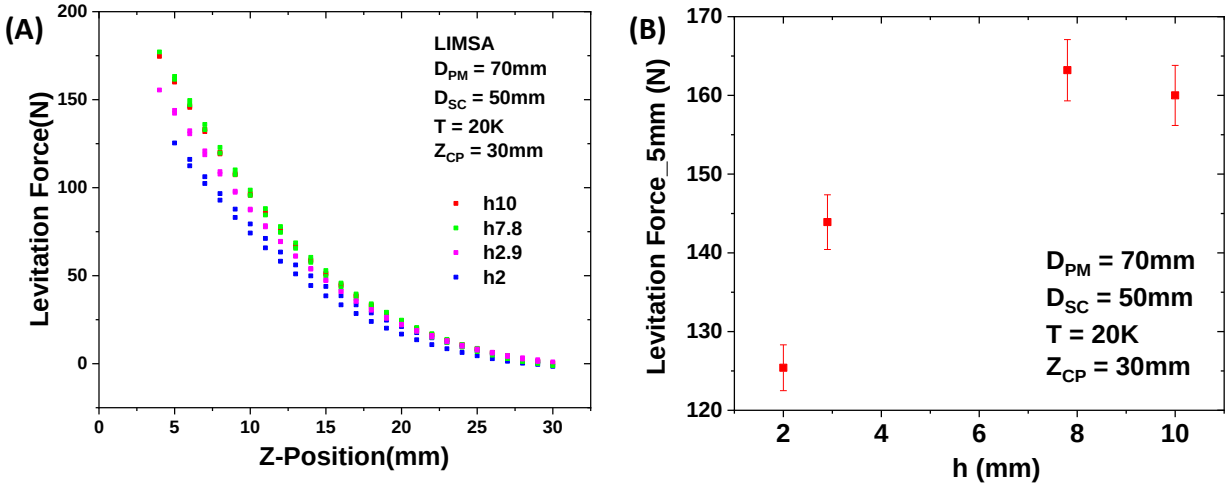

Fig.6-6: (A) Levitation forces carried out with various thick MgB_2 bulks at LIMSA. (B) Levitation force measured at Z_{min} = 5 mm as a function of sample thickness, h.

Measurements of the lateral force were carried out on these discs. The corresponding stiffness (taken as the slope of $F_Y(Y)$ between -10 mm < Y < 10 mm) is plotted in Fig.6-7 at $Z = Z_{CP}$ = 30 mm and Z = 24 mm. At $Z = Z_{CP}$ the stiffness slightly decreases with h down to h = 2.9 mm (Fig. 6-7(A)) . At Z = 24 mm, the stiffness is positive for h = 2 mm (Fig.6-7(B)). Figs.6-7(A) and (B) show that the stiffness of systems including thick superconducting discs is better than that of those including thinner ones, suggesting that the stability of the SML systems could be optimized using superconductors with a suitable thickness.

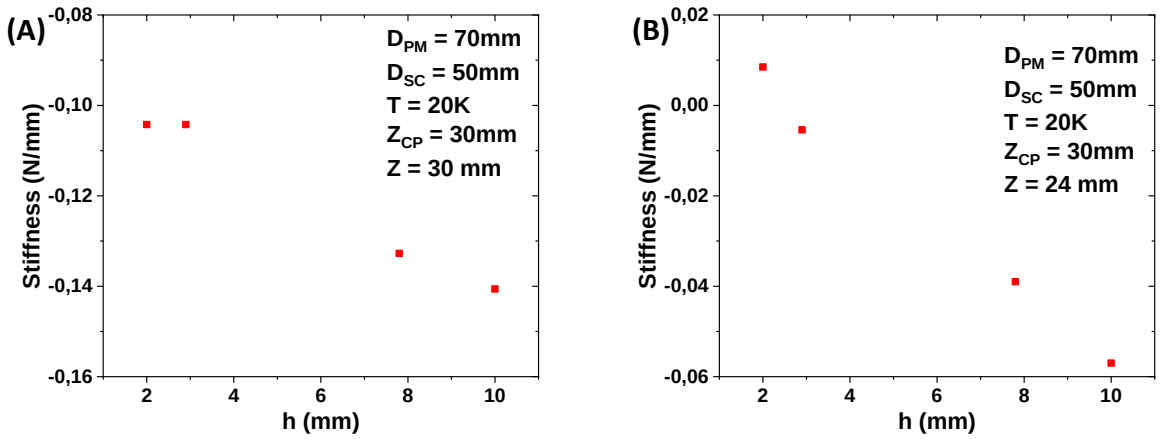

Fig.6-7: Lateral stiffness as a function of sample thickness, h at (A) $Z = Z_{CP}$ and (B) Z = 24 mm

6.2.3 Effect of working temperature

The temperature has strong effects on the levitation force and the hysteresis loops of the superconductors. The levitation force of $YBa_2Cu_3O_{7-\delta}$ (YBCO) and MgB_2 bulks increases firstly as the temperature decreases, then tends towards saturation as reported elsewhere [43]. It has also been mentioned that the hysteresis of the levitation force increases and increases and the critical current density, J_C, decreases as the temperature increases [43,153]. It is reasonable to suppose that the same phenomenon occurs in the case of the lateral force. At

LIMSA, measurements of the levitation and lateral forces between a 70 mm diameter MgB_2 disc and a 70 mm diameter magnet have been carried out at different temperatures and are reported in (Fig.6-8). The levitation force curves recorded at 20 K and 26 K are similar and without hysteresis. Hysteresis can be seen at 28 K while the levitation force decreases slightly. The levitation force drops strongly and shows a wide hysteresis loop when the temperature increases to 30 K.

The lateral forces measured at Z = 16 mm at different temperatures are shown in Fig.6-8(B). The slopes of the $F_Y(Y)$ curves show that the stability of the levitating system is improved as the working temperature increases. In addition, the $F_Y(Y)$ slope measured at T = 30 K is still negative at Z = 10 mm while the levitation force is equal to 166 N. This suggests that MgB_2 superconductor cooled down with liquid hydrogen could be good candidates for SML applications.

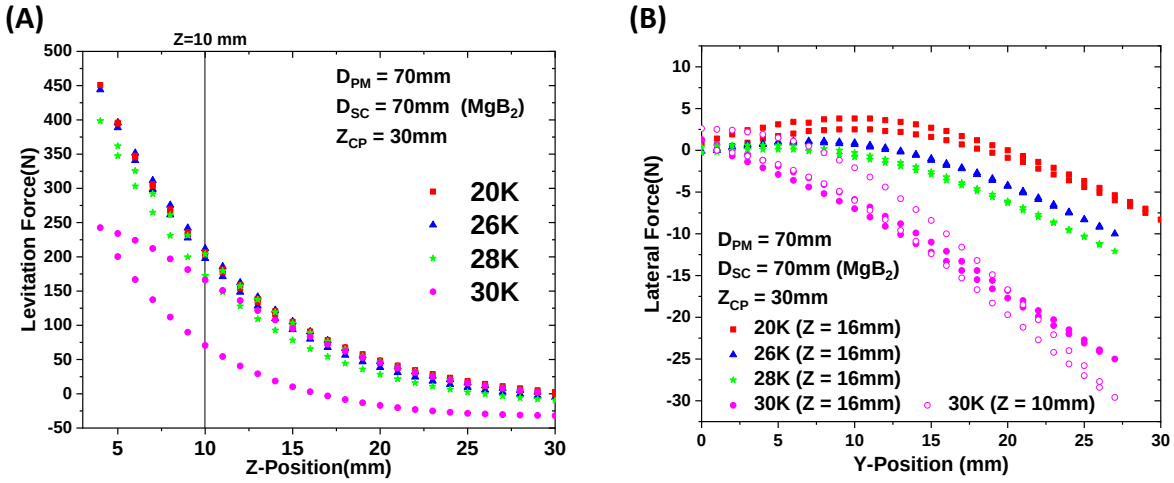

Fig.6-8: Comparison between 20-30 K of the (A) levitation forces and (B) lateral forces of 70 mm diameter and 10 mm thick MgB_2 disc after field cooling at 30 mm from the 70 mm diameter magnet.

The most used superconductor material in SML system till today is YBCO, which can be cooled down with liquid nitrogen [81,154,155]. In order to compare the behavior of MgB_2 discs to that of YBCO bulks, we have investigated the effect of temperature on the levitation and lateral forces of a 56 mm diameter and 16 mm thick YBCO cylindrical bulk provided by CAN superconductors (Czech Republic). As for the MgB_2 discs, the levitation force decreases as the temperature increases (Fig.6-9(A)). Although the stiffness should be determined by measurements on minor hysteresis loops since the $F_Y(Y)$ curves are strongly hysteretic, the results reported in Fig.6-9(B) sugggest that the stability of the system increases (Fig.6-9) with the temperature, as in the case of MgB_2 .

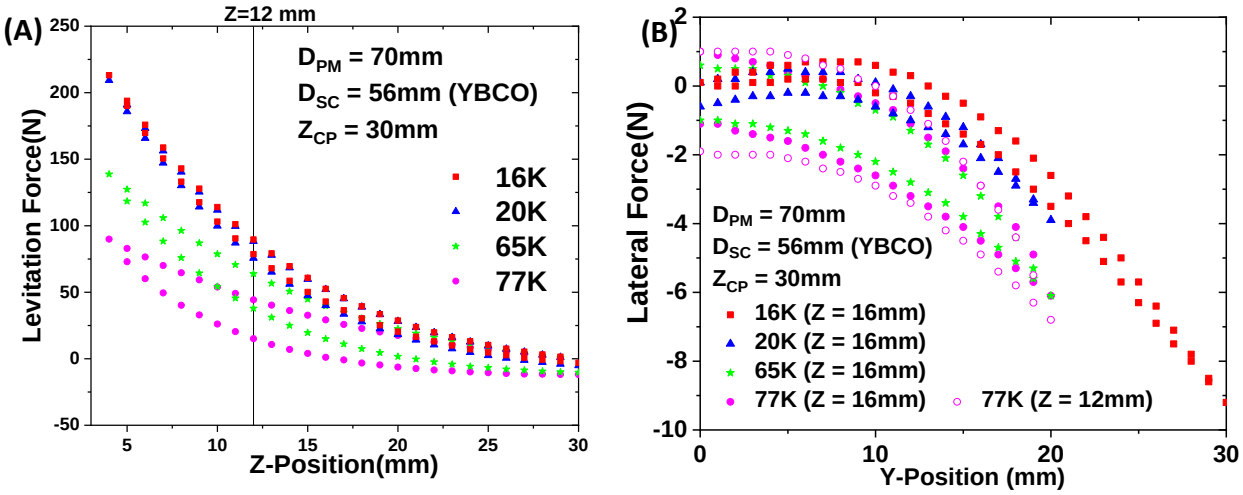

Fig.6-9: Comparison between 16 K and 77 K of the levitation forces (A) and of the lateral forces (B) of a 56 mm diameter and 16 mm thick YBaCuO disc after field cooling at 30 mm from the 70 mm diameter magnet.

These results demonstrates the negative effects of a low working temperature on the stability of a SML system and the possibility to use MgB_2 bulks in these systems.

6.2.4 Simulation work

During the field cooling process, as long as the sample is in the normal state, the applied magnetic field penetrates the whole bulk. At the transition to the superconducting state at T_c, the magnetic flux is channeled along vortex lines, while the field vanishes elsewhere in the superconductor. Below T_c, for constant applied field, the situation is frozen and no shielding current flows in the superconductor. Changes in Z cause changes in the applied field and induce a gradient in the density of the vortices, resulting in the generation of shielding currents and that of the levitation force. Different analytical and numerical approaches have been proposed for modeling magnetic levitation. As mentioned in chapter 2 and previous articles [43,141], we have proposed an analytical model to reproduce the measurements, assuming that the shielding currents flow in a layer of thickness t facing the magnet and generate magnetic moment m (J_C, t, ΔB). Fig.6-10 shows the vertical field component produced by the 70 mm diameter NdFeB magnet used during the measurements and its field gradient, which have be used to calculate ΔB (see section 2.3.3.1).

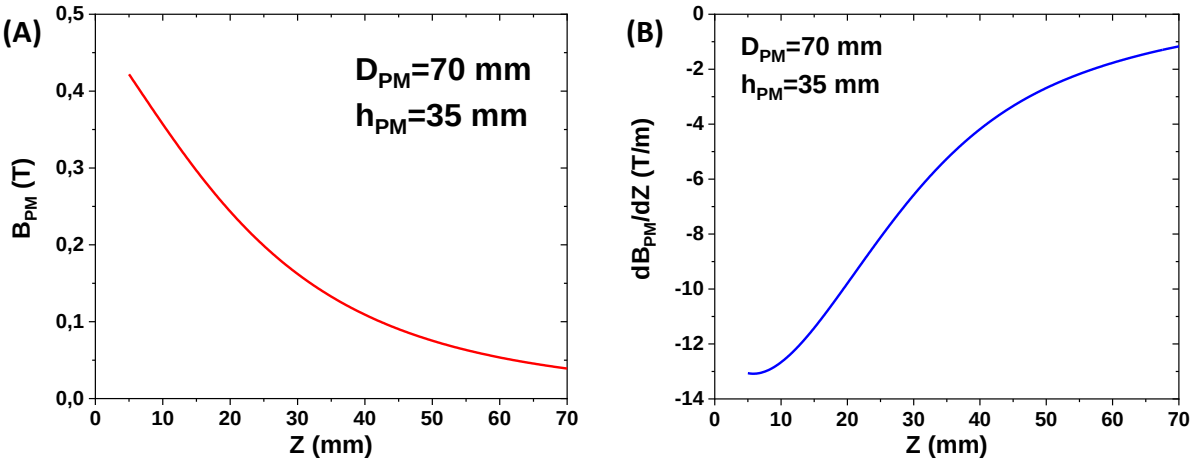

Fig.6-10: Field (A) and field gradient (B) along the axis of the NdFeB magnet used during the measurements.

The levitation forces measured at LIMSA along the axis of a 50 mm and a 70 mm diameter MgB_2 discs with a thickness of 10 mm are shown in Fig.6-11. The best reproductions of the results with the model detailed in section 2.3.3.1 are also reported. Clearly, the model does not account for the measurements, at least at low *Z*. While work is in progress to improve the model, a numerical model developped by Prof. Morandi's team [143,144] for the reproduction of the measurements has been tested. The numerical model is based on the subdivision of the superconductor in a finite number of current loops with a rectangular cross-section. It is assumed that the electric field *E* and the current density *J* are parallel at any point of the superconductor and oriented along the circumferential direction. In addition to the Maxwell's equations a power law between *E* and *J* is used to account for the superconductor behaviour:

$$E = E_C \left(\frac{J}{J_C}\right)^n \quad \text{[Eq.6.2]}$$

In [Eq.6.2] E_C is usually the electric field criterion employed for defining J_c, while *n* is proportional to the activation energy of vortex depinning. The interaction force between the permanent magnet and the superconductor is written as:

$$F = \int_v J \times B_{PM}\, dv \quad \text{[Eq.6.3]}$$

the integration is carried out on the volume *v* of the superconductor. Other detailed expressions are reported elsewhere [143]. The dashed lines in Fig.6-11 show the results calculated with the numerical model considering $J_c = 10^5$ A/cm^2. The measurements are well reproduced for Z > 10 mm, but overestimated for *Z* < 10 mm. As a consequence, simulation should be improved in future works.

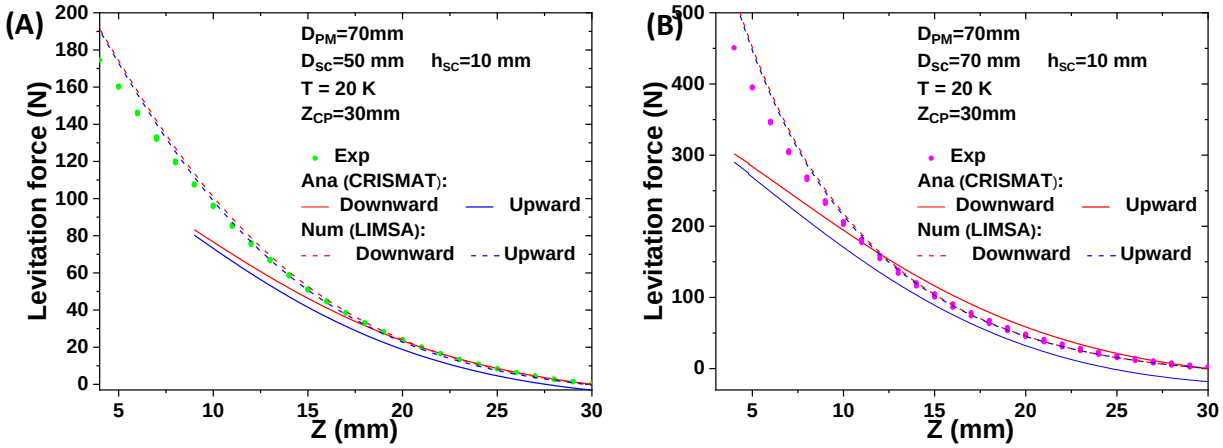

Fig.6-11: Force cycles of (A) the 50 mm and (B) the 70 mm diameter MgB_2 bulk measured at LIMSA. The continuous lines show the values calculated with the CRISMAT analytical model. The dashed lines show the values estimated with the numerical model used at LIMSA.

6.3 Trapped field measurements

Fig.6-12 shows the flux density above the surface of 20, 40 and 70 mm diameter discs at 20 K, after field cooling down the samples with a 70 mm diameter NdFeB permanent magnet located above the cryostat at 9 mm from the superconductor surface. The measurements were done by scanning a Hall sensor 10 mm above the bulks surface. The trapped field distribution shows a single dome. This conical distribution of the magnetic field shows that the transport of the current in the samples is homogeneous. The maximum trapped field increases with increasing superconductor diameter. However, the trapped fields are low because the field generated by the magnet 10 mm away from the magnet was equal to 0.35 T only. To fully investigate the trapped field capacities of MgB_2 we have magnetized our samples at higher applied fields.

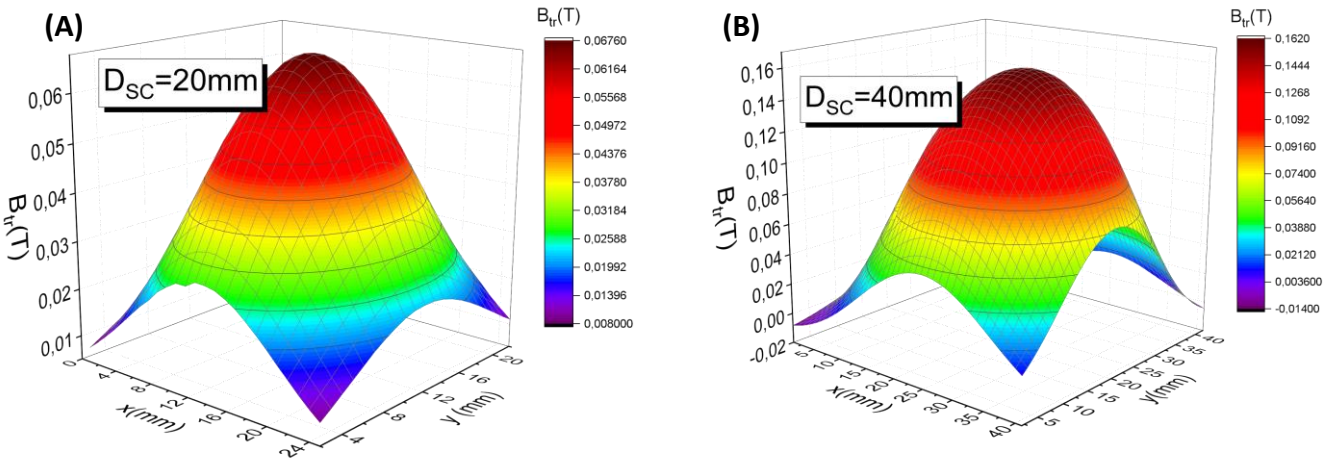

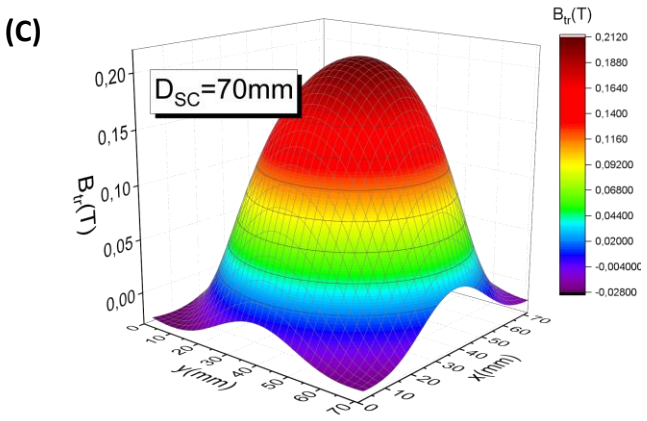

Fig.6-12: Magnetic mapping of (A) 20, (B) 40 and (C) 70mm diameter MgB_2 discs.

As mentioned in chapter 2, measurement of the trapped field at high field was carried out firstly on a 20 mm diameter and 10 mm thick ex-situ MgB_2 bulk in the PPMS (Quantum Design, 9T) equipment with a Hall sensor located at an altitude of 0.5 mm above the sample surface. After cooling the superconductor down to 20 K while applying a 3 T external magnetic field, the external field was decreased to zero at a rate equal to 0.06 T/min. Fig.6-13(A) shows the field measured above the center of the sample during this step. The field trapped at zero applied field is equal to 2.16 T, which is in the range of the fields reported for similar measurements on MgB_2 [40,100,156].

The trapped field, B_{tr}, decreases linearly with increasing temperature (Fig.6-13(B)) and drops to 0 T at 37.5 K, which corresponds to the critical temperature recorded in previous measurements. However, we have observed flux jumps during the measurements. This phenomenon manifests itself by a sudden decrease of the trapped field occurring at given applied fields. It has been more thoroughly investigated during measurements carried out at LNCMI, Grenoble.

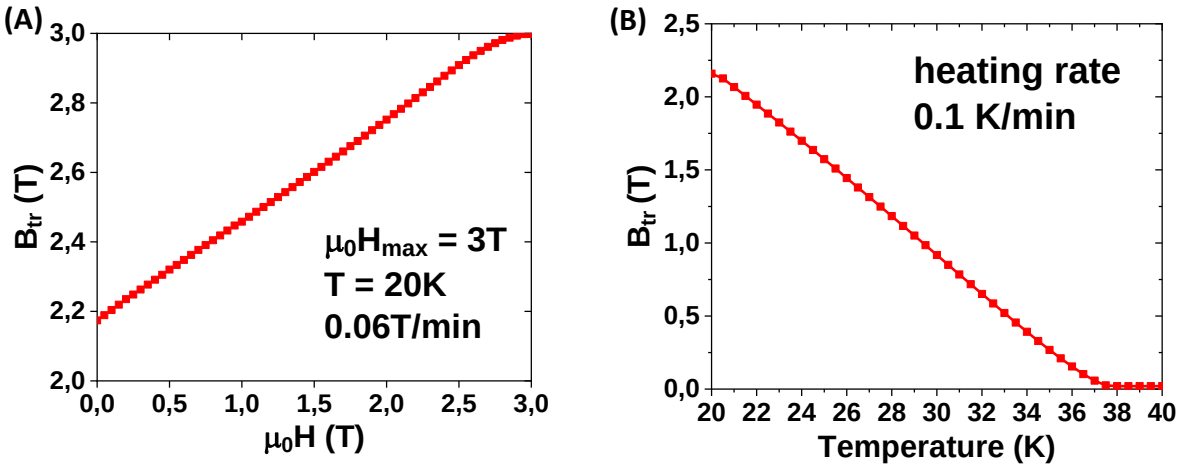

Fig.6-13: (A) Trapped field vs. applied magnetic field for the 20 mm diameter MgB_2 disc at 20 K. The applied field is 3 T, and the reduction rate is 0.06 T/min. (B) Trapped field vs. applied temperature with a 0.1 K/min heating rate.

The fields trapped by large diameter discs (D_{SC} > 30mm) were measured at Grenoble. The samples were cooled down to the working temperature (20 K) under a 4 T external field provided by an Oxford superconducting coil. After temperature stabilization, the applied magnetic field was decreased to zero at a rate equal to 0.05 T/min. As detailed in section 2.3.4.3 the field was measured by three Hall sensors labelled as H1, H2 and H3 located along a radius of the sample. The position of each sensor is indicated in Fig.2-11. Fig.6-14(A) shows the field trapped by a 80 mm diameter disc. Many flux jumps are visible. The field trapped at the center of the sample (measured by sensor H1) is slightly higher than that measured at other locations by H2 and H3. According to measurements of the temperature reported by the C1 and C2 cernox sensors, the thermal gradient along the disc radius is around 0.07 K/mm. Otherwise, the flux jumps are associated to temperature jumps. The intensity of the energy dissipation during the flux jumps is reflected by the temperature variations. The fields trapped in the same conditions by 10 mm thick MgB_2 disc with D_{SC} = 30 mm and D_{SC} = 40 mm are plotted along that of the 80 mm one in Fig.6-14(B). Compared to the 80 mm diameter disc, the reduction in the flux jump frequency and the lower temperature rise of these two samples during the flux jumps is an indication that small diameter superconductors show a stronger thermal stability than larger ones, which is in agreement with the model of Zhang et al. [157]. These authors have also mentioned that the ramp rate and the working temperature have effects on the flux jumps. As a consequence, in future work, we expect to improve our results by controlling the field rate. In addition we intend to study the effect of complex shapes, such as rings, reinforced samples and samples with multiple holes designs.

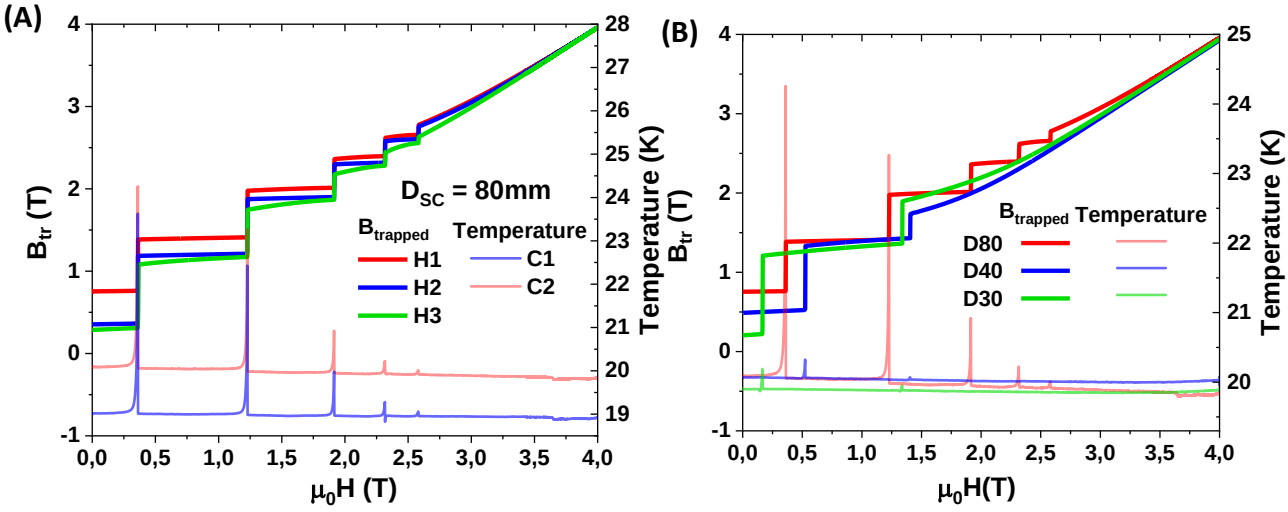

Fig.6-14: (A) Applied field dependence of trapped field and temperature for three positions of Hall probe and two positions of Cernox probe on the surface of the 80 mm diameter disc. (B) Applied field dependence of trapped field and temperature for three different diameter samples.

6.4 Conclusions

We have investigated the influence of the size of the MgB_2 bulks and of the working temperature on the superconducting magnetic levitation and guidance forces. The results have shown that the levitation force, F_Z increases with the sample diameter and that there is a linear relation between F_Z and R^3 which is attributed to the dependency of the magnetic moment on the radius of the samples (Eq.2.6). Otherwise, the levitation forces do not depend on the thickness h of the samples above some threshold and are slow varying functions of h below the threshold. This behavior can be linked to the limited thickness t of the layer carrying the superconducting currents. We have also investigated the effect of the working temperature. The results have shown that the stability can be improved by increasing the temperature, but that this causes a decrease of the levitation force as a consequence of the reduction of the critical current density J_c. The comparison of the data obtained at CRISMAT to those obtained at LIMSA is encouraging. They will be more deeply investigated in the future in order to improve the models we have used. Finally, we have investigated the field trapped by various samples with different equipments. The measurements have evidenced the generation of flux jumps and their links to sudden increases of the temperature. Nevertheless, we have been able to trap a 2.16 T field at 20 K with a 20 mm diameter and 10 mm thick MgB_2 bulk.

Chapter 7 Conclusions and perspectives

MgB_2 bulks exhibit various aspects interesting for applications, such as a medium-high critical temperature T_c (39 K), a reasonably high upper critical field H_{c2}, and a high critical current density J_c. However, due to the low packing ratio of the bulks fabricated by the conventional sintering methods, their domains of applications are limited. In this thesis, we have used the unconventional "Spark Plasma Sintering" (SPS) to prepare highly dense MgB_2 bulks. It is a rapid consolidation method that results in a better understanding and control of the sintering kinetics than the other techniques. It allows to prepare dense samples while controlling the grain growth and to save processing time.

The influence of the starting powder on the superconducting properties of MgB2 has been investigated in this work. Optimizing the SPS processing parameters as well as the sintering conditions, the critical current density of the samples could be increased. This has resulted from the control of the microstructure and from the increase of both the bulks density and the flux pinning capability. Sintering precusors containing nano-particles of boron in tungsten carbide (WC) molds, has resulted in samples with a packing density equal to 94%, large enough to ensure a large critical current density equal to $J_c = 7.10^5$ A/cm^2 at 20 K in self-field. In presence of a magnetic field, J_c has decreased but in the 20 K range, it has kept values large enough at 4 T for most applications (10^4 A/cm^2). This significant J_c improvement can be attributed to the strong densification of the nano grains and to the suppression of the MgB_4 phase during the sintering pressure at high pressure and low temperature. In addition, sintering the powder containing carbon-coated boron, J_c could be increased to 10^4 A/cm^2 at 5 T.

We have investigated the functional properties of bulks fabricated with the commercial MgB_2 powder, especially the levitation and stabilizing forces on the one hand and the trapped field on the other hand. The force measurements results have revealed that large diameter MgB_2 discs can be good candidates for superconducting magnetic levitation (SML) system using a cryogenic fluid such as hydrogen or neon. Concerning field trapping, the best field trapped with a 20 mm diameter and 10 mm thick sample at 20 K was around 2.16 T. However, it is difficult to trap high fields with large MgB_2 discs because of the occurrence of flux jumps.

In conclusion, the characteristics and performances reminded of above, the light weight, the mechanical properties and the simple fabrication process of MgB_2 bulks suggest that they could be one of the best candidates for applications using liquid hydrogen or liquid neon as cryo-coolant.

Finally, we point out below some typical phenomena observed during our experiments. Anisotropy after SPS sintering has been observed in both ex-situ and in-situ bulks. Here, we present as an example results obtained with ex-situ bulks. Fig.7-1 shows the XRDs recorded with X-rays i) parallel and ii) perpendicular to the SPS uniaxial pressure applied to a sample sintered at 1050°C and 100 MPa. There is clearly a preferred orientation of the crystallites parallel to the (00ℓ) planes.

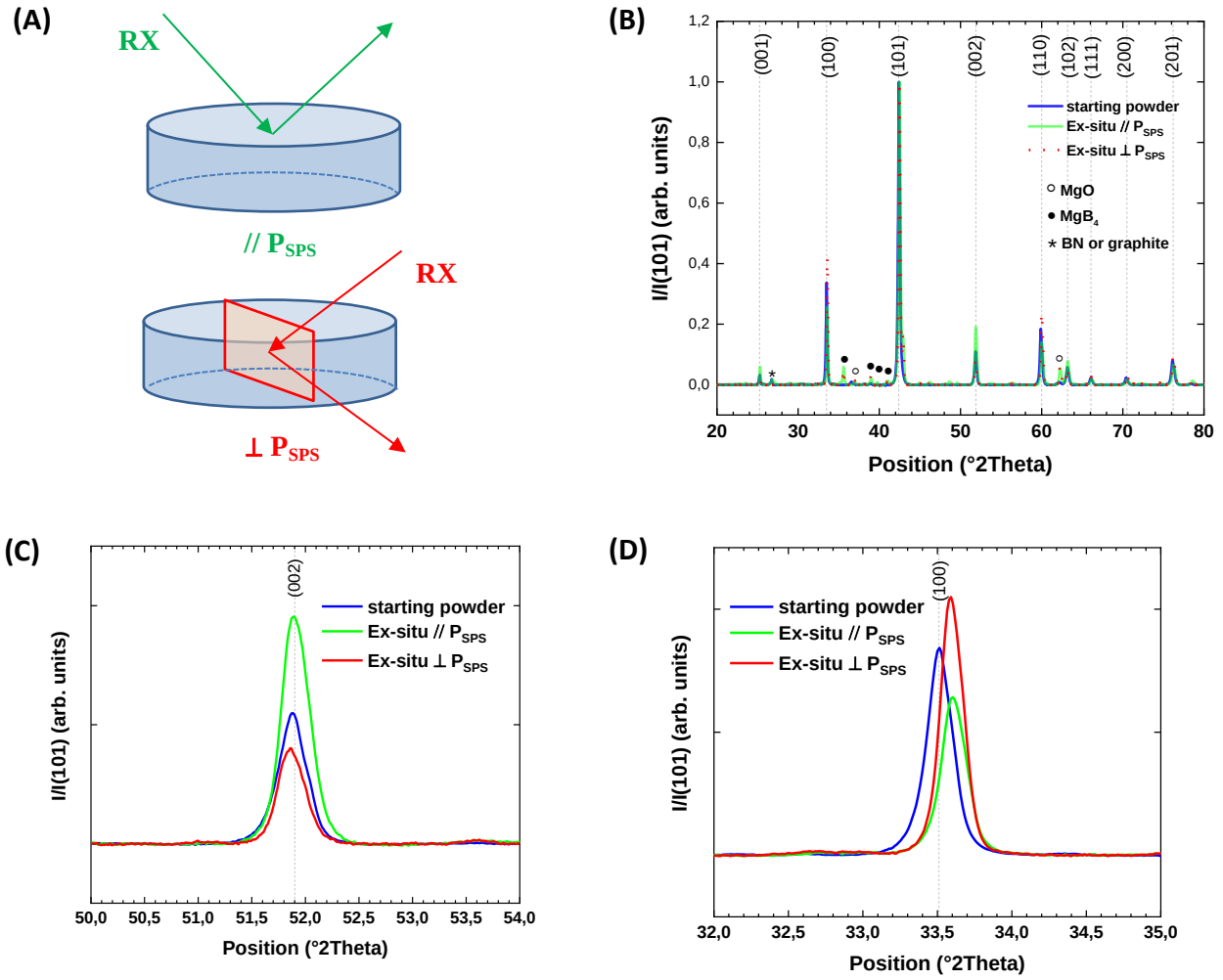

Fig.7-1: (A) The indication of the XRD measurements direction for the sintered MgB_2 disc. (B) XRD patterns of the initial powder and the sintered bulk obtained on different surfaces. The intensity is normalized by the peak (*101*), which is the most intense peak for a randomly oriented sample. (C) and (D) shows the magnified results of (*002*) and (*100*) peak, respectively.

Correlated anisotropies have been observed in the H_{irr}, H_{c2} and J_c measurements. As mentioned in chapter 2, the direction of the external magnetic field applied during our previous measurements was parallel to the SPS pressure ($\mu_0 H // P_{SPS}$). Fig 7-2 shows the H_{irr}, H_{c2} and J_c of an ex-situ sample measured while applying the magnetic field i) parallel and ii) perpendicular to the SPS pressure. When the external field is perpendicular to the SPS pressure ($\mu_0 H \perp P_{SPS}$), H_{irr}, H_{c2} and J_c are larger than when it is parallel ($\mu_0 H // P_{SPS}$), suggesting that pinning is more efficient in this field direction, as mentioned elsewhere [51].

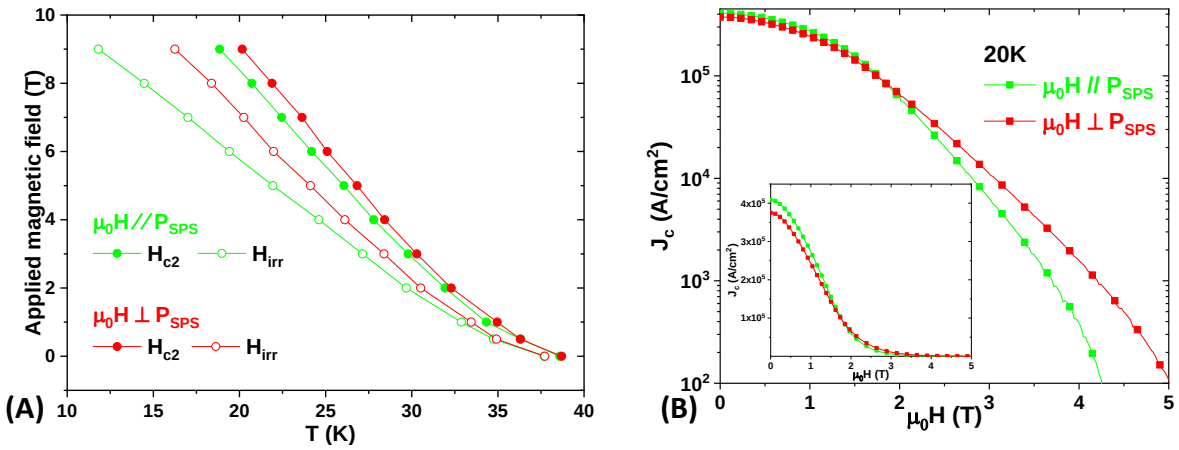

Fig.7-2: (A) Temperature dependence of H_{c2} and H_{irr} for different applied field directions. (B) Magnetic field dependence of the critical current density J_c at 20 K for different applied field directions. The inset shows the same curves on a linear scale.

Another noteworthy aspect is that the sample aspect ratio affects the magnetic moment measured with the SQUID magnetometer. The roughly cubic specimen (1.5 x 1.5 x 1.62 mm^3) cut from the W1 sample was firstly investigated as described in chapter 4. Then, the same specimen was cut again to obtain a thinner sample with dimensions v = 1.5 x 1.5 x 0.4 mm^3 and its magnetic moment was measured at 20 K. The *m(H)* hysteresis curves have shown strong differences: while that of the thin sample is almost symmetric, that of the thicker one is strongly assymetric (Fig.7-3(A)). Although they are in the same ranges, this discrepancy affects the critical current densities estimated with the extended Bean model [93], as seen in ((Fig.7-3(C)). Similar observations have been done by other authors, as shown in Fig.7-4. These discrepancies result probably from the demagnetizing field of the samples and consequently, a correction to the magnetic measurements needs to be developed in future works.

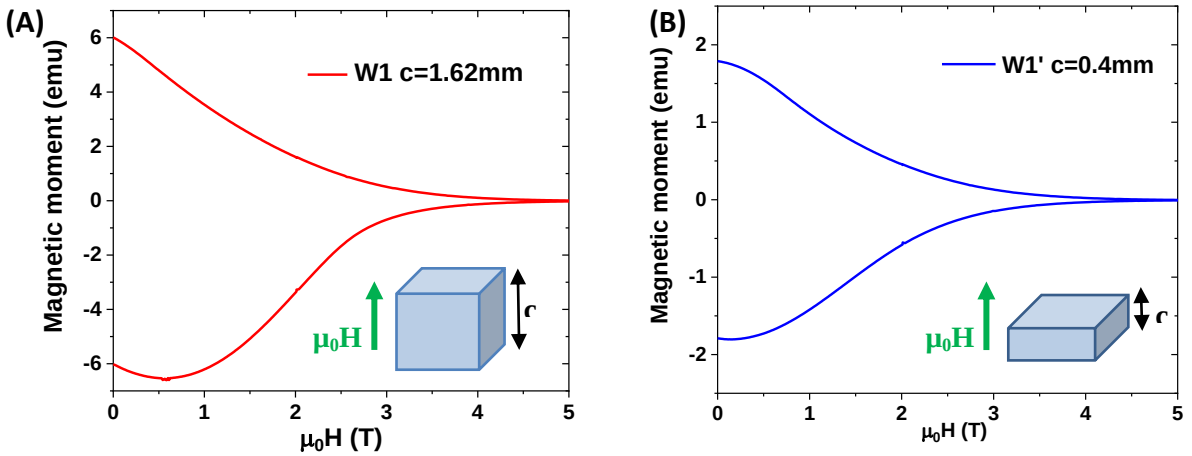

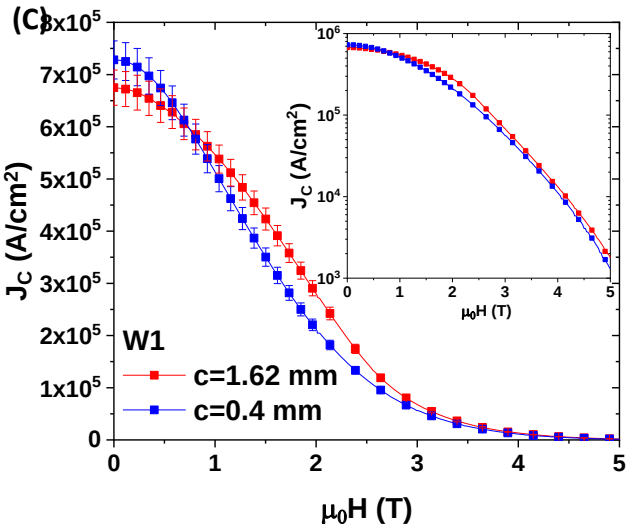

Fig.7-3: *M-H* loops at 20 K of W1 sample with dimensions of (A)1.5 x 1.5 x 1.62 mm^3 and (B) 1.5 x 1.5 x 0.4 mm^3. (C) Magnetic field dependence of the critical current density J_c estimated from these two size samples. The inset shows the same curves on a linear scale.

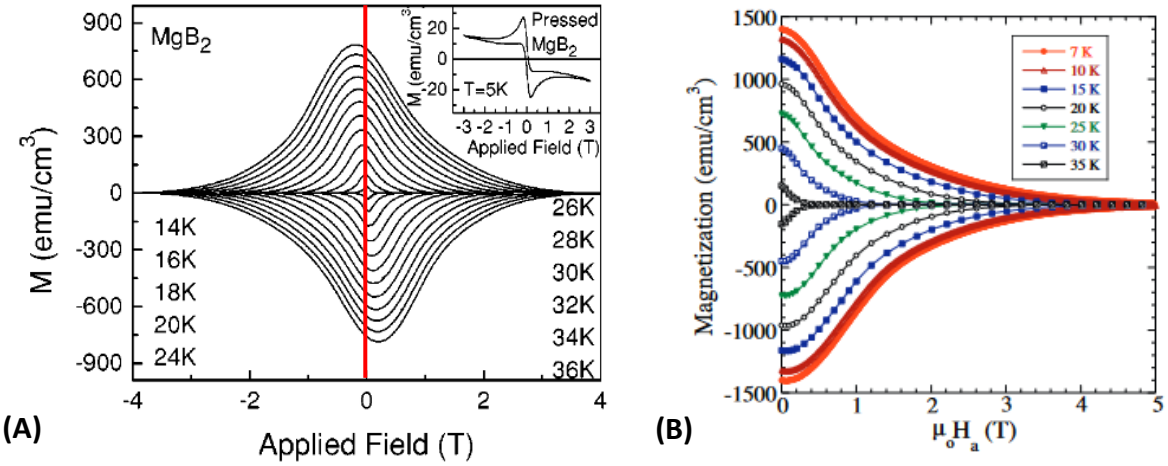

Fig.7-4: (A) *M-H* loops reported in [158] with a 2.18 x 2.76 x 1.88 mm^3 sample (B) *M-H* loops reported in [36] with a 1.5 x 1.5 x 0.5 mm^3 sample

Publications and communications

Articles

1. Y. Thimont, **Y. Xing**, P. Bernstein, M. Miryala and J. Noudem

"Joining superconducting MgB_2 parts by Spark Plasma Sintering: a new technique with high potential for manufacturing future superconducting devices"

*Coatings **12**, 1151(2022)*

2. P. Bernstein, **Y. Xing** and J. Noudem

"Calculation of the forces applied to a superconductor in levitation in an inhomogeneous magnetic field"

Journal Recent Progress in Materials (2022) (Under review)

3. J. G. Noudem, **Y. Xing**, M. Prakasam, F. Balima, A. Largeteau, and P. Bernstein

Superconducting properties of bulk MgB_2 processed by ultra-high pressure spark plasma sintering

(In process)

4. **Y. Xing**, P. Bernstein, M. Muralidhar and J. G. Noudem

"High critical current density of in-situ MgB_2 bulk superconductor fabricated by Spark Plasma Sintering"

*Nanomaterials **12**, 2583 (2022)*

5. **Y. Xing**, P. Bernstein and J. Noudem

"Superconductor-Magnetic Levitation: Investigation of the Restoring Force"

*IEEE Trans. Appl. Supercond. **31** 1–4 (2021)*

6. J. G. Noudem and **Y. Xing**

"Overview of Spark Plasma Texturing of Functional Ceramics"

Ceramics, vol. 4, n^o 1, p. 97-107 (mars 2021)

7. J. G. Noudem, **Y. Xing**, P. Bernstein, R. Retoux, M. Higuchi, S. S. Arvapalli, M. Muralidhar and M. Murakami

"Improvement of critical current density of MgB_2 bulk superconductor processed by Spark Plasma Sintering"

J. Am. Ceram. Soc. 103, 6169–6175 (2020).

Oral Communications

1. P. Bernstein, **Y. XING** and J. Noudem

"Characterization of a New Superconducting Magnetic Levitation System with a Large Levitation Force"

2022 Virtual MRS Spring Meeting, May 23-25,

2. J. Noudem, **Y. Xing**, P. Luigi Ribani, Giacomo Russo, A. Morandi and P. Bernstein

"The potential of MgB_2 superconductors for the magnetic levitation of Maglev vehicles"

2022 Virtual MRS Spring Meeting, May 8-13, Honolulu, Hawai'i

3. **Y. XING**, P. Bernstein, G. Chevallier, C. Estournès and J. Noudem

"Caractérisation des cryoaimants supraconducteurs MgB_2 denses fabriqués par Spark Plasma Sintering"

Journées annuelles 2022 du Groupe Français de Céramique (GFC), March 22-24, Albi, France.

4. **Y. Xing**, P. Bernstein, M.Muralidhar and J. Noudem

"Effect of Mg addition on the critical current density of dense MgB_2 bulk superconductors processed by spark plasma sintering"

The 34th International Symposium on Superconductivity, November 30 – December 2, 2021, Japon (Video conference)

5. **Y. Xing**, P. Bernstein, M.Muralidhar and J. Noudem

"High critical current density of MgB_2 bulk superconductor fabricated by Spark Plasma Sintering"

12th International Workshop on Processing and Applications of Superconducting Bulk Materials November 11 – 13, 2021, Shanghai, China (Video conference)

6. J. Noudem, **Y. Xing**, P. Luigi Ribani, Giacomo Russo, A. Morandi and P. Bernstein

Could MgB_2 superconductors be used in Maglev vehicles?

12th International Workshop on Processing and Applications of Superconducting Bulk Materials November 11 – 13, 2021, Shanghai, China (Video conference)

7. **Y. Xing**, J. Lecourt, C. Bilot, S.Gascoin, F. Veillon, P. Bernstein et J. Noudem

"Spark Plasma Sintering: densification des cryo-aimants superaconducteur MgB_2"

Journées scientifiques du GFDM-FACE, October 2021, Caen, France

8. J. Noudem, **Y. Xing** and P. Bernstein

"MgB_2—A Promising Material for Large Scale Applications of Superconductivity"

2021 Virtual MRS Spring Meeting, April 17 - 23, 2021

9. P. Bernstein, **Y. XING** and J. Noudem

"Analytical modelling of the functional properties of superconductors: a useful tool complementary to numerical simulation"

2021 Virtual MRS Spring Meeting, April 17 - 23, 2021

10. **Y. Xing,** J. Lecourt, C. Bilot, S. Gascoin, P. Bernstein and J. Noudem

"Spark Plasma Sintering de cryoaimants supraconducteurs MgB_2"

Journées annuelles 2021 du Groupe Français de Céramique (GFC), March 23-25, Caen (Video conference), France.

11. **Y. XING**, P. Bernstein, G. Chevallier, C. Estournès and J. Noudem

"Spark Plasma Sintering de cryoaimants supraconducteurs MgB_2"

Journée thématique « Pièces de grandes dimensions par SPS », January 25th, 2021 GFDM FACE (Video conference)

12. **Yiteng XING** Jacques NOUDEM and Pierre BERNSTEIN*

"Superconductor-Magnetic Levitation: investigation of the restoring force"

2020 Applied Superconductivity Conference (Video conference), October 24 – November 7, 2020

13. **Yiteng XING**, Pierre BERNSTEIN and Jacques NOUDEM

"Superconducting Magnetic Levitation of MgB_2 bulks: the Effect of the sample thickness"

The 33rd International Symposium on Superconductivity (ISS2020), December 1-3, AIST Tsukuba (Video conference), Japan

14. Pierre Bernstein, **Yiteng Xing** and Jacques Noudem

Magnetic Levitation Force and Stability in Axisymmetric Systems Magnetic.

The 33rd International Symposium on Superconductivity (ISS2020), December 1-3, AIST Tsukuba (Video conference), Japan

Poster Communications

1. "Applications of MgB_2 superconducting cryomagnets",

Yiteng XING, Pierre Bernstein, Kévin Berger and Jacques Noudem

Workshop-Safran Tech : journée scientifique, applications de la supraconductivité, Paris-Saclay, January 30th 2020.

2. "Restoring force and stability in superconductor-magnetic levitation"

Yiteng XING, Pierre Bernstein, and Jacques Noudem

Workshop international HTS 2022: Numerical Modelling of High Temperature Superconductors, Nancy, France, June 14 to 16, 2022

References

[1] Lord K 1848 On an absolute thermometric scale *Phil. Mag*

[2] von Wroblewski Sigm and Olszewski K 1883 On the liquefaction of oxygen and the congelation of carbon disulphide and alcohol *The London, Edinburgh, and Dublin Philosophical Magazine and Journal of Science* **16** 75–6

[3] von Wroblewski S and Olszewski K 1883 On the liquefaction of nitrogen and carbonic oxide *The London, Edinburgh, and Dublin Philosophical Magazine and Journal of Science* **16** 76–76

[4] Dewar J 1898 Liquid hydrogen *Nature* **58** 270–270

[5] Onnes H K 1908 The condensation of helium *Nature* **77** 581–581

[6] Onnes H K 1911 On the sudden change in the rate at which the resistance of mercury disappears *Commun. Phys. Lab. Univ. Leiden, c* **124**

[7] Geballe T, Geller S and Corenzwit E 1954 Superconductivity of Nb_3Sn *Phys. Rev.* **95** 1435

[8] Berlincourt T G 1962 *Pulsed-magnetic-field studies of superconducting transition metal alloys at high and low current densities* (Atomics International. Div. of North American Aviation, Inc., Canoga Park …)

[9] Josephson B D 1962 Possible new effects in superconductive tunnelling *Physics letters* **1** 251–3

[10] Bednorz J G and Müller K A 1986 Possible high T c superconductivity in the Ba−La−Cu−O system *Zeitschrift für Physik B Condensed Matter* **64** 189–93

[11] Wu M K, Ashburn J R, Torng C J, Hor P H, Meng R L, Gao L, Huang Z J, Wang Y Q and Chu C W 1987 Superconductivity at 93 K in a new mixed-phase Y-Ba-Cu-O compound system at ambient pressure *Phys. Rev. Lett.* **58** 908–10

[12] Oto K, Murase K and Takaoka S 1989 Resistivity, Hall coefficient and transition temperatures in doped 80K and 110K Bi-Sr-Ca-Cu-O superconductors *Solid state communications* **71** 819–22

[13] Liu J, Vandervoort K, Claus H, Crabtree G and Lam D 1988 Low field magnetic properties of superconducting $Tl_2Ba_2Ca_2Cu_3O_x$ single crystals *Physica C: Superconductivity* **156** 256–8

[14] Schilling A, Cantoni M, Guo J and Ott H 1993 Superconductivity above 130 K in the Hg–Ba–Ca–Cu–O system *Nature* **363** 56–8

[15] Gao L, Xue Y Y, Chen F, Xiong Q, Meng R L, Ramirez D, Chu C W, Eggert J H and Mao H K 1994 Superconductivity up to 164 K in $HgBa_2Ca_{m-1}Cu_mO_{2\,m+2+\delta}$ (m =1, 2, and 3) under quasihydrostatic pressures *Phys. Rev. B* **50** 4260–3

[16] J. Nagamatsu, N. Nakagawa, T. Muranaka, Y. Zenitani, J. Akimitsu 2001 Superconductivity at 39 K in magnesium diboride *Nature* **410** 63–4

[17] Kamihara Y, Hiramatsu H, Hirano M, Kawamura R, Yanagi H, Kamiya T and Hosono H 2006 Iron-Based Layered Superconductor: LaOFeP *J. Am. Chem. Soc.* **128** 10012–3

[18] Kamihara Y, Watanabe T, Hirano M and Hosono H 2008 Iron-Based Layered Superconductor La[$O_{1-x}F_x$]FeAs (x= 0.05−0.12) with T_c= 26 K *J. Am. Chem. Soc.* **130** 3296–7

[19] Liu R H, Wu G, Wu T, Fang D F, Chen H, Li S Y, Liu K, Xie Y L, Wang X F, Yang R L, Ding L, He C, Feng D L and Chen X H 2008 Anomalous Transport Properties and Phase Diagram of the FeAs-Based $SmFeAsO_{1-x}F_x$ Superconductors *Phys. Rev. Lett.* **101** 087001

[20] Ge J-F, Liu Z-L, Liu C, Gao C-L, Qian D, Xue Q-K, Liu Y and Jia J-F 2015 Superconductivity above 100 K in single-layer FeSe films on doped $SrTiO_3$ *Nature Mater* **14** 285–9

[21] Bardeen J, Cooper L N and Schrieffer J R 1957 Theory of Superconductivity *Phys. Rev.* **108** 1175–204

[22] Drozdov A P, Eremets M I, Troyan I A, Ksenofontov V and Shylin S I Conventional superconductivity at 203 K at high pressures 19

[23] Hemley R J, Ahart M, Liu H and Somayazulu M Road to Room-Temperature Superconductivity: Tc above 260 K in Lanthanum Superhydride under Pressure 11

[24] Snider E, Dasenbrock-Gammon N, McBride R, Debessai M, Vindana H, Vencatasamy K, Lawler K V, Salamat A and Dias R P 2020 Room-temperature superconductivity in a carbonaceous sulfur hydride *Nature* **586** 373–7

[25] Grockowiak A D, Ahart M, Helm T, Coniglio W A, Kumar R, Somayazulu M, Meng Y, Oliff M, Williams V, Ashcroft N W, Hemley R J and Tozer S W 2020 Hot Hydride Superconductivity above 550 K *arXiv:2006.03004 [cond-mat]*

[26] Meissner W and Ochsenfeld R 1933 Ein neuer effekt bei eintritt der supraleitfähigkeit *Naturwissenschaften* **21** 787–8

[27] Ginzburg V and Landau L 1950 Theory of superconductivity *Zh. Eksp. Teor. Fiz.;(USSR)* **20**

[28] Arovas D and Wu C 2019 Lecture Notes on Superconductivity (A Work in Progress)

[29] Abrikosov A A 1957 The magnetic properties of superconducting alloys *Journal of Physics and Chemistry of Solids* **2** 199–208

[30] Essmann U and Träuble H 1967 The direct observation of individual flux lines in type II superconductors *Physics letters A* **24** 526–7

[31] Kramer E J 1973 Scaling laws for flux pinning in hard superconductors *J. Appl. Phys.* **44** 12

[32] Dew-Hughes D 1974 Flux pinning mechanisms in type II superconductors *Philosophical Magazine* **30** 293–305

[33] Jones M E and Marsh R E 1954 The Preparation and Structure of Magnesium Boride, MgB_2 *J. Am. Chem. Soc.* **76** 1434–6

[34] Huang X, Mickelson W, Regan B C and Zettl A 2005 Enhancement of the upper critical field of MgB_2 by carbon-doping *Solid State Communications* **136** 278–82

[35] Prikhna T, Eisterer M, Gawalek W, Kozyrev A, Weber H W, Sokolovsky V, Chaud X, Noudem J, Habisreuther T, Moshchil V, Karpets M, Basyuk T, Kovylaev V, Dellith J, Sverdun V, Kuznietsov R,

Shmidt C, Vitovetskaya T and Polikarpova L 2013 Synthesis Pressure–Temperature Effect on Pinning in MgB_2-Based Superconductors *J Supercond Nov Magn* **26** 1569–76

[36] Muralidhar M, Inoue K, Koblischka M R, Murakami A and Murakami M 2015 Effects of Silver Addition on Critical Current Densities and Mechanical Properties in Bulk MgB_2 *Advanced Engineering Materials* **17** 831–8

[37] Muralidhar M, Kenta N, Koblischka M R and Murakami M 2015 High critical current densities in bulk MgB_2 fabricated using amorphous boron: High critical current densities in bulk MgB_2 *Phys. Status Solidi A* **212** 2141–5

[38] Yamamoto A, Ishihara A, Tomita M and Kishio K 2014 Permanent magnet with MgB_2 bulk superconductor *Appl. Phys. Lett.* **105** 032601

[39] Durrell J H, Dancer C E J, Dennis A, Shi Y, Xu Z, Campbell A M, Babu N H, Todd R I, Grovenor C R M and Cardwell D A 2012 A trapped field of >3 T in bulk MgB_2 fabricated by uniaxial hot pressing *Supercond. Sci. Technol.* **25** 112002

[40] Fuchs G, Häßler W, Nenkov K, Scheiter J, Perner O, Handstein A, Kanai T, Schultz L and Holzapfel B 2013 High trapped fields in bulk MgB_2 prepared by hot-pressing of ball-milled precursor powder *Supercond. Sci. Technol.* **26** 122002

[41] Noudem J G, Aburras M, Bernstein P, Chaud X, Muralidhar M and Murakami M 2014 Development in processing of MgB_2 cryo-magnet superconductors *Journal of Applied Physics* **116** 163916

[42] Noudem J G, Bernstein P, Dupont L, Martin F G R, Sotelo G G, Dias D H N, de Andrade R, Muralidhar M and Murakami M 2020 Spark plasma sintering of bulk MgB_2 and levitation force measurements *Supercond. Sci. Technol.* **33** 024001

[43] Bernstein P, Colson L, Dupont L and Noudem J 2017 Investigation of the levitation force of field-cooled YBCO and MgB_2 disks as functions of temperature *Superconductor Science and Technology* **30** 065007

[44] Kang W N, Kim H-J, Choi E-M, Jung C U and Lee S-I 2001 MgB_2 Superconducting Thin Films with a Transition Temperature of 39 Kelvin *Science* **292** 1521–3

[45] Shi Z X, Zhang Y X, Lv H, Xu M, Choi E-M and Lee S-I 2007 Flux pinning in c-axis-oriented MgB_2 thin film *Physica C: Superconductivity and its Applications* **467** 101–5

[46] Canfield P C, Finnemore D K, Bud'ko S L, Ostenson J E, Lapertot G, Cunningham C E and Petrovic C 2001 Superconductivity in Dense MgB_2 Wires *Phys. Rev. Lett.* **86** 2423–6

[47] Liu Y, Cheng F, Qiu W, Ma Z, Al Hossain M S and Dou S X 2016 High performance MgB_2 superconducting wires fabricated by improved internal Mg diffusion process at a low temperature *J. Mater. Chem. C* **4** 9469–75

[48] Grasso G, Malagoli A, Ferdeghini C, Roncallo S, Braccini V, Siri A S and Cimberle M R 2001 Large transport critical currents in unsintered MgB_2 superconducting tapes *Appl. Phys. Lett.* **79** 230–2

[49] Fang H, Padmanabhan S, Zhou Y X and Salama K 2003 High critical current density in iron-clad MgB_2 tapes *Appl. Phys. Lett.* **82** 4113–5

[50] Dulčić A, Požek M, Paar D, Choi E-M, Kim H-J, Kang W N and Lee S-I 2003 Coherence lengths and anisotropy in MgB_2 superconductor *Phys. Rev. B* **67** 020507

[51] Lyard L, Samuely P, Szabo P, Klein T, Marcenat C, Paulius L, Kim K H P, Jung C U, Lee H-S, Kang B, Choi S, Lee S-I, Marcus J, Blanchard S, Jansen A G M, Welp U, Karapetrov G and Kwok W K 2002 Anisotropy of the Upper Critical Field and Critical Current in Single Crystal MgB_2 *Phys. Rev. B* **66** 180502

[52] Kumakura H, Takano Y, Fujii H, Togano K, Kito H and Ihara H 2001 Critical current densities and irreversibility fields of MgB_2 bulks *Physica C* 5

[53] Jung S-G, Seong W K and Kang W N 2012 Effect of columnar grain boundaries on flux pinning in MgB_2 films *Journal of Applied Physics* **111** 053906

[54] Noudem J, Dupont L, Bernstein P, Retoux R, Chevallier G, Estournès C, Berger K, Higuchi M, Muralidhar M and Murakami M 2019 Superconducting cryo-magnets processed by spark plasma sintering and texturing *Spark Plasma Sintering* pp 185–99

[55] Noudem J G, Xing Y, Bernstein P, Retoux R, Higuchi M, Arvapalli S S, Muralidhar M and Murakami M 2020 Improvement of critical current density of MgB_2 bulk superconductor processed by Spark Plasma Sintering *Journal of the American Ceramic Society* **103** 6169–75

[56] Zhao Y, Feng Y, Cheng C H, Zhou L, Wu Y, Machi T, Fudamoto Y, Koshizuka N and Murakami M 2001 High critical current density of MgB_2 bulk superconductor doped with Ti and sintered at ambient pressure *Appl. Phys. Lett.* **79** 1154–6

[57] Liu Y, Lan F, Ma Z, Chen N, Li H, Barua S, Patel D, Shahriar M, Hossain A, Acar S, Kim J H and Dou S X 2015 Significantly enhanced critical current density in nano-MgB_2 grains rapidly formed at low temperature with homogeneous carbon doping *Supercond. Sci. Technol.* **28** 055005

[58] Peng J, Liu Y, Ma Z, Shahriar Al Hossain M, Xin Y and Jin J 2016 Superior critical current density obtained in MgB_2 bulks via employing carbon-coated boron and minor Cu addition *Physica C: Superconductivity and its Applications* **528** 60–4

[59] Wang Q 2012 *Fabrication et propriétés physiques de conducteurs multifilamentaires MgB_2 dopés au carbone* Thesis

[60] e Naturali F *Supersonic O2 Beam Assisted Deposition of Long-Length YBa2Cu3O7 Coated Conductors*

[61] Mustapić M, Horvat J, Hossain M S, Skoko Ž and Dou S 2013 Enhancing superconducting properties of MgB_2 pellets by addition of amorphous magnetic Ni–Co–B nanoparticles *Superconductor Science and Technology* **26** 075013

[62] Arvapalli S S *Innovative Techniques for Enhancement of Superconducting Characteristics of Bulk MgB_2* (SHIBAURA INSTITUTE OF TECHNOLOGY)

[63] Kim S, Stone D S, Cho J-I, Jeong C-Y, Kang C-S and Bae J-C 2009 Phase stability determination of the Mg–B binary system using the CALPHAD method and ab initio calculations *Journal of Alloys and Compounds* **470** 85–9

[64] Giunchi G 2003 High density MgB_2 obtained by reactive liquid Mg infiltration *Int. J. Mod. Phys. B* **17** 453–60

[65] Bhagurkar A G, Yamamoto A, Babu N H, Durrell J H, Dennis A R and Cardwell D A 2015 Synthesis of dense bulk MgB_2 by an infiltration and growth process *Supercond. Sci. Technol.* **28** 015012

[66] Prikhna T, Eisterer M, Gawalek W, Mamalis A G, Kozyrev A, Kovylaev V, Hristoforou E, Weber H W, Noudem J G, Goldacker W, Moshchil V, Chaud X, Sokolovsky V, Shaternik A, Dellith J, Schmidt C, Habisreuther T, Litzkendorf D, Dub S, Borimskiy A, Sergienko N, Sverdun V and Prisyazhnaya E 2014 Structure and Functional Properties of Bulk MgB_2 Superconductors Synthesized and Sintered under Pressure *MSF* **792** 21–6

[67] Suarez M, Fernandez A, Menendez J L, Torrecillas R, U. H, Hennicke J, Kirchner R and Kessel T 2013 Challenges and Opportunities for Spark Plasma Sintering: A Key Technology for a New Generation of Materials *Sintering Applications* ed B Ertug (InTech)

[68] M. Tokita, Mater. 1999 Development of large-size ceramic/metal bulk FGM fabricated by spark plasma sintering *Sci Forum* **308** 83

[69] Orrù R, Licheri R, Locci A M, Cincotti A and Cao G 2009 Consolidation/synthesis of materials by electric current activated/assisted sintering *Materials Science and Engineering: R: Reports* **63** 127–287

[70] Dadiel J L, Naik S P K, Pęczkowski P, Sugiyama J, Ogino H, Sakai N, Kazuya Y, Warski T, Wojcik A, Oka T and Murakami M 2021 Synthesis of Dense MgB_2 Superconductor via In Situ and Ex Situ Spark Plasma Sintering Method *Materials* **14** 7395

[71] Liu C F, Yan G, Du S J, Xi W, Feng Y, Zhang P X, Wu X Z and Zhou L 2003 Effect of heat-treatment temperatures on density and porosity in MgB_2 superconductor *Physica C: Superconductivity* **386** 603–6

[72] Horvat J, Soltanian S, Wang X L and Dou S X 2004 Effect of sample size on magnetic Jc for MgB_2 superconductor *Appl. Phys. Lett.* **84** 3109–11

[73] Horvat J, Soltanian S, Pan A V and Wang X L 2004 Superconducting screening on different length scales in high-quality bulk MgB_2 superconductor *Journal of Applied Physics* **96** 4342–51

[74] Muralidhar M, Nozaki K, Kobayashi H, Zeng X L, Koblischka-Veneva A, Koblischka M R, Inoue K and Murakami M 2015 Optimization of sintering conditions in bulk MgB_2 material for improvement of critical current density *Journal of Alloys and Compounds* **649** 833–42

[75] Zou J, Ainslie M D, Fujishiro H, Bhagurkar A G, Naito T, Babu N H, Fagnard J-F, Vanderbemden P and Yamamoto A 2015 Numerical modelling and comparison of MgB_2 bulks fabricated by HIP and infiltration growth *Supercond. Sci. Technol.* **28** 075009

[76] Prikhna T A 2009 Properties of MgB_2 bulk

[77] Tixador P 2006 Concepts for HTS and MgB_2 in transformers vol 47 (Trans Tech Publ) pp 195–203

[78] Ballarino A, Bordini B and Giannelli S 2016 MgB_2 Transmission Lines for the Large Hadron Collider *MgB2 Superconducting Wires: Basics and Applications* (World Scientific) pp 581–91

[79] Razeti M, Angius S, Bertora L, Damiani D, Marabotto R, Modica M, Nardelli D, Perrella M and Tassisto M 2008 Construction and Operation of Cryogen Free MgB_2 Magnets for Open MRI Systems *IEEE Trans. Appl. Supercond.* **18** 882–6

[80] Nakamura T, Yamada Y, Nishio H, Kajikawa K, Sugano M, Amemiya N, Wakuda T, Takahashi M and Okada M 2012 Development and fundamental study on a superconducting induction/synchronous motor incorporated with MgB_2 cage windings *Supercond. Sci. Technol.* **25** 014004

[81] Deng Z, Zhang W, Zheng J, Ren Y, Jiang D, Zheng X, Zhang J, Gao P, Lin Q, Song B and Deng C 2016 A High-Temperature Superconducting Maglev Ring Test Line Developed in Chengdu, China *IEEE Transactions on Applied Superconductivity* **26** 1–8

[82] Lilit M 2021 China debuts train prototype that can hit speeds of 620 kilometers per hour

[83] Bernstein P and Noudem J 2020 Superconducting magnetic levitation: principle, materials, physics and models *Supercond. Sci. Technol.* **33** 033001

[84] Hühne R High temperature superconductors: Properties and applications

[85] Inoue K Spark discharge machining energy source

[86] Noudem J G, Kenfaui D, Chateigner D and Gomina M 2012 Toward the enhancement of thermoelectric properties of lamellar $Ca_3Co_4O_9$ by edge-free spark plasma texturing *Scripta Materialia* **66** 258–60

[87] Guillon O, Gonzalez-Julian J, Dargatz B, Kessel T, Schierning G, Räthel J and Herrmann M 2014 Field-Assisted Sintering Technology/Spark Plasma Sintering: Mechanisms, Materials, and Technology Developments *Advanced Engineering Materials* **16** 830–49

[88] Kim J H, Dou S X, Shi D Q, Rindfleisch M and Tomsic M 2007 Study of MgO formation and structural defects in *in situ* processed MgB_2 /Fe wires *Supercond. Sci. Technol.* **20** 1026–31

[89] Jain A, Ong S P, Hautier G, Chen W, Richards W D, Dacek S, Cholia S, Gunter D, Skinner D, Ceder G and Persson K A 2013 Commentary: The Materials Project: A materials genome approach to accelerating materials innovation *APL Materials* **1** 011002

[90] Rowell J M 2003 The widely variable resistivity of MgB_2 samples *Supercond. Sci. Technol.* **16** R17–27

[91] Bragg W H and Bragg W L 1913 The reflection of X-rays by crystals *Proceedings of the Royal Society of London. Series A, Containing Papers of a Mathematical and Physical Character* **88** 428–38

[92] Clarke J and Braginski A I 2006 *The SQUID handbook: Applications of SQUIDs and SQUID systems* (John Wiley & Sons)

[93] Ji H, Jin X and Fan H 1992 Bean model and critical current density of superconductor samples with different shapes *Chinese journal of low temperature physics* **14**

[94] Xu X, Kim J H, Hossain M S A, Park J S, Zhao Y, Dou S X, Yeoh W K, Rindfleisch M and Tomsic M 2008 Phase transformation and superconducting properties of MgB_2 using ball-milled low purity boron *Journal of Applied Physics* **103** 023912

[95] Bernstein P, Noudem J and Dupont L 2016 Critical current density and current distribution in field cooled superconducting disks *Supercond. Sci. Technol.* **29** 075007

[96] Brandt E H 1998 Superconductor disks and cylinders in an axial magnetic field. I. Flux penetration and magnetization curves *Phys. Rev. B* **58** 6506–22

[97] Xing Y, Bernstein P and Noudem J 2021 Superconductor-Magnetic Levitation: Investigation of the Restoring Force *IEEE Trans. Appl. Supercond.* **31** 1–4

[98] Hirano T, Takahashi Y, Namba S, Naito T and Fujishiro H 2020 A record-high trapped field of 1.61 T in MgB_2 bulk comprised of copper plates and soft iron yoke cylinder using pulsed-field magnetization *Supercond. Sci. Technol.* **33** 085002

[99] Namburi D K, Takahashi K, Hirano T, Kamada T, Fujishiro H, Shi Y-H, Cardwell D A, Durrell J H and Ainslie M D 2020 Pulsed-field magnetisation of Y-Ba-Cu-O bulk superconductors fabricated by the infiltration growth technique *Supercond. Sci. Technol.* **33** 115012

[100] Aldica G, Burdusel M and Badica P 2014 Trapped magnetic field in a (NdFeB)–(MgB_2) pair-type bulk magnet *Physica C: Superconductivity and its Applications* **505** 18–23

[101] Naito T, Takahashi Y and Awaji S 2020 A record-high trapped field of 5.6 T in the stacking of MgB_2 /TiB_2 composite bulks prepared by an *in-situ* hot isostatic pressing method *Supercond. Sci. Technol.* **33** 125004

[102] Lutterotti L, Matthies S and Wenk H 1999 MAUD: a user friendly Java program for Rietveld texture analysis and more *Newsletter of the CPD* pp 14–5

[103] Buzea C and Yamashita T 2001 Review of the superconducting properties of MgB_2 *Supercond. Sci. Technol.* **14** R115–46

[104] Uvarov V and Popov I 2013 Metrological characterization of X-ray diffraction methods at different acquisition geometries for determination of crystallite size in nano-scale materials *Materials Characterization* **85** 111–23

[105] Rathinasabapathy S, Santhosh M S and Asokan M 2020 Significance of Boron Nitride in Composites and Its Applications *Recent Advances in Boron-Containing Materials* ed M Aydin (IntechOpen)

[106] Chen S K, Yates K A, Blamire M G and MacManus-Driscoll J L 2005 Strong influence of boron precursor powder on the critical current density of MgB_2 *Supercond. Sci. Technol.* **18** 1473–7

[107] Kim, S.H., Kang, W.N., Lee, Y.J., Jun, B.H. and Kim, C.J. 2017 Effects of heat treatment temperature on the formation of MgB_2 bulk superconductors prepared using MgB_4 and Mg powder *Progress in Superconductivity and Cryogenics* **19** 42–6

[108] Yamamoto A, Shimoyama J, Kishio K and Matsushita T 2007 Limiting factors of normal-state conductivity in superconducting MgB_2 : an application of mean-field theory for a site percolation problem *Supercond. Sci. Technol.* **20** 658–66

[109] Senatore C, Lezza P, Lortz R, Shcherbakova O, Yeoh W K, Dou S X and Flukiger R 2007 Specific Heat and Magnetic Relaxation Analysis of MgB_2 Bulk Samples With and Without Additives *IEEE Trans. Appl. Supercond.* **17** 2941–4

[110] Barua S, Hossain M S A, Ma Z, Patel D, Mustapic M, Somer M, Acar S, Kokal I, Morawski A, Cetner T, Gajda D and Dou S X 2015 Superior critical current density obtained in MgB_2 bulks through low-cost carbon-encapsulated boron powder *Scripta Materialia* **104** 37–40

[111] Muralidhar M, Higuchi M, Jirsa M, Diko P, Kokal I and Murakami M 2017 Improved Critical Current Densities of Bulk MgB_2 Using Carbon-Coated Amorphous Boron *IEEE Trans. Appl. Supercond.* **27** 1–4

[112] Ma Z Q and Liu Y C 2011 Low-temperature synthesis of MgB_2 superconductors *International Materials Reviews* **56** 267–86

[113] Liu Z-K, Zhong Y, Schlom D G, Xi X X and Li Q 2001 Computational thermodynamic modeling of the Mg-B system *Calphad* **25** 299–303

[114] Karpinski J, Zhigadlo N D, Katrych S, Puzniak R, Rogacki K and Gonnelli R 2007 Single crystals of MgB_2: Synthesis, substitutions and properties *Physica C: Superconductivity* **456** 3–13

[115] Gonnelli R S, Daghero D, Ummarino G A, Calzolari A, Dellarocca V, Stepanov V A, Kazakov S M, Jun J and Karpinski J 2004 A Point-Contact Study of the Superconducting Gaps in Al-Substituted and C-Substituted MgB_2 Single Crystals *arXiv:cond-mat/0407267*

[116] Arvapalli S S, Miryala M, Jirsa M and Murakami M 2020 Size reduction of boron particles by high-power ultrasound for optimization of bulk MgB_2 *Supercond. Sci. Technol.* **33** 115009

[117] Zhang J Y, Zhang Y F, Lou Z W, Zhang P H, Li C Y, Yuan J W, Peng L, Ma Y X, Noudem J G and Izumi M 2021 The discrepancies in different facets of MgB_2 bulk superconductors prepared under various sintering durations by spark plasma sintering *Supercond. Sci. Technol.* **34** 045011

[118] Grigoroscuta M A, Aldica G, Pasuk I, Burdusel M, Sandu V, Kuncser A, Suzuki T S, Vasylkiv O and Badica P 2021 Partially-oriented MgB_2 superconducting bulks with addition of B_4C and cubic BN obtained by slip casting under high magnetic field and spark plasma sintering *Materials Research Bulletin* **134** 111103

[119] Naito T, Endo Y and Fujishiro H 2017 Optimization of vortex pinning at grain boundaries on *ex-situ* MgB_2 bulks synthesized by spark plasma sintering *Supercond. Sci. Technol.* **30** 095007

[120] Sandu V, Ionescu A M, Aldica G, Grigoroscuta M A, Burdusel M and Badica P 2021 On the pinning force in high density MgB_2 samples *Sci Rep* **11** 5951

[121] Eisterer M 2008 Calculation of the volume pinning force in MgB_2 superconductors *Phys. Rev. B* **77** 144524

[122] Grigoroscuta M A, Sandu V, Kuncser A, Pasuk I, Aldica G, Suzuki T S, Vasylkiv O and Badica P 2019 Superconducting MgB_2 textured bulk obtained by *ex situ* spark plasma sintering from green compacts processed by slip casting under a 12 T magnetic field *Supercond. Sci. Technol.* **32** 125001

[123] Matsumoto Y, Shigeta I, Abiru T, Terasaki Y, Akune T and Sakamoto N 2003 Critical current density and flux pinning characteristics of powdered MgB_2 specimens *Physica C: Superconductivity* **388–389** 163–4

[124] Shigeta I, Abiru T, Abe K, Nishida A and Matsumoto Y 2003 Temperature and field dependence of magnetization of MgB_2 polycrystals *Physica C: Superconductivity* **392–396** 359–63

[125] Ghorbani S R, Darini M, Wang X L, Hossain M S A and Dou S X 2013 Vortex flux pinning mechanism and enhancement of in-field J in succinic acid doped MgB_2 *Solid State Communications* **168** 1–5

[126] Noudem J G, Xing Y, Bernstein P, Retoux R, Higuchi M, Arvapalli S S, Muralidhar M and Murakami M 2020 Improvement of critical current density of MgB_2 bulk superconductor processed by Spark Plasma Sintering *Journal of the American Ceramic Society* **103** 6169–75

[127] Avdeev M, Jorgensen J D, Ribeiro R A, Bud'ko S L and Canfield P C 2003 Crystal chemistry of carbon-substituted MgB_2 *Physica C: Superconductivity* **387** 301–6

[128] Kang, Won Nam 2014 Single-Crystal like MgB_2 thin films grown on c-cut sapphire substrates *Progress in Superconductivity and Cryogenics* **16** 7–9

[129] Matsushita T 2014 MgB_2 *Flux Pinning in Superconductors* Springer Series in Solid-State Sciences ed T Matsushita pp 377–403

[130] Zeng R, Lu L, Wang J L, Horvat J, Li W X, Shi D Q, Dou S X, Tomsic M and Rindfleisch M 2007 Significant improvement in the critical current density of *in situ* MgB_2 by excess Mg addition *Supercond. Sci. Technol.* **20** L43–7

[131] Güner S B, Savaşkan B, Öztürk K, Çelik Ş, Aksoy C, Karaboğa F, Koparan E T and Yanmaz E 2019 Investigation on superconducting and magnetic levitation force behaviour of excess Mg doped-bulk MgB_2 superconductors *Cryogenics* **101** 131–6

[132] Hinks D G, Jorgensen J D, Zheng H and Short S 2002 Synthesis and stoichiometry of MgB_2 *Physica C: Superconductivity* **382** 166–76

[133] Perner O, Eckert J, Häßler W, Fischer C, Acker J, Gemming T, Fuchs G, Holzapfel B and Schultz L 2005 Stoichiometry dependence of superconductivity and microstructure in mechanically alloyed MgB_2 *Journal of Applied Physics* **97** 056105

[134] Jung C U, Kim H-J, Park M-S, Kim M-S, Kim J Y, Du Z, Lee S-I, Kim K H, Betts J B, Jaime M, Lacerda A H and Boebinger G S 2002 Effects of unreacted Mg impurities on the transport properties of MgB_2 *Physica C: Superconductivity* **377** 21–5

[135] Chauhan S R and Chaudhary S 2010 On the Residual Resistivity Ratio in MgB_2 Superconductors *IEEE Trans. Appl. Supercond.* **20** 26–32

[136] Ma Z, Liu Y, Zhao Q, Dong Z and Yu L 2009 Mechanism analysis for the enhanced electromagnetic properties in nano-SiC-doped MgB_2 based on the discussion of the sintering process *Supercond. Sci. Technol.* **22** 085015

[137] Vajpayee A, Jha R, Srivastava A K, Kishan H, Tropeano M, Ferdeghini C and Awana V P S 2011 The effect of synthesis temperature on the superconducting properties of n-SiC added bulk MgB_2 superconductor *Supercond. Sci. Technol.* **24** 045013

[138] Gozzelino L, Minetti B, Gerbaldo R, Ghigo G, Laviano F, Lopardo G, Giunchi G, Perini E, Cavallin T and Mezzetti E 2007 Pinning properties in pure and SiC doped MgB_2 bulk obtained by reactive Mg liquid infiltration technique *Physica C: Superconductivity and its Applications* **460–462** 604–5

[139] Susner M A, Sumption M D, Bhatia M, Peng X, Tomsic M J, Rindfleisch M A and Collings E W 2007 Influence of Mg/B ratio and SiC doping on microstructure and high field transport Jc in MgB_2 strands *Physica C: Superconductivity* **456** 180–7

[140] Qu B, Sun X D, Li J-G, Xiu Z M and Xue C P 2009 Phase evolution and microstructure of high J_c SiC doped MgB_2 fabricated by hot pressing *Supercond. Sci. Technol.* **22** 075014

[141] Bernstein P 2018 A new approach to the current distribution in field cooled superconductors disks *Supercond. Sci. Technol.* 8

[142] Xing Y, Bernstein P and Noudem J 2021 Superconductor-Magnetic Levitation: Investigation of the Restoring Force *IEEE Transactions on Applied Superconductivity* **31** 1–4

[143] Morandi A, Fabbri M, Ribani P L, Dennis A, Durrell J, Shi Y and Cardwell D 2018 The Measurement and Modeling of the Levitation Force Between Single-Grain YBCO Bulk Superconductors and Permanent Magnets *IEEE Trans. Appl. Supercond.* **28** 1–10

[144] Perini E, Giunchi G, Geri M and Morandi A 2009 Experimental and Numerical Investigation of the Levitation Force Between Bulk Permanent Magnet and MgB_2 Disk *IEEE Trans. Appl. Supercond.* **19** 2124–8

[145] Yang Y and Li C 2017 Numerical investigation of the relationship between magnetic stiffness and minor loop size in the HTS levitation system *AIP Advances* **7** 105327

[146] Yang Y and Li C 2017 Minor loop dependence of the magnetic forces and stiffness in a PM-HTS levitation system *AIP Advances* **7** 125028

[147] Hull J R and Cansiz A 1999 Vertical and lateral forces between a permanent magnet and a high-temperature superconductor *Journal of Applied Physics* **86** 6396–404

[148] Li H, Deng Z, Jin L, Li J, Li Y and Zheng J 2018 Lateral motion stability of high-temperature superconducting maglev systems derived from a nonlinear guidance force hysteretic model *Supercond. Sci. Technol.* **31** 075010

[149] Wang X, Ren Z, Song H, Wang X, Zheng J, Wang S, Wang J and Zhao Y 2005 Guidance force in an infinitely long superconductor and permanent magnetic guideway system *Supercond. Sci. Technol.* **18** S99–104

[150] Yildizer I, Cansiz A and Ozturk K 2016 Optimization of levitation and guidance forces in a superconducting Maglev system *Cryogenics* **78** 57–65

[151] Del Valle N, Sanchez A, Pardo E, Chen D-X and Navau C 2007 Optimizing levitation force and stability in superconducting levitation with translational symmetry *Appl. Phys. Lett.* **90** 042503

[152] Navau C, Sanchez A and Pardo E 2003 Lateral force in permanent magnet-superconductor levitation systems with high critical current *IEEE Trans. Appl. Supercond.* **13** 2185–8

[153] Zhou J, Zhang X-Y and Zhou Y-H 2010 Temperature dependence of levitation force and its relaxation in a HTS levitation system *Physica C: Superconductivity* **470** 336–9

[154] Dias D H N, Sotelo G G, Sass F, Motta E S, Jr R de A and Stephan R M 2012 Dynamical Tests in a Linear Superconducting Magnetic Bearing *Physics Procedia* **36** 1049–54

[155] Mattos L S, Rodriguez E, Costa F, Sotelo G G, de Andrade R and Stephan R M 2016 MagLev-Cobra Operational Tests *IEEE Trans. Appl. Supercond.* **26** 1–4

[156] Sasaki T, Naito T and Fujishiro H 2013 Trapped Magnetic Field of Dense MgB_2 Bulks Fabricated under High Pressure *Physics Procedia* **45** 93–6

[157] Zhang W, Xia J, Yong H and Zhou Y 2020 Mechanical response induced by flux jump in a cylindrical superconductor *AIP Advances* **10** 025021

[158] Qin M J, Wang X L, Liu H K and Dou S X 2002 Evidence for vortex pinning induced by fluctuations in the transition temperature of MgB_2 superconductors *Phys. Rev. B* **65** 132508